Proceedings of the Tenth Asian Congress of Fluid Mechanics
17-21 May 2004, Peradeniya, Sri Lanka

INTERACTION OF THE SEA BREEZE WITH INLAND URBAN HEAT ISLANDS OF DIFFERENT INTENSITY

A. Cenedese and P. Monti
Dipartimento di Idraulica Trasporti e Strade, Università "La Sapienza, Via Eudossiana 18, Rome, Italy

ABSTRACT: Using laboratory experimental data taken from a temperature controlled water tank, some aspects of the circulation associated with an inland urban heat island (UHI) and its interaction with a sea-breeze current were investigated. The similarity between nocturnal and diurnal UHIs and the role played by the UHI intensity on the resulting circulation in presence of sea breeze have been investigated. Comparisons with field observations, numerical experiments and other laboratory simulations are also presented and discussed.

1. INTRODUCTION

UHIs are defined as the warmth produced by cities [1]. Generally, they form above cities during both daytime and nighttime, with peculiar characteristics with respect to atmospheric boundary layers existing in rural areas. Because many large cities are located in the vicinity of shorelines, it is of great interest to investigate the circulation associated with the interaction between a UHI and a sea breeze. The objective of this work is to investigate in the laboratory the flow field induced by the simultaneous presence of an inland three-dimensional daytime UHI and a sea breeze current, in the absence of prevailing winds.

2. EXPERIMENTAL SETUP AND FLOW PARAMETERS

Experiments were carried out in a water-filled rectangular tank (Fig.1) with a length L=1800 mm, a height H of 95 mm and a width of 600 mm (along the x, z and y axis, respectively) open at the top and with a horizontal aluminum bottom. The lateral sides of the tank were made up of 10 mm thick transparent glass. The bottom was divided into two sections. The temperature T_S of the left section ("sea side") was kept constant by means of a heat exchanger connected to a heater bath circulator, while a heater-cooler bath circulator set the temperature T_L of the right section ("land side"). The separation line between the two sections is the "coastline". To produce the ambient thermal stratification, dT_a/dz (T_a is the ambient temperature), the temperature T_U of the upper surface was set to a constant value by means of a third heat exchanger. The surplus of surface heat flux H_0 between the city and its rural environment was simulated by means of a thin (~0.2 mm), circular shaped, electric heater (diameter D=100 mm), whose center was placed above the land side at x_{UHI}=450 mm from the coastline. H_0 was controlled by means of a suitable power supply. Information about flow kinematics has been extracted by using Particle Tracking Velocimetry. The studied area was rectangular (x=200 mm, z=48 mm) lying in the vertical plane x-z orthogonal to the coastline passing through the center of the electric heater. A thin laser light sheet from a 3 W Argon Laser beam passing through an optical device illuminated the measurement plane. The water was seeded with pine pollen particles. We define the origin (x=0, z=0) at the center of the heater, x positive downwind from the heater and negative upwind. Along the longitudinal direction the domain lay in the range $-1<x/D<1$, the heater in $-0.5<x/D<0.5$ while the coastline was at x/D=-4.5. A set of images was taken during each experiment by means of a CCD video camera at 25 Hz for a sampling interval t_{samp}=1800 s. One out every four frames was automatically retrieved, lowering the resulting sampling rate to 6.25 Hz. From the trajectories evaluated at each instant from the centroid positions, the instantaneous Lagrangian velocity field was obtained. A Gaussian interpolation algorithm was applied to the velocity samples in order to obtain a 2D Eulerian description of the motion on a 40 20 regular grid along the x- and z-axis, respectively. Temperatures were taken using ten T-type (copper-constantan) thermocouples placed on a vertical rake, equally spaced every 4 mm in the vertical from 0 to 36 mm, at a sampling rate of 1 Hz for the same time interval t_{samp} used for the velocity measurements.

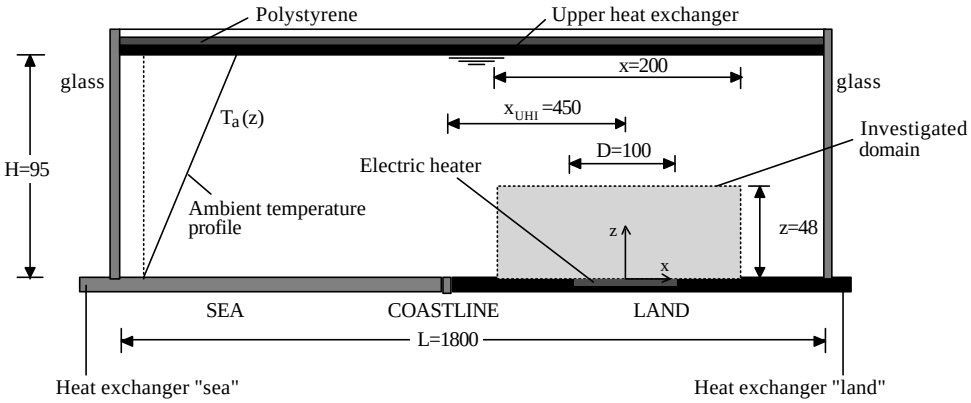

Fig. 1: Schematic of the water tank (all measurements in millimeters, y-axis normal to the x-z plane).

Table 1: Parameters for the experiments

Case	H_0 (Wm^{-2})	H_L (Wm^{-2})	U (ms^{-1})	z_i(m)	T_m (°C)	Fr	Re	Breeze
Case 1.A	300		0.0027	0.009	2.0	0.038	270	No
Case 1.B	300	300	0.0034	0.013	1.9	0.049	340	No
Case 1.C	300	300	0.0034	0.013	1.1	0.049	340	Yes
Case 2.A	500		0.0032	0.012	2.7	0.045	320	No
Case 2.B	500	300	0.0037	0.018	2.2	0.052	370	No
Case 2.C	500	300	0.0037	0.018	1.4	0.052	370	Yes
Case 3.A	750		0.0036	0.015	3.5	0.051	360	No
Case 3.B	750	300	0.0041	0.021	3.0	0.058	410	No
Case 3.C	750	300	0.0041	0.021	2.1	0.058	410	Yes
Case 4.A	1250		0.0043	0.020	5.5	0.061	430	No
Case 4.B	1250	300	0.0046	0.024	4.0	0.067	460	No
Case 4.C	1250	300	0.0046	0.024	3.0	0.067	460	Yes
Case 5.A	2000		0.0050	0.024	6.5	0.073	500	No
Case 5.B	2000	300	0.0053	0.028	6.7	0.076	530	No
Case 5.C	2000	300	0.0053	0.028	5.9	0.076	530	Yes

It has been showed [2] that in calm and stably stratified environments, UHIs can be modeled by combining D, dT_a/dz and H_0. They also showed, by means of a bulk convection model, that for fully turbulent flows the Froude number Fr=U/ND was the only non-dimensional parameter governing the dynamics of low-aspect-ratio thermal plumes. Here, $U=(g\ DH_0/\ _0c_p)^{1/3}$ was the horizontal velocity scale (W=UFr the vertical velocity scale), $N=(g\ dT_a/dz\ )^{1/2}$ the Brunt-Väisälä frequency, g the gravity, the thermal expansion coefficient, $_0$ the ambient density and c_p the specific heat. In particular, by keeping the Reynolds number Re=UD/ above a certain critical value, the simulated large-scale structures and the mean flow can both be considered independent of Re (Reynolds number independence [3]).

3. RESULTS AND DISCUSSION

Three types of experiments were performed, namely, the UHI developing in a calm, stably, stratified environment (nocturnal UHI, hereafter situation A), the UHI developing in a statically unstable environment (diurnal UHI, situation B) and the interaction between a daytime UHI and a sea breeze flow (situation C). Five values of H_0 were prescribed for each one of the above situations. Thus, a total of 15 cases (Cases i.A, i.B and i.C, where i ranged from 1 to 5) were examined as listed in Table 1.

3.1 The nighttime and daytime UHIs

The temperature of the two bottom sections was set at the same value $T_L=T_S=27°C$, while the temperature of the upper surface was kept at $T_U=46$ °C. The resulting (constant with height) ambient

temperature gradient was dT_a/dz =200 °C m^{-1} (N~0.7 s^{-1}). Qualitative observations made during the UHI circulation growth after the heater was turned on were in agreement with those of [2]. At first the UHI rapidly grew and showed the formation of the classical axisymmetrical convective cell, with the thermal plume axis at the center of the heater (x/D=0), the converging flow above the bottom and the diverging flow at upper levels. Fig. 2a shows the mean temperature profiles taken at various radial distances from the UHI center for Case 4.A. The averaging time interval was set to t_{aver}=300 s (see [4]). The figure illustrates that inside the middle portion of the UHI (x/D=0 and 0.25) the temperature did not vary appreciably with height. Conversely, outside the heater (x/D=0.75) the boundary layer remained stably stratified and was signified by a temperature profile similar to that imposed for the ambient temperature T_a. Given the temperature profiles, it appeared that the resulting UHI circulation was dome-shaped, characterized by well-mixed conditions within its central region and maximum depth at x/D=0. In particular, Fig. 2a shows that at x/D=0 the temperature was nearly constant in the vertical range $0<z<z_i$=20 mm, where z_i is the mixing height. Defining z_e as the distance from the bottom to where the temperature of the plume axis and T_a coincided (equilibrium height), one could observe that for z_e=16 mm$<z<z_i$ the fluid inside the plume was cooler than that outside at the same height (crossover effect). Fig. 2b shows the vertical profiles for the temperature difference ($T-T_a$), scaled with the UHI intensity T_m for Case 4.A, measured at various radial distances from the heater center. The height z was scaled with z_i. Here, T_m is defined as the difference measured at z=0 between the temperature at the UHI center and T_a.

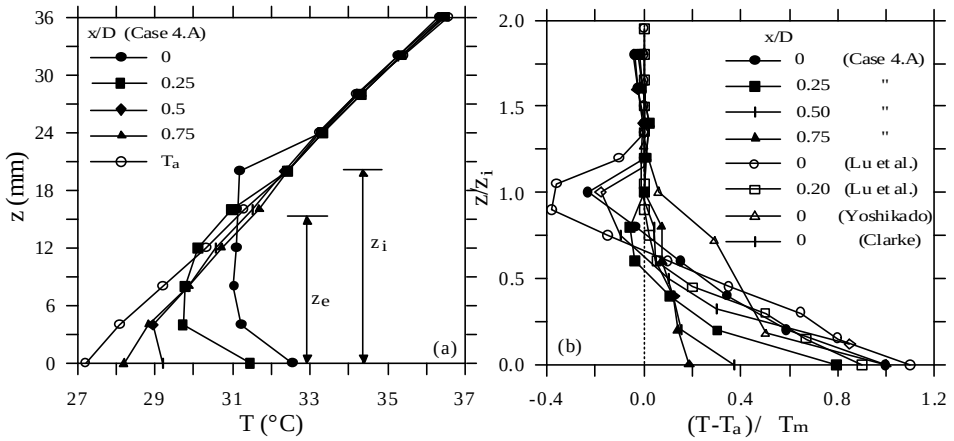

Fig. 2: (a) Mean temperature profiles as a function of the radial distance from the UHI center for Case 4.A. (b) As in (a) but for the nondimensional mean temperatures.

Fig. 2b also shows laboratory results carried out by [2] for Re=2920 and Fr=0.089, data from field experiments in Cincinnati [5] (Re=1.2×10^9 and Fr=0.013) and numerical results given by [6]. For the latter case, since the author did not report the value of the surface heat flux, Fr and Re could not be directly evaluated. Given D=25 km and d_a/dz=0.007 km^{-1}, respectively, the city radius and the ambient potential temperature gradient selected by [6] and by assuming H_0=40 Wm^{-2}, we have U 3 ms^{-1}, Fr=0.009 and Re=4.8×10^9. Despite the large differences in Re and Fr, there is reasonable agreement among the curves. This fact confirmed a previous finding of [2], that is, the shape of the non-dimensional mean temperature profiles of low-aspect-ratio UHIs depends on the location rather than the Reynolds and the Froude numbers. Fig. 3 depicts the averaged velocity field associated with the UHI circulation for Case 4.A. The shape of the flow pattern is consistent with the mean temperature profiles previously discussed.

To check the similarity among the velocity fields obtained for different values of the surface heat flux H_0, in Fig. 4a the vertical profiles of the mean vertical velocity w, normalized by the vertical velocity scale W, taken at the plume axis (x/D=0) for Cases i.A (where i=1 5) are shown (Cases i.B displayed in the figure will be discussed in the following). The figure also reports the profiles carried out by [6] and the laboratory results obtained by [7]. Fr and Re of [7] experiments were (Fr=0.047 — Re=3820) and

(Fr=0.077 — Re=8280). A noteworthy observation is that, with the exclusion of Case 1.A, the normalized vertical velocity profiles were quite similar, even though the profile obtained by [6] was distinctly different. Similar conclusions could be drawn for the normalized horizontal velocity u/U (not shown). The above discrepancies could be attributed both to the arbitrary choice for H_0 used to determine U and Fr for the numerical runs conducted by [6] and to the fact that his model was 2D. It should be also noted that a slight dependence on the experimental conditions was present. In essence, Re seemed to be the distinguishing feature, in that, as Re increased, so did the measured u/U and w/W. A possible reason for this was that the Reynolds number attained in the experiments was not large enough to match the full Reynolds number independence of the flow. Therefore, data points for Case 1.A, characterized by the smaller Re, need to be viewed with caution. Fig. 4b shows the vertical profiles of the normalized standard deviation of the horizontal velocities, $_u$/U, calculated at the UHI center for some of the nocturnal cases studied. The figures also report the water tank results of [7] and nighttime urban observations conducted at the city center of Sapporo, Japan, during light wind conditions [8] (Run 15 and 17). The agreement with the field data was reasonably good, even though the laboratory data of $_u$/U showed lower values with respect to those in the field measurements. This fact was probably related to the well known limitation of water tank simulations, caused by the finite size of vessels utilized in laboratories [7].

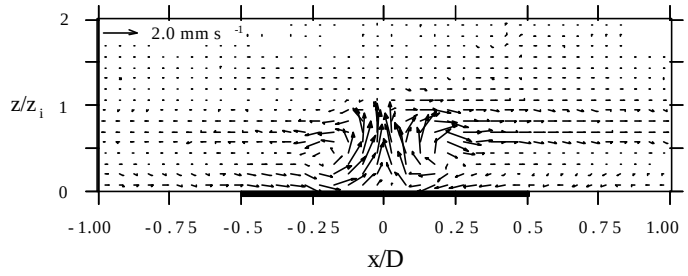

Fig. 3: Averaged velocity vectors for Case 4.A

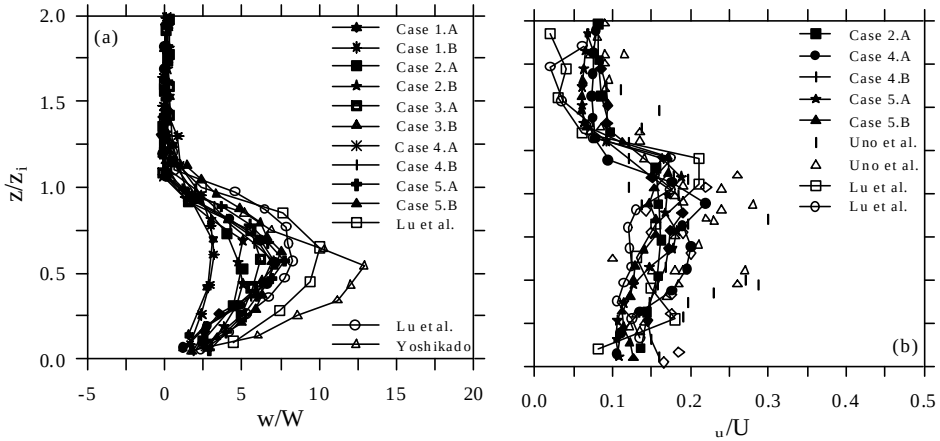

Fig. 4: (a) Profiles of nondimensional vertical velocities (x/D=0) for nocturnal (1.A 5.A) and diurnal conditions (1.B 5.B). Open symbols refer to [7] (squares: Fr=0.047, Re=3820; circles: Fr=0.077, Re=8280) and [6] (triangles: Fr=0.009, Re=4.8×10^9). (b) Profiles of nondimensional standard deviations of horizontal velocity (x/D=0) for the present study (full squares, circles and crosses: nocturnal cases; full diamonds and triangles: diurnal cases), the laboratory simulation of [7] and the field data of [8] (open diamonds: run 15; open triangles: run 17)

One of the fundamental characteristics of UHIs dynamics noted by [6] was the similarity between nocturnal and daytime UHIs. He found that their circulations were comparable if the sum $T_m + T_L$ had the same value (T_L was the surface temperature growth after sunrise, expressed as T_L-T_S, in our laboratory model). The mentioned similarity is of great interest in that it leads to the hypothesis that the

bulk convection model derived by [7], valid for nocturnal UHIs, might be extended to daytime UHIs. In that case, U and W would be appropriate velocity scales for daytime UHIs, too. In order to verify the above hypothesis, simulations of UHIs developing in statically unstable boundary layers, and comparison with nocturnal UHIs, are described here. The experimental approach was the following. First, in order to avoid influences from the sea side, a removable vertical partition was positioned along the coastline. Second, stratification was established above the land side by setting T_L=27 °C and T_U=46 °C. Then, the land side temperature rapidly raised to T_L=31 °C (an indirect estimation of the surface heat flux associated with this growth in temperature after that stationary conditions were established gave H_L 300 Wm^{-2}). As a result, a well-mixed layer formed above the land side. The last step was to switch on the electric heater. In so doing, the UHI developed within an unstable environment, taking on the features of a daytime UHI. The procedure was repeated for each one of the 5 values of H_0 listed in Table 1 (the corresponding situations were indicated with Case i.B, where i spanned from 1 to 5). Finally, the horizontal velocity scale U was calculated by using H_0+H_L. The shape of the diurnal UHI was similar to that observed for the corresponding nocturnal UHI, with a depth higher as compared with that observed for the nocturnal one caused by the presence of the well-mixed layer, which made the vertical development of the thermal plume easier. To verify the similarity between diurnal and nocturnal conditions, the vertical profiles of the normalized vertical velocities and the normalized standard deviation of the horizontal velocities calculated for the diurnal situations have been compared with those of the nocturnal ones previously discussed (Figs. 4a,b). The figures reveal a reasonable agreement among the curves, suggesting that both the velocity scales U and W were appropriate also for diurnal UHIs.

3.2 Daytime UHI – sea breeze interaction

In order to simultaneously generate the daytime UHI and the sea breeze regime (situation C), the experiments were made using the same procedure described in 3.1, although the vertical partition was removed from the shoreline. Thus, when the land side was heated a difference in temperature was established between the sea and the land surfaces. This disparity generated a horizontal pressure gradient directed offshore which, in turn, caused an onshore current (sea breeze) directed toward the UHI. In so doing, we simulated the interaction between an inland, daytime UHI and a pure sea breeze in case of flat terrain. A problem arose, however, with the small sea breeze velocity U_B 0.45 mms^{-1} attained in the experiments. In fact, the ratios U_B/U, for stationary conditions, fell in the range 0.08 to 0.13, while typical full-scale ratios are generally above 1. Nevertheless, [6] noted that composite systems of UHIs and sea breezes can be considered completely similar to those associated with UHIs and light gradient winds of velocity U_G, where the ratio U_G/U is commonly below 1. Thus, the results presented below are pertinent both to the interaction daytime UHI sea breeze flow and daytime UHI light gradient wind, even though for the former situation its natural counterpart is rather uncommon.

The averaged velocity field for Case 4.C is sketched in Fig. 5 It shows that the circulation lost its symmetry with respect to the heater axis, in contrast with that developed in calm environments. Furthermore, part of the sea breeze was blocked by the UHI and channeled seaward at elevated layers strengthening the upwind diverging flow associated with the urban plume, while part flowed over the plume. A noteworthy observation from the figure is the formation of a stagnation region in the lee of the UHI, in agreement with the numerical results given by [6]. Another salient feature was the leeward shift from the city center of the thermal plume, that is, the new position attained by the maximum upward velocity W_M. As noted by [6], the shift depended on the incoming sea breeze (or gradient wind) velocity, or rather on the ratio U_B/U. Fig. 6a presents measurements of x_{PA}/D as a function of U_B/U for the Cases i.C (i=1 5) and the corresponding results carried out by [6] in his analysis on the influence of gradient winds on UHI dynamics. Here x_{PA} is the landward displacement from the heater center of the thermal plume axis. Despite the fact that the ratios U_B/U encompassed by the two data sets were quite different, the curves appeared to show a similar trend, although our results were characterized by greater x_{PA}. Though the small number of data points did not allow for clearly defined conclusions, the results corroborated the numerical experiments of [9]. He noted that, when the city is located along the shore, the UHI circulation does not develop enough before the arrival of the sea breeze. In that case, the sea breeze

is not blocked by the thermal plume and flows above the urban complex. As a result, the UHI circulation does not show a well defined structure (see also [10]). On the contrary, if the city is located inland, its associated UHI circulation can reach a mature stage and retains its identity when interacting with the sea breeze, provided that the distance from the shoreline exceeds a certain value. A further comparison between this study and the numerical simulations of [6] is presented in Fig. 6b, where the normalized upward velocity maximum W_M/W as a function of U_B/U is given. As noted in the previous subsections, numerical and experimental velocity data exhibited a non-negligible discrepancy. Nevertheless, for low U_B/U, the two curves suggests that as U_B/U increased, so did W_M/W. In other words, UHI circulations associated with large U (i.e. large heat fluxes and/or large city diameters) kept on their identity with larger values of U_B. It has been conjectured [6] that the sudden drop of W_M when U_B exceeded a certain range was caused by the stronger advection which blew away the urban boundary layer as a whole.

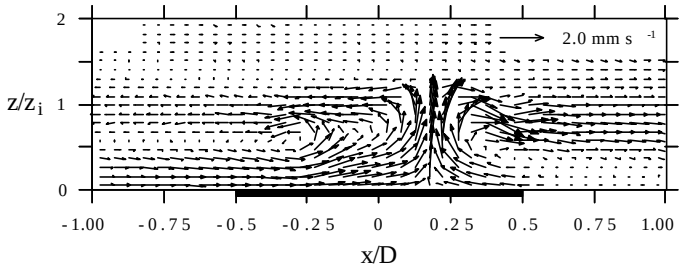

Fig. 5: Averaged velocity vectors for Case 4.C

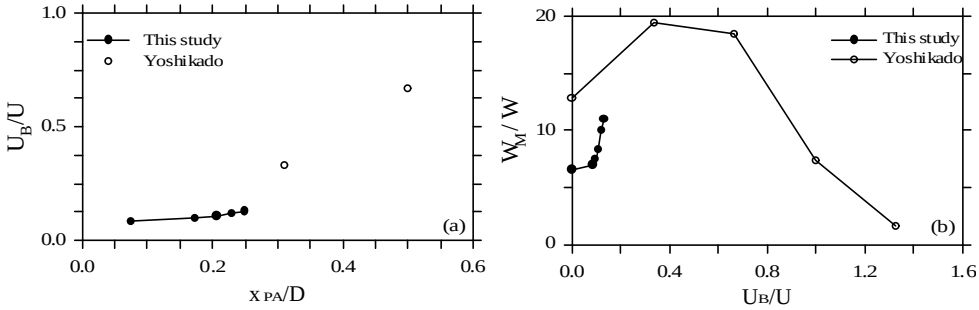

Fig. 6: (a) x_{PA}/D vs U_B/U for this study and for [7] numerical runs . (b) As in (a), but for W_M/W vs U_B/U

REFERENCES

[1] Oke TR: The heat island of the urban boundary layer: characteristics, causes and effects. In *Wind Climate in Cities*, JE Cermak et al., Eds., NATO ASI series E, Vol. **277**, Kluwer Academic, 81-107, 1995

[2] Lu J, Arya SP, Snyder WH and Lawson Jr. RE: A laboratory study of the urban heat island in a calm and stably stratified environment. Part I: temperature field. *J. Appl. Meteor.* 1997, **36**, 1377-1391

[3] Snyder WH: Guideline for fluid modeling of atmospheric diffusion. Rep. EPA-600/8-81-009, 1981, 1-200

[4] Cenedese A and Monti P: Interaction between an inland urban heat island and a sea breeze flow: A laboratory study. *J. Appl. Meteor*. 2003, in press

[5] Clarke JF: Nocturnal urban boundary layer over Cincinnati, Ohio. *Mon. Wea. Rev.* 1969, **97**, 582-589

[6] Yoshikado H: Numerical study of the daytime urban effect and its interaction with the sea breeze. *J. Appl. Meteor*. 1992, **31**, 1146-1164

[7] Lu J, Arya SP, Snyder WH and Lawson Jr. RE: A laboratory study of the urban heat island in a calm and stably stratified environment. Part II: velocity field. *J. Appl. Meteor*. 1997, **36**, 1392-1402

[8] Uno I, Wakamatsu S, Ueda H and Nakamura A: An observational study of the structure of the nocturnal urban boundary layer. *Bound.-Layer Meteor*. 1998, **45**, 59-82

[9] Yoshikado H: Interaction of the sea breeze with urban heat islands of different sizes and locations. *J. Meteor. Soc. Japan* 1994, **72**, 139-143

[10] Ohashi Y and Kida H: Local circulation developed in the vicinity of both coastal and inland urban areas: a numerical study with a mesoscale atmospheric model. *J. Appl. Meteor.* 2002, **41**, 30-45

Proceedings of the Tenth Asian Congress of Fluid Mechanics
17-21 May 2004, Peradeniya, Sri Lanka

FEASIBILITY OF DREDGING THE ENTRANCE CHANNELS OF NEGOMBO LAGOON TO IMPROVE THE FLOW OF WATER AND ITS QUALITY

SP Samarawickrama and SSL Hettiarachchi
University of Moratuwa, Sri Lanka

PC Fernando and WPK Egodawatta
Lanka Hydraulic Institute, Sri Lanka

ABSTRACT The paper presents the results from an Engineering Study on the Feasibility of Dredging the Negombo Lagoon to improve the flow of water and its quality. The purpose of the study was to improve the circulation in the lagoon to minimize further siltation and to achieve favourable conditions to sustain the rich biodiversity.

1. THE NEGOMBO LAGOON AND ITS ENVIRONMENT

The Negombo lagoon is a shallow coastal body of water located on the west coast of Sri Lanka (7^0 10' N and 79^0 50' E). It forms an integral part of the Muthurajawela marsh - Negombo lagoon coastal wetland, 6230 ha in extent (**Figure 1**). The lagoon is approximately 12.5 km in length and its width varies from 0.6 to 3.6 km. Its mean depth is estimated to be approximately 0.65 m and the surface area to be 35 km^2, thus placing its volume to be of the order of 22.5 million m^3. One of the unique features of the lagoon is that its transition to the sea consists of several narrow channels. The total cross-sectional area of the inlet channels is estimated to be 250 m^2 with a length of 2.5 km. This area of transition also serves as a principal anchorage for a large fleet of fishing vessels of different types.

The exchange of water in the lagoon is influenced by the tides from the ocean side and fresh water supply from the inland side. The tide is semi-diurnal and the tidal range in the lagoon varies in the order of 0.07m at neaps to 0.2m at springs, these values being about one third of tide at sea. Thus the volume of water stored and released varies between 1.5 million m^3 and 7 million m^3 per tide. Fresh water enters from the southern end of the lagoon through Dandugam Oya, Ja Ela and several streams from the Muthurajawela marsh. The supply of fresh water varies from virtually zero during the dry seasons to more than 100 cumecs during the rainy seasons. The lagoon and the entire wetland are separated from the sea by a narrow stretch of land consisting of a very fragile coastal dune system situated on beach rock formed during sea level changes over geological periods of time.

The Negombo lagoon and its coastal environment has had a long association with tourism and the fishery industry. One of Sri Lanka's leading beach resorts is located north of the Negombo lagoon inlet. The lagoon inlet serves as a principal coastal fishery anchorage for a fleet of fishing vessels and the lagoon estuarine fishery supports at least 3000 families from around 25 villages dispersed at the perimeter of the lagoon. Haphazard expansion of piers and landing points have contributed towards alterations in the flow patterns leading to sedimentation in the channel segments thereby affecting the control of flow into and out of the lagoon. Large quantities of solid and liquid waste are dumped at various locations in the lagoon resulting in pollution problems. This has resulted in the loss of vital functional parts of the eco-system including the flow channels and nursery areas. It is evident that unplanned development along the waterfront, reduction of tidal flow, siltation and pollution are major problems affecting the Negombo Lagoon. These have contributed to the overall degradation of the aquatic environment at the tidal inlet and within the lagoon. If this siltation

continues it will in the long-term, adversely affect the lagoon environment, in particular, its biodiversity.

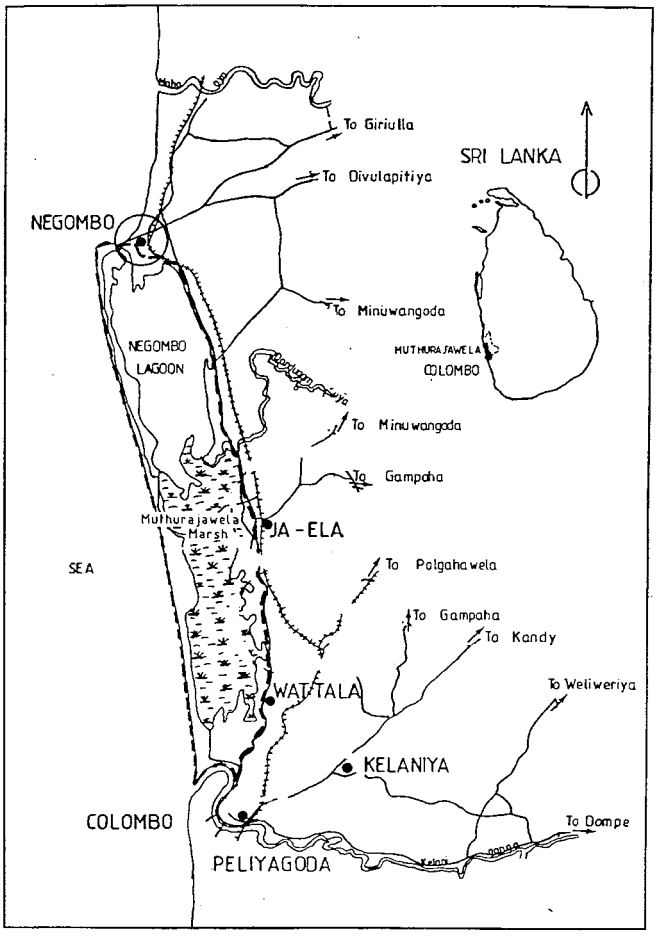

Figure 1 : Muthurajawela Marsh - Negombo Lagoon

2. APPROACH TO THE INVESTIGATIONS

Planning and implementing engineering interventions at the Negombo lagoon inlet and assessing its impact on the environment require as detailed an understanding as possible of the system to be managed. A review of natural conditions and human/development activities identified some of the problems, which affect the lagoon environment. It was clear that siltation of the lagoon and its inlet was a major issue, linked to most problem areas. In this context it was evident that the method of approach adopted should identify the lagoon inlet as an integral part of the aquatic system consisting of the main body of the lagoon on one side and the ocean on the other side. It is important to note that the entire tidal exchange between the ocean and the lagoon is restricted to flow beneath the two bridges at the inlet. The region between the bridges and the mouth is used extensively by fishing vessels and waves from the ocean propagate into this area.

The investigative strategy requires both qualitative and quantitative information leading to a clear understanding of natural changes of inlet stability. It also requires methods of predicting the manner in which

the hydraulic behaviour would respond to changes introduced by proposed engineering interventions. The priority need is to assess the likely impact or efficiency of the proposed interventions so that different options can be evaluated objectively, one against the other. In order to achieve this objective it is necessary to be able to simulate existing conditions within the system of interest and to predict, in quantitative terms, within acceptable levels of accuracy, the consequences of such interventions. In this context it is recommended to apply reliable mathematical models which is a powerful technique capable of integrating, by means of mathematical equations, the many diverse processes involved in the functioning of aquatic systems, thereby simulating such systems and predicting quantitatively the effects of changes in these systems.

The hydraulic behaviour of a tidal inlet was investigated in **three stages**. In the **first stage** an initial but sufficiently detailed assessment of the physical processes occurring at the inlet was made by studying existing information. This included

1) Historical information and data from different investigations carried out in the study area. These include information on previous schemes in the area and their impact on neighbouring regions.
2) Results of semi-quantitative conceptual models and preliminary modelling studies that rely on an understanding of the varying processes in the natural systems that affect the hydraulic regime.
3) Using results from case studies of similar situations from which likely impact of change can be inferred.

In the **second stage** attention was focused on planning and implementing field investigations to strengthen the existing information / data bank. The depth of these investigations depended entirely on the outcome of the first stage. A preliminary analysis of data indicates that although a large data bank exists for the Negombo Lagoon, most of the data have not been collected from a viewpoint of engineering studies and hence the same cannot be used directly for computations associated with the hydraulic behaviour for the inlet. The principal shortcomings of the data from an engineering viewpoint are the limited frequency of collection (sampling frequency), the limitations with respect to the points at which the data has been collected (spread of data points) and the absence of an interconnected grid for the sampling points. Sampling points at the bed have only been identified on plan and not related to the bathymetry. In order to study the hydrodynamic processes associated with sedimentation it is necessary to collect specific data at pre determined sampling frequencies over a particular time interval (for example spring tidal cycle).

In the **third stage** detailed mathematical modelling was implemented. Once the existing physical processes were fully understood and modelled, engineering interventions for improving the environment were formulated. The interventions were modelled to determine their efficiency and the input on the hydraulic regime. Such studies could then be used to assess the impact of the intervention on the aquatic and neighbouring environment.

3. FIELD INVESTIGATIONS

Extensive field investigations which were carried out comprise two components namely field surveys and deployment of data recording equipment at identified locations along the lagoon water body. Tables 1 and 2 summarize the two components.

Most recording equipment were deployed beyond the minimum required period. This enabled each of the parameters to be determined under varying combinations of the boundary conditions. Some instruments were in place for a long time so that the acquired data bear more meaning in the subsequent applications in the study. Such data banks provide a wider understanding of critical parameters and could be related to the long-term behaviour of the lagoon.

Table 1 : Summary of Field Survey Activities

Horizontal and Vertical Control Surveys
Topographic Survey of the lagoon periphery including islands/ shoals
Bathymetric Survey
Drogue Studies
Bed Sediment Sampling
Core Sediment Sampling
Flow, Salinity, Suspended Sediment measurements in the entrance channels
Discharge measurements in Dandugam Oya
Physical, Chemical and Microbiological Analysis
Biological Analysis

Table 2 : Summary of Deployment of Recording Equipment

WTG-Water Level Gauge (at lagoon entrance)
WTG- Water Level Gauge (in the main water body of the lagoon)
Salinity Meter (at the lagoon entrance)
Salinity Meter (at the lagoon southern end)
Current Meter with Salinity Sensor (at the westward lagoon channel)
Current Meter with Salinity Sensor (at the lagoon main water body)
Anemometer (wind measurements)
Tide gauge (at the southern end of the lagoon)

4. ENVIRONMENTAL CONSIDERATIONS

The high BOD levels at all locations sampled indicate that there is inflow of wastewater into the lagoon. The major point sources are Dandugam Oya, Ja Ela and Hamilton Canal. The quality of water in all three above point sources are poor, and indicates pollution by human waste. While the faecal contamination of the water within the lagoon is considerably less, the water in the two channels at the outlet into the sea, and in the environment of the mouth of the lagoon appears to be heavily polluted by human waste. In order to prevent further pollution of the lagoon and its environment it is imperative that sanitary facilities of the people living on the banks of the waterways and of the market and commercial establishments in the town near the mouth of the lagoon should be improved on a matter of priority.

The study also showed that the north eastern channel is more polluted, and there is very little flow in this channel, particularly during the dry season. Dredging of this channel would improve the flow through it, and coupled with interception of waste inflows, can be expected to improve significantly the quality of water in the lagoon.

5. ECOLOGICAL CONSIDERATIONS

The results of the present investigation indicate that there is no need for increased circulation in the western region of the basin segment of the lagoon because the COD, BOD_5, Ammonia –N and coliform levels are relatively low.

However, a recent survey carried out indicates that dense growths of aquatic macrophytes, which are usually present in habitats with heavy organic pollution and less circulation, are present in the north-eastern region of the basin segment, i.e, in Kurana and Kadolkele regions. This indicates that the water circulation in this region is poor. Therefore, it is necessary to increase the circulation in that area.

If all canals are dredged water exchange in all regions of the lagoon would be facilitated. This will enhance the migration of shrimp larvae and juveniles of popular food fish such as grey mullets, milk fish, sea

perches and leognathdds into the lagoon. With the dredging the mangrove habitats in the lagoon should be conserved and the denuded mangroved habitats should be reestablished in order to provide nursery grounds for these organisms. Therefore, with the increased recruitment of shrimps and fish due to dredging, all fisheries in the lagoon including brush park fisheries, encircling net fisheries and Kattu del fisheries would be benefited.

6. NUMERICAL MODELLING

MIKE 21 HD is the hydrodynamic module within the MIKE 21 modelling system that is used for the simulation of water levels and flows in estuaries, bays and coastal areas. It simulates unsteady, two-dimensional flows in one-layer (vertically homogeneous) fluids and has been applied in a large number of studies. MIKE 21 HD is based on the numerical solution of full non-linear equations of conservation of mass and momentum integrated over the vertical to describe flow and water level variations. MIKE 21 HD makes use of a so-called "Alternating Direction Implicit (ADI)" technique to integrate the equations for mass and momentum conservation in the space-time domain.

MIKE 21 ST is the sediment transport module for the assessment of sediment transport rates and related initial rates of bed level changes of non-cohesive sediment (sand) due to currents or combined wave-current flow. MIKE 21 ST calculates sediment transport rates on a rectangular grid covering the area of interest on the basis of the hydrodynamic data obtained from a simulation with MIKE 21 HD together with information about the characteristics of the bed material. MIKE 21 AD simulates the spreading of a dissolved or suspended substance in an aquatic environment under the influence of the fluid transport and associated natural dispersion processes. The substance may be a pollutant, which may be treated as conservative or subject to linear decay: salt, heat and dissolved/suspended contaminants. Similarly to the HD module, the concentration of the substance is calculated in each point of a rectangular grid covering the area of interest.

The wind velocity, tidal flows and river discharges were used to force the hydrodynamic model. Full scale measurements programme was carried out to obtain the information for model forcing and for model calibration. Accurate definition of the open sea tidal constituents at model boundaries is essential for the verification of the tidal propagation pattern in the area of interest. The constituents adopted in the present study were extracted from a previously performed tidal hydrodynamic study in which the already established open sea tidal constituents were further refined. The tidal constituents used in the study were calibrated with the measured surface elevations at the lagoon entrance. Wind measurements were carried out in one of the lagoon islands. In all computations time varying wind field was used, however wind was assumed to be uniform in space. Cumulative discharge from Dandugam Oya, Ja-ela and Hamilton Canal was used as a single point source for model forcing.

7. ENGINEERING INTERVENTIONS

7.1. Lagoon entrance channels

Average depth of the channels vary from about 0.5 m to 3.5 m. The length of the lagoon entrance channels is about 2.4 km and the cross sectional area varies from 500-650 m^2. Figure 2 gives the lagoon entrance channels showing the channel sections selected for model outputs. These model outputs are for the same period selected for model calibration.

Figure 3 gives the plan view of the entrance channels showing maximum flood discharges for the existing condition. It can be seen from the figure that there are three dominant flow paths (3-6-11, 3-5 and 3-14-9-12), which carry almost 90% of the flow.

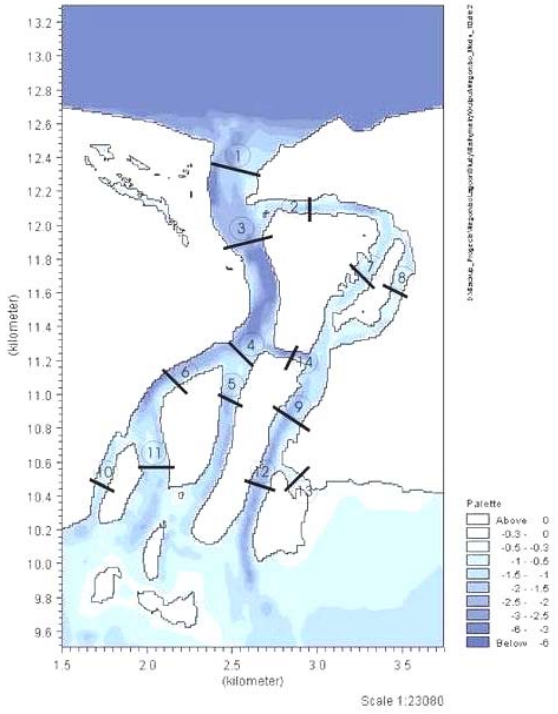

Figure 2: Lagoon inlet showing the selected channel sections for model studies

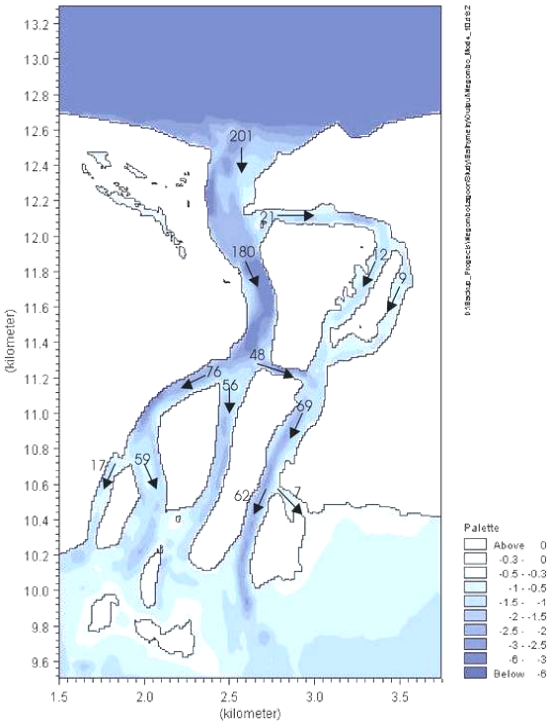

Figure 3: Maximum flood discharges (m^3/s) for existing condition

7.2 Dredging Scenarios

The inlet of the Negombo lagoon and the lagoon itself is subjected to sedimentation. As a result the water exchange between the sea and the lagoon has decreased, which is harmful for fresh-salt eco-system of the lagoon. The objective of the present study is to improve the circulation in the lagoon so that further siltation of the lagoon can be minimized and the water quality can be improved.

In the present study, 8 options were considered. Water exchange and the long-term sedimentation are considered as the most important criteria in the selection of the most feasible option. Stake net fishing in the lagoon entrance channels and other types of lagoon fishing and also the other user effects are given due consideration. Water circulation can be improved through the increase in the dredging quantity, which in turn will increase the cost involved.

Option 1: In this option channels 2 and 7 are dredged up to a depth of 1.5 m. There is a 33% increase of discharge in channel 2 and 92% increase in discharge in channel 7. Discharge through channel 8 has reduced by 44% and through the main channel 3 by about 3%. This option involves a total dredging volume of 60,000 m^3 and the total increase of discharge through the entrance channel system is only by 1%.

Option 2: In this option channels 2 and 7 are dredged up to a depth of 2.5 m. There is a 100% increase of discharge in channel 2 and 217% increase in discharge in channel 7. Discharge through channel 8 has reduced by 56% and through the main channel 3 by about 7%. This option involves a total dredging volume of 220,000 m^3 and the total increase of discharge through the entrance channel system is by 4%.

Option 3:In this option channels 2,7,9 and 12 are dredged up to a depth of 2.5 m. There is a 152% increase of discharge in channel 2 and 292% increase in discharge in channel 7. Channels 9 and 12 experiences an

increase in discharge of 45% and 50% respectively. Discharge through channel 8 has reduced by 33% and there is only a minor effect to main channel 3. This option involves a total dredging volume of 350,000 m^3 and the total increase of discharge through the entrance channel system is by 14%.

Option 4: In this option channels 2,7,9,12 and 13 are dredged up to a depth of 2.5 m. There is a 176% increase of discharge in channel 2 and 333% increase in discharge in channel 7. Channels 9 experiences an increase in discharge of 62% and there is no significant change of flow in channel 12. Discharge through channel 8 has reduced by 33% and there is only a minor effect to main channel 3. This option involves a total dredging volume of 540,000 m^3 and the total increase of discharge through the channel system is by 19%.

Option 5: In this option channels 6 and 11 are dredged up to a depth of 2.5 m. There is a 45% increase of discharge in channel 6 and 69% increase in discharge in channel 11. Discharge through the other 2 western channel segments 5 and 10 reduces by 11% and 41% respectively. There is a varying percentage reduction 5%-29%, through the eastern channel system and also reduction in flow through the cross channel 14 towards the eastern channel system. This option involves a total dredging volume of 315,000 m^3 and the total increase of discharge through the entrance channel system is by 9%.

Option 6: In this option both eastern and western channels are dredged up to a depth of 2.5 m. There is a 181% and 333% increase of discharge through two northeastern channels 2 and 7. Southeastern channel, number 9, provides an increase of 59% and there is no significant change in channel number 12. Channel 13, which provides water to the northeastern part of the lagoon water body, provides an increase of discharge from 7 to 47 m^3/s, a 571% increase. In the western channel segment, main channels 3 and 4 gives and percentage increase of 17 and 21 and the branches 6 and 11 provide a percentage increase of 45 and 66. Channels which are not subjected to dredging indicate decreases in discharge. This option involves a total dredging volume of 900,000 m^3 and the total increase of discharge through the channel system is by 34%.

Option 7: In this option both eastern and western channels are dredged up to a depth of 2.5 m and channel 12 was blocked to obtain a higher discharge through channel 13 in view of getting more water to the presently stagnant northeastern part of the lagoon main water body. Discharge through the channel 13 has increased from 7 to 78 m^3/s, a 1014% increase but the total increase of discharge through the entrance channel system has dropped to 25% from 34% (option 6).

Table 3 gives the summary of maximum flood discharges for the existing condition and different dredging scenarios. Existing condition is denoted by 0.

7.3 Comparison of Option-6 and the Existing Condition

Option 6 gives about 45-60% increase in tidal range in the lagoon water body. Existing condition gives a time lag of 4 hours and as a result of dredging time lag reduces up to about 2.5 hours, which contributes to the increase in tidal range mentioned above. Table 4 gives the cross sectional area, maximum flood flow discharge and maximum flood velocity for the existing condition and option 6. Table also gives the percentage increase /decrease in discharge and velocity as a result of dredging. It is clear from the table that there is a percentage increase in discharge in all channels except 5, 8 and 10, which are not subjected to dredging. Increase sedimentation in these channels could be expected as a result of the decrease in velocity. Dredging of these channels would not contribute greatly for the increase in total volume exchange but will be included in the dredging programme due to the stakeholder requirements. Channels 11 and 12 experience an increase in discharge and a decrease in velocity as a result of dredging. This small reduction in velocity could not be expected to give any adverse effects in relation to sedimentation. There is an 18% reduction of velocity in the main entrance channel but the magnitude of predicted velocity is still high enough to prevent increase in sedimentation. There is a 25-50% increase in volume exchange into and out of the lagoon.

The alternative proposals for dredging were presented to the stakeholders and each proposal was discussed at length identifying the relative merits/demerits. It was decided to adopt Option 6 with slight modifications to accommodate the issues raised by the stakeholders (Option 8).

Table 3: Maximum flood discharges (m^3/s) for different dredging scenarios

	Dredging Scenario								
	Channel Number	**0**	**1**	**2**	**3**	**4**	**5**	**6**	**7**
Main entrance channel	**1**	201	203	210	230	240	220	270	252
Western channel segments	**3**	180	175	168	177	182	200	211	202
	4	132	128	130	130	128	160	160	171
	5	56	52	54	54	53	50	50	55
	6	76	76	76	76	75	110	110	116
	10	17	17	18	17	18	10	12	12
	11	59	59	58	59	57	100	98	104
Eastern channel segments	**2**	21	28	42	53	58	20	59	50
	7	12	23	38	47	52	11	52	45
	8	9	5	4	6	6	9	7	5
	9	69	75	80	100	112	60	110	81
	12	62	67	73	93	64	55	63	3
	13	7	8	7	7	48	5	47	78
	14	48	47	38	47	54	40	51	31

Table 4 : Comparison of Discharge, Velocity and Cross sectional areas in entrance channel segments for Existing condition and Dredging Option 6

	Channel Number	**Existing Condition**			**Option 6**				
		Cross section (m^2)	Discharge (m^3/s)	Velocity (m/s)	Cross section (m^2)	Discharge (m^3/s) (m^3/s)	% increase in discharge	Velocity (m/s)	% increase in velocity
Main entrance channel	**1**	517	201	0.39	821	270	34	0.33	*-18*
Western channel segments	**3**	474	180	0.38	434	211	17	0.49	29
	4	349	132	0.38	349	160	21	0.46	21
	5	188	56	0.30	188	50	*-11*	0.27	*-10*
	6	228	76	0.33	254	110	45	0.43	30
	10	77	17	0.22	77	12	*-29*	0.16	*-27*
	11	228	59	0.26	392	98	66	0.25	*-4*
Eastern channel segments	**2**	82	21	0.26	133	59	181	0.44	69
	7	100	12	0.12	211	52	333	0.25	108
	8	76	9	0.12	76	7	*-22*	0.09	*-25*
	9	249	69	0.28	370	110	59	0.30	7
	12	196	62	0.32	214	63	2	0.29	*-9*
	13	38	7	0.18	96	47	571	0.49	172
	14	117	48	0.41	117	51	6	0.44	7

Option -8 which includes 1,250,000 m^3 of dredging provides a 43% increase in the total discharge. In addition to the channels 5, 8 and 10, wider areas between ebb deltas were included into the dredging programme to obtain a higher volume exchange. It has to be noted here that the increase of total discharge

from 34% to 43% is mainly due to the inclusion of the areas between ebb deltas into the dredging programme. Channels 8 and 10 experience an increase in discharge compared to the existing condition, giving satisfactory solution to stakeholder concerns.

An additional option (option -9) was considered to see the effectiveness of the selected dredging depth. In this option same area considered under option -8 was dredged to a depth of 2.0 m in view of reducing the dredging volume. Channels 8 and 10 maintained the increase in discharge at the required level but the total discharge through the entrance channel system drops down to 250 m^3/s from 288 m^3/s. This is only a 24% increase from the existing condition compared to 34% under option -6 and 43% under option -8.

Taking all the factors into account, it was decided to select option -8, which provides 43% increase in total discharge and includes 1,250,000 m^3 of dredging. There is about 45-60% increase in tidal range in the lagoon water body and 60-70% increase in volume exchange into and out of the lagoon. Existing condition gives a time lag of 4 hours and as a result of dredging time lag reduces up to about 2.5 hours, which contributes to the increase in tidal range mentioned above. This option also addresses the issues raised by the stakeholders.

The longitudinal velocity increases both on the western side and eastern side of the lagoon as a result of dredging. The percentage increase in velocity in the western side is about 40% and in the eastern side it is 75% (values are for lagoon mid reaches). Higher percentage increase at the eastern side of the lagoon body can be seen as a result of dredging the channel 13, which supplies water to this area. The circulation in the eastern side of the lagoon will improve up to the present conditions in the western side.

8. SEDIMENT TRANSPORT MODELLING

The prediction of sedimentation and its prevention at tidal inlets is one of the complex areas in coastal engineering practice. In order to identify methods of preventing sedimentation or limiting its impact it is essential to identify and confirm the source of the deposited material, its volume and the process by which it is moved into the tidal inlet. These processes may include wave and tidal action and inland drainage (fresh water discharge). Even more important is the impact of combined action of these processes.

Bed sediment movement for existing and dredging option 8 was modeled using MIKE 21 ST. The results indicate that there is hardly any effect of river discharge in channel bed movement. During the spring period bed movement can be seen in all the channels except channels 8 and 13 under the existing conditions. With the proposed dredging program there is a small change in the pattern of bed movement. Few channels experience an increase in bed movement whereas the others experience a decrease in bed movement. During the neap period there is hardly any movement of bed under the existing condition and only few changes can be seen with the proposed dredging program. Overall changes of sediment transport rates are quite small and it can be expected that the channels will reach a new equilibrium profile after the dredging.

It is evident that both inland drainage and tidal flow have a pronounced effect on the main body of the lagoon and its outlet. The impact of inland drainage has a greater effect in the regions within and closer to the tail whereas the impact of tidal flow has a greater effect in the regions within and closer to the outlet. Both land drainage and tidal flow introduce sediment laden discharge into the lagoon and the prevailing hydraulic regime is such that it encourages a large portion of the sediment load to settle within the main body of the lagoon and its outlet.

With the proposed dredging option it can be expected that suspended sediment will flush out easily especially under the high river flow conditions. Formation of ebb tidal deltas will continue and might initially happen at an increased rate as a result of the increase in volume exchange.

9. ADVECTION DISPERSION MODELLING

MIKE 21 AD module was used to predict the salinity distribution of the Negombo Lagoon after the proposed engineering interventions. First, AD module was applied for the existing condition and calibrated with both continuous and in-situ salinity measurements. Model was then applied for the proposed dredging option and compared the results with the existing condition. Modeling was carried out to simulate both wet and dry conditions.

In the dry conditions gradual salinity variation from over 31ppt at the mouth to about 22ppt at the tail end can be seen whereas under wet conditions major part of the lagoon experiences salinity values in the range of 5-10ppt and less than 5ppt. It is clear from the AD modeling results that salinity patterns before and after dredging is very similar and only higher movement of salinity bands can be seen as a result of higher volume exchange.

10. RESIDENCE TIME

Residence time of the lagoon under the existing and option 8 conditions were calculated for a early spring period with a low river discharge. Existing condition provides a residence time of 19.5 days where as under same conditions residence time for option 8 is around 14.5 days. About 25% reduction in residence time could be achieved with the proposed dredging option.

There is a significant variation of residence time with the variation of inland drainage and tidal levels. In the dredging option 8, dry-spring period provides a residence time of about 16 days and a wet-neap period provides a residence time of about 4 days. During the dry-spring period a higher water level variation of 0.6 m outside the lagoon mouth and a cumulative discharge of 5-45 m^3/s with an average of about 20 m^3/s from Dandugam Oya, Ja-ela and Hamilton Canal was used. To simulate a wet-neap period a low water level variation of 0.2 m outside the lagoon mouth and a cumulative discharge of 110 m^3/s was used.

11. CONCLUSIONS

The comprehensive investigative study provided a clear understanding of the problems associated with the Negombo Lagoon and in particular the influence of the very complex outlet of the lagoon. As a result of stakeholder consultations, field investigations and the modeling of the existing status the following problems were clearly identified.

- Reduced water exchange
- Increased sedimentation
- Low circulation in the eastern part of the lagoon, especially the north eastern part of the lagoon
- High pollution in the north eastern channel segment
- Insufficient depths for stake net fishing in some entrance channels

As specified earlier, a wide range of dredging options were considered. This was done in order to achieve the most economical solution which would give due consideration to increased hydraulic efficiency and dredging costs. Having considered relevant issues including those of the stakeholders Dredging option 8 was refined to achieve the specific objectives. This option includes,

- 1.25 million m^3 of dredging
- 43% increase in flood discharge
- 45-60% increase in tidal range
- Time lag reduces from 4 hrs to 2.5 hrs
- 60-70% increase in volume exchange
- 25% reduction in residence time

Overall changes of sediment transport rates are comparatively small and it can be expected that the channels will reach to a new equilibrium position after the dredging. Suspended sediment will flush out easily especially under the high river flow conditions. Formation of ebb tidal deltas will continue and might initially

happen at an increased rate as a result of the increase in volume exchange.

Salinity patterns before and after dredging are very similar and only higher movement of salinity bands can be seen as a result of higher volume exchange. Salinity modeling was carried out for the options which were ranked high in the list of preferred options. Therefore the proposed engineering intervention will not contribute to an undue stress on the species profile of the lagoon. The species will certainly have time to adjust to the nominal changes in salinity and will benefit from increased exchange volume.

It is emphasized that human related activities including agricultural run-off impose severe stress on the lower catchment areas covering Ja-ela and Dandugam Oya. Similarly, pressure arising from the urbanization processes within the heavily polluted lagoon outlet too impose adverse impacts on the overall hydraulic regime. It is clearly established that these aspects have to be considered within a broader environmental management framework to reap full benefits of the proposed engineering interventions. There is a strong need to introduce effective procedures for environmental management and in this context to educate the community and all stakeholders on the need to conserve the Negombo Lagoon and its environment.

The proposed engineering interventions will contribute to an appreciable increase in flood discharge, tidal range and volumetric exchange. However human interventions in the form of unauthorized reclamation, formation of bunds, barriers and obstructions to the channels will certainly reduce the overall efficiency of the engineering interventions. It is in this context that post dredging monitoring should be carried out in a planned manner. Regulation of development activities within the outlet area will have to give due consideration to these aspects.

ACKNOWLEDGEMENT

This paper is based on the work carried out under the Engineering Study on the Feasibility of Dredging the Negombo Lagoon to improve the flow of water and its quality for the Coastal Resources Management Project (CRMP). The authors wish to thank the CRMP for their assistance.

REFERENCES

(1) Conservation Management Plan - Muthurajawela Marsh and Negombo Lagoon. Wetland Conservation Project, Central Environmental Authority, and Euroconsult, Netherlands. Oct 1995.

(2) Environmental Profile of Muthurajawela and Negombo Lagoon.
Ed. Samarakoon, J. and van Zon, H. GCEC, Sri Lanka and Euroconsult, Netherlands. March 1991.

(3) Sedimentation in the Negombo Lagoon outlet Hettiarachchi, S.S.L.
Research Report, University of Moratuwa, 1995.

(4) Sedimentation in the Negombo Lagoon outlet, Terwel, L. and Vermeulen, J. Research Report of the Delft University of Technology conducted in collaboration with the University of Moratuwa, September 1994.

(5) Mathematical Modelling of Tidal Currents in the Negombo Lagoon, Sri Lanka.
Holmes, P. and Samarawickrama, S.P. Research Report, Imperial College, London. January 1996.

Proceedings of the Tenth Asian Congress of Fluid Mechanics
17-21 May 2004, Peradeniya, Sri Lanka

MODELLING OF SEA LEVELS, WATER EXCHANGE AND DISPERSION IN AN INTERMITTENTLY CLOSED TIDAL ESTUARY*:* CHILAW LAGOON, WEST COAST OF SRI LANKA

E.M.S. Wijeratne
Oceanography Division, National Aquatic Resources Research and Development Agency, Colombo, Sri Lanka

L. Rydberg
Department of Oceanography, University of Gothenburg, Sweden

K.P.P. Pathirana
Faculty of Engineering, University of Peradeniya, Sri Lanka

ABSTRACT: Sea levels, water exchange and dispersion in an intermittently closed tidal inlet (Chilaw Lagoon) are examined using measurements and a high-resolution numerical model. Sea levels and salinities in the lagoon are strongly influenced by seasonal variations in river discharge and intermittent sandbar formation at the mouth. The lagoon salinity varies from zero to about 35 psu, while the range in mean sea level exceeds 0.5 m. When the mean sea level within the lagoon maximises at 0.4 m above the oceanic, the tide is almost extinguished. A combined 1-D and 2D barotropic tidal model, with a C_d of 0.0022, shows good agreement with the measured sea levels**.** Adding a salt flux equation to the model, gives reasonable agreement between predicted and observed salinities. The residence time was estimated by using a Lagrangian particle-tracking method. Simulations were carried out for different inlet configurations and different river discharges. Low river discharge and sandbar formation restrict the water exchange and result in longer residence times. The model can be used to predict the ecological state of the lagoon as well as the effect of any engineering undertakings at the inlet.

1. INTRODUCTION

Chilaw Lagoon is an intermittently closed small tidal lagoon (Fig.1) on the west coast of Sri Lanka. The lagoon is 4 km long and the average width is 1.6 km. The lagoon is shallow with an average depth of 1.1 m from MSL. It is connected to the open ocean through two narrow and long restricting channels, located at the extreme north and south ends of the lagoon. The length of the northern channel is 8 km with an average width of 80 m and a mean depth of 1.5 m. The southern channel is 5.5 km long with an average width of 20 m and an average depth of 1 m. The southern entrance is mostly closed, due to sandbar formation at the mouth (Thoduwawa). The topography at the northern entrance varies frequently due to formation and movement of sandbar [4]. Even the northern entrance may close intermittently particularly during summer when the river discharge is low. However, the mouths are generally kept open by dredging to avoid floods upstream and also to allow for boat traffic. Over 7000 fishing boats are daily passing the entrance to Chilaw Lagoon [4].

There are no rivers discharging directly into Chilaw Lagoon. However, the lagoon occasionally receives freshwater from the rivers namely, Deduru Oya and Lunu Oya. Lunu Oya discharges water to the southern channel with an annual mean discharge of 8 m^3s^{-1}, a part which is discharged to the sea when the southern outlet is open. Deduru Oya with an annual mean discharge of 36 m^3s^{-1} [1] enters the sea, where the northern channel also meets the sea (Fig.1). Freshwater from Deduru Oya may enter the lagoon during periods of sandbar formation at the mouth.

Prawn farming has become quite popular in this area, particularly long inlet channels on the northwest coast [5]. The area of prawn farms has gone up by 48% during 1994 to 1998 [7]. This may have resulted severe environmental and ecological problems to the coastal waterways. The fish catch from the lagoon per unit effort has dropped by 4 - 1.5 Kg between 1994 and 1997 [11]. Today, however, the prawn farming suffers from wide spread viral diseases, such as white spot, probably because of an uncontrolled settlements. Over establishment of farms has resulted in lack of freshwater supply to the

lagoon leading to low water exchange and hence, polluting the lagoon water body. This problem has been further aggravated due to pesticides and/or abnormally high nutrient concentrations and even oxygen deficit in the lagoon [6].

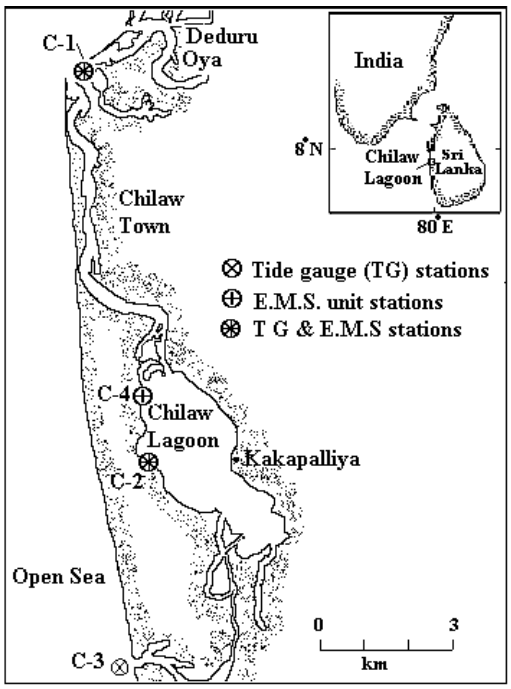

Several major activities have been proposed in the Chilaw Lagoon system; such as, an anchorage for fishing boats in the northern entrance channel by Ceylon Fishery Harbour Co-operation [9] and opening of southern entrance of the lagoon permanently to improve water exchange for the prawn farms [13]. There is also a proposal to construct a dam upstream of Deduru Oya and to divert a part of the river into irrigation water tanks further north (Mutupanthi Lakes).

In this study, a combined 1D and 2D hydrodynamic model is developed for the river -lagoon system in order to study the water exchange and circulation and to assist the prediction of water quality and management strategies. The model is calibrated and validated using a comprehensive set of field data on salinities and sea levels obtained in 1998. The following sections present the detailed description of field measurements, model set-up, model calibration and validation. The model is capable of predicting sea levels and salinities in the lagoon due to the oceanic tides and freshwater supply.

Fig. 1: Map of Chilaw Lagoon (E.M.S. stations are used for continuous recording of salinities and temperatures).

2. FIELD MEASUREMENTS

Sea level, salinity and temperature measurements were taken at several stations in the lagoon during 1998. The sea level measurements were carried out with Micro Tide pressure gauges from Coastal Leasing, USA with an absolute accuracy of ±1.5 cm. Time series of salinity and temperature variations were taken using an Aanderaa Environmental Monitoring System (EMS). This instrument was equipped with a sensor, which measures salinity and temperature with an absolute accuracy for salinity measurements of about ± 0.1 PSU and for temperature ± 0.1^{o}C. Data were recorded at 10 min intervals.

Tide gauges and EMS units were deployed at several locations in the lagoon and at the entrance channel and the locations were selected so as to specify model boundary conditions and to collet data for model calibration and validation at control points. The locations of the instruments are shown in Fig. 1 and deployment periods in Table 1.

The periods covered for sea level measurements include different conditions of the Chilaw Lagoon; one where both the northern and southern entrances were open, other periods when only the northern entrance was open. Both entrances were opened during the period of 3rd to 23rd April, and tide gauges were deployed at stations C-3 and C-2. From 26th April to 4th June, only the northern entrance was opened and tide gauges were deployed at stations C-1 and C-2. During next period from 17th July to 26th August, also only the northern entrance was open and the tide gauges were deployed at C-2 and C-3. During these latter periods, freshwater from Deduru Oya entered the lagoon through the northern entrance channel. EMS units for salinity measurements were installed at three stations during several periods (Table 1). Air pressure, rainfall and evaporation data were obtained from the Chilaw Weather Station. Air pressure data were available twice a day (at 9 and 15 hrs), rainfall and pan evaporation data on a daily basis (from Meteorology Department), but unfortunately, no discharge measurements were available for this period.

Recent bathymetry maps of the lagoon prepared by National Hydrographic Office were used for the model runs.

Table 1: Periods of field measurements (for positions of instruments see Fig.1).

Instrument	Duration of measurements			
	C-1	C-2	C-3	C-4
Tide gauge	26 April-4 June, 98	03-23 April, 98 26 April- 4 June, 98 17 July- 26 Aug, 98	03-23 April, 98	
EMS	30 April-21 Aug, 98	13 Jan- 22 Apr, 98, 30 April- 26 Aug, 98 21 Aug – 28 Sep, 96		16 Mar- 19 April, 98

3. MODEL DESCRIPTION

3.1 Formulation

With the complex nature of the lagoon mouth, mathematical formulation of the proposed model has to be based on a 2-D representation, where as, 1-D representation is appropriate for entrance channel and the basin. Thus, river and lagoon are modelled as 1-D channels with variable widths and cross-sectional areas and incorporated into the 2-D model. The 2-D model uses a semi implicit numerical scheme to solve depth-averaged momentum and continuity equations in a space staggered grid system [12].

$$\frac{\partial U}{\partial t}+U\frac{\partial U}{\partial x}+V\frac{\partial U}{\partial y}=-g\frac{\partial \eta}{\partial x}-\frac{1}{\rho_o}\frac{\tau_{xb}}{D} \quad (1)$$

$$\frac{\partial V}{\partial t}+U\frac{\partial V}{\partial x}+V\frac{\partial V}{\partial y}=-g\frac{\partial \eta}{\partial y}-\frac{1}{\rho_o}\frac{\tau_{yb}}{D} \quad (2)$$

$$\frac{\partial \eta}{\partial t}+\frac{\partial (DU)}{\partial x}+\frac{\partial (DV)}{\partial y}=0 \quad (3)$$

Where U and V are the depth-averaged velocities in the x and y directions respectively, $D=H+\eta$ the total water depth, H the undisturbed depth, t is time, ρ is water density, η is sea level, g is gravitational acceleration. τ_{xb} and τ_{yb} are the bed stresses in the x and y directions, respectively. Assuming a quadratic dependence, the kinematic bottom stress expressed as, $\tau_x^b=\rho_o C_d U\left(U^2+V^2\right)^{1/2}$ and $\tau_y^b=\rho_o C_d V\left(U^2+V^2\right)^{1/2}$ [8], with C_d as the dimensionless drag coefficient. The boundary conditions for the above equations were taken as; $x = 0$; $\eta=\eta_0(t)$ and zero fluxes through coastal boundaries. The initial condition is $t = 0$; $\eta = 0$ and $U = V = 0$.

The 1-D model is based on cross-sectionally averaged momentum and continuity equations [12].

$$\frac{\partial Q}{\partial t}+\frac{1}{A}Q\frac{\partial Q}{\partial x}=-gA\frac{\partial \eta}{\partial x}-\mathrm{B}\frac{1}{\rho_o}\tau_x^b \quad (4)$$

$$\frac{\partial \eta}{\partial t}=-\frac{1}{B}\frac{\partial Q}{\partial x} \quad (5)$$

Where Q is the cross-sectionally averaged volume flux, B the cross-sectional width, $A = B\times D$ the cross-sectional area. The bottom stress, τ_x^b is defined as $\tau_x^b=\rho_o C_d\frac{Q}{A}\left|\frac{Q}{A}\right|$ [10].

The boundary conditions are; $x = 0$; $\eta = \eta_0(t)$ and no volume flux through head $x = L$; $Q = 0$. The initial condition of the model is taken as, $t = 0$; $\eta = 0$ and $Q = 0$.

The velocity (and/or volume flux) points were placed at the transition between the1-D and 2-D models, so that depth-averaged velocities calculated by the 2-D model are converted to volume fluxes and then, these fluxes were used to drive the 1-D model. Similar approach was adopted when specifying the boundary condition at the transition of the 2-D model, where the volume fluxes computed by the 1-D model were converted to depth-averaged velocities.

3.2 Calibration and Validation

Sea level measurements from 30th April to 28th May were used for model calibration. The model was driven by the observed sea levels at the open sea. Model predicted water levels in the lagoon were compared with the field measurements. The time interval, Δt was chosen to be 10 sec, which satisfies with the stability criteria of both the 1-D and 2-D models. The sea level data at every 10 sec interval were derived from linear interpolation of the 10-min gauge data at open sea. Several trial runs were performed with C_d values ranging between 0 and 0.006.

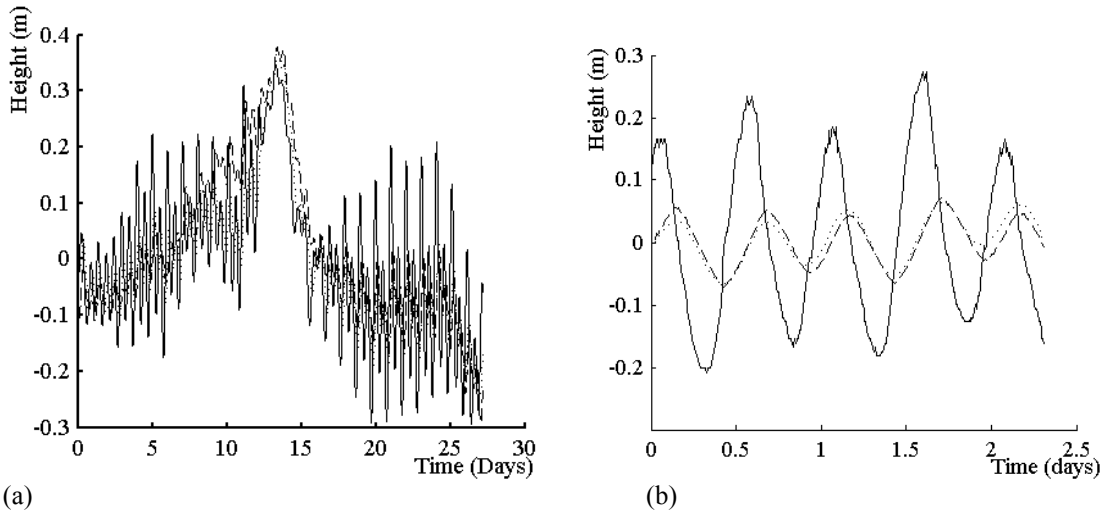

Fig. 2: Comparison between predicted and observed sea levels at station C-2 in Chilaw Lagoon (a) with one entrance open, 30th April-28th May 1998, and (b) both entrances open, 13th – 15th April 1998. The solid line is the sea level at station C-1, i.e. the model boundary condition. Dash line indicates the observed sea level at station C-2 and the dotted line is the model predicted sea level at station C-2.

The simulations show that higher C_d values produce gradually smaller tidal ranges and larger phase lags in the lagoon compared to measured values. The coefficient of 0.0022 gave the best agreement between the predicted and measured values. Figure 2(a) shows a comparison of predicted and measured water levels at Stn C-2. The model validation was done using the sea level measurements during 3rd to 23rd April 1998. No further adjustments were made to the C_d and the models predictions were validated using the measured sea levels at station C-1. A comparison between the predicted and observed sea levels is shown in Fig. 2b.

4. RESULTS

4.1 Sea level

The variation of water level outside and inside the lagoon (Fig.2) shows that the tidal range is reduced by more than 70%. During the periods when both entrances are opened (26th April-18th May 1996), the tidal range is slightly higher as compared to the period when only the northern entrance is opened. The average ebb period is about 20% longer than the flood period. The average high water phase lag between the ocean and the lagoon is about 3.2 hrs, whereas the average low water phase lag is about 3.5 hrs. These figures indicate a finite amplitude effect on wave progression [3]. There is a profound influence on the mean sea level during periods of low salinity (high river discharge). The mean sea level was more than 50 cm above MSL for a couple of days in May and the tide was almost extinguished, as shown later in Fig. 4. The river normally enters the open ocean near the mouth of the northern channel but during river floods freshwater obviously finds its way into Chilaw Lagoon. Figure 3 illustrates the predicted mean sea levels inside the lagoon for different situations. High river discharge and sandbar formation have resulted in higher mean sea level in the lagoon.

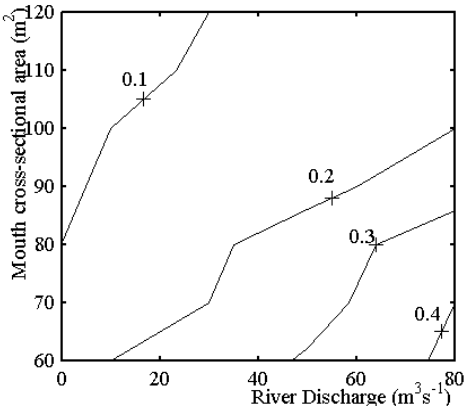

Fig. 3: The variation of mean sea level predicted by the model for different river discharges and inlet topography.

4.2 Salinity

The salinity in Chilaw Lagoon varies strongly over a year; from almost zero to a value even higher than the ocean salinity (Fig.4). Minimum and maximum salinities in the lagoon during 1998 were 1.5 psu and 35.8 psu, respectively. Annual average evaporation (1650 mm) in the area is higher than the annual precipitation of 1375 mm [2] and hence, with no freshwater input, it can be expected that the lagoon water will be hyper-saline during the periods of droughts. The total precipitation and evaporation from January to August 1998 were about 700 mm and 1000 mm, respectively and the mean salinity in the lagoon during the same period was about 15 psu. This low salinity levels in the lagoon were mainly due to draining of freshwater from Deduru Oya and Lunu Oya into Chilaw Lagoon. Figure 4 also shows that during high mean sea levels in the lagoon, salinities are low and vice versa. Salinity measurements at station C-1 show the influence of river discharge and tidal flux on lagoon water. When the river discharge is low, the daily variation of salinity in the lagoon is dominated by tide.

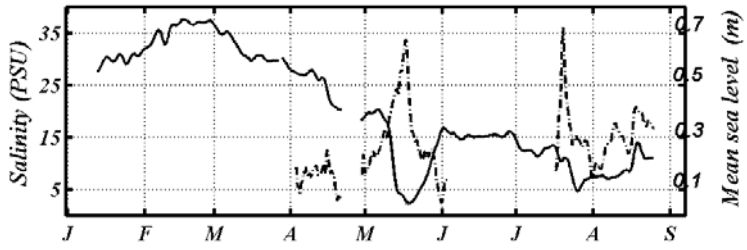

Fig.4: Salinity (solid line) and sea level (dotted line) variations from January to September1998.

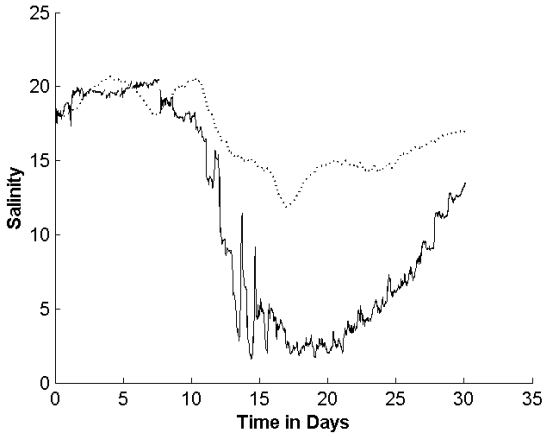

In order to simulate the salinity variations, a salt transport equation was incorporated into the model. Introducing volume flux, Q and the cross-sectionally averaged salinity, $\bar{s}$ the salt balance equation reads as;

$$\frac{\partial \bar{s}}{\partial t} = -\frac{Q}{A}\frac{\partial \bar{s}}{dx} + \frac{\partial}{\partial x}(K_x \frac{\partial \bar{s}}{\partial x}) \qquad (6)$$

Salinity measurements at station C-1 were used as the open boundary condition. The comparison between the observed and model simulated salinities at station C-2 that is located inside lagoon, are shown in Fig.5.

Fig. 5: A Comparison between the observed (full-drawn) and predicted (dotted) salinity variations at station C-2 for a constant discharge of 40 m^3/s.

4.3 Dispersion and flushing

A particle-tracking method was applied to study dispersion and residence time in the lagoon under different situations. The particle position at each time step was computed using the velocity field generated by the hydrodynamic model and a fourth order Runge-Kutta integration scheme. The particles are free to move between the grid points and therefore, the velocity field computed by the hydrodynamic model was interpolated for the instantaneous particle positions prior to the integration. By varying river discharge and inlet topography, several model runs were carried out to estimate the average residence time in the lagoon, as indicated in Fig. 6. Low river discharge and sandbar formation generally restrict the water exchange, which eventually result in longer residence times**.** The average residence time varies from 5 days to more than three weeks.

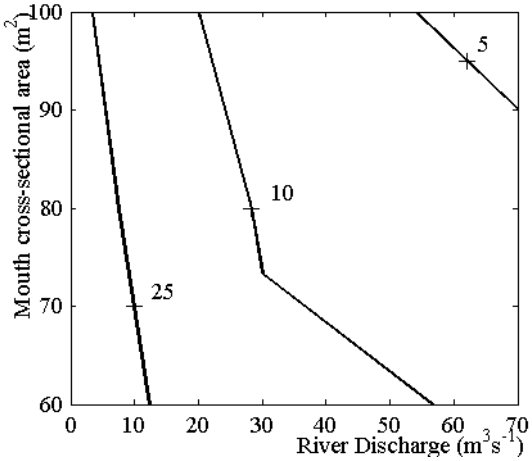

Fig. 6: Model simulations for average residence time (days) for different river discharges and inlet topography.

5. DISCUSSION

In Chilaw Lagoon, the maximum rise of mean sea level due to river discharge is found to be more than 50 cm above the ocean level. Such a strong discharge is likely to cause stratification, particularly during neap when mixing slows down, and thus, circulation. Several processes that are taking place at the inlet area will change the flow characteristics, including the change of flow from barotropic to baroclinic. It is obvious that such a change will affect the drag coefficient (C_d) used in the models. Therefore, the results presented in Fig.5 are influenced by these factors.

In addition, the baroclinic forcing caused by the horizontal salinity gradient was not considered in this study. This force will reduce the time taken for salt particles to reach the inner end of the Lagoon. Assuming that the baroclinic force is balanced by bottom friction as;

$$B\frac{1}{\rho_o}\tau_x^b = gAD\beta\frac{\partial \bar{s}}{\partial x},$$

an advective velocity scale, $u = (\tau / \rho_o)^{1/2}$ can be estimated, and which can be used to compare with the diffusive salt flux. This velocity was estimated to be in the order of 1 cm/s, according to the values used in the applications, which indicates that the forcing caused by the initial salt gradient is as efficient as the tidal mixing.

The difficulties mentioned above, related to lack of discharge measurements and the problems of handling gravitational circulation due to freshwater input, are not seriously affecting the results on residence time (Fig. 6). In all practical applications, it is important to apply the model during the periods of poor water exchange, when there is no or small freshwater discharge into the lagoon. Under such circumstances, the model is likely to behave very well (Fig. 2) and therefore, the simulated results on residence times shown in Fig. 6 are justifiable.

6. CONCLUSIONS

A combined 1D and 2D model has been developed and applied to Chilaw lagoon in order to simulate sea levels, salinities and residence times in the lagoon based on the observed data from the ocean side. The results of model calibration and validation indicate that the model is capable of simulating the sea level and salinities within the lagoon in a reasonable way. The lack of discharge measurements was one of the major difficulties faced during model simulations, and to overcome this, a constant discharge of freshwater had to be assigned in model applications. The results of model validation indicates that the model performance are highly convincing, although the model does not show any significant effect of discharge on sea level variation in the lagoon during the simulation period.

ACKNOWLEDGMENTS

Field Measurements were conducted under SIDA/SAREC/NARA coastal ecological programme with assistance of oceanography division staff, NARA.

REFERENCES

[1] Amarasinghe, U.A., Mutuwatta, L. and Sakthivadivel, R., "Water scarcity variations within a country: A case study of Sri Lanka". Research Report 32. Colombo, Sri Lanka, 1999.

[2] Arulananthan, K., "Hydrography, coastal water circulation and classification of Sri Lankan Lagoons". Ph.D. Thesis, PGIS, University of Peradeniya, Sri Lanka, 2003.

[3] Aubrey, D.G and Speer, P.E., "A study of non-linear tidal propagation in shallow inlet/estuarine systems", part 1: observations. *Estuarine, Coastal and Shelf Science*. 1985,**21**,185-205.

[4] Baranasuriya, P.W., "Hydrographic investigations for the design of an anchorage in a complex lagoon estuary", A Spatial Odyssey, 42nd Australian Surveyors Congress, 2001

[5] Corea, A.S.L.E., Jayasinghe, J.M.P.K., Ekaratne, S.U.K. and Johnstone, R.W., "Environmental impact of prawn farming on Dutch Canal: The main water source for the prawn culture industry in Sri Lanka". *Ambio*, 1995, **24**, 423-427.

[6] Corea, A.S.L.E., Johnstone, R.W., Jayasinghe, J.M.P.K., Ekaratne, S.U.K. and Jayawardene, K.G.M.J., "Self-pollution: a major threat to the prawn farming industry in Sri Lanka", *Ambio*, 1998, **27**, 662-668.

[7] Dahdouh-Guebas, F., Zetterstrom, T., Onnback , P.R.,Troell, M., Wickramasinghe., A and Koedam, N., "Recent changes in land-use in the Pambala–Chilaw Lagoon Complex (Sri Lanka) investigated using remote sensing and GIS: conservation of Mangroves Vs. development of Shrimp Farming", *Environment Development and Sustainability*, 2002, 4, 185-200.

[8] Dronkers, J.J. (1969), "Tidal computations for rivers, coastal areas and seas", Journal of Hydraulics Division, 95, 44-77.

[9] LHI, “Chilaw anchorage flushing study”, Interim report, LHI-96-2, Lanka Hydraulic Institute, Sri Lanka, 1997.

[10] Speer, P.E. and Aubrey, D.G., “A study of non-linear tidal propagation in shallow inlet/estuarine systems”, part II: theory. *Estuarine, Coastal and Shelf Science*. 1985, **21**,207-224.

[11] Wickramasinghe, A., “Progress review – mangrove conservation programme in Pambala Lagoon”, Small Fishers Federation, in Proceedings of the Workshop on Conservation and Management of Mangrove Ecosystems, Mangrove Conservation and Demonstration Centre, Small Fishers Federation,Pambala-Kakkapalliya, Sri Lanka, 1997, pp. 9–11.

[12] Wijeratne, E.M.S. ,”Tidal Characteristics and Modelling of Tidal Wave Propagation in Shallow Lagoons of Sri Lanka”, Ph.D. Thesis, PGIS, University of Peradeniya, Sri Lanka, 2002.

[13] Wijewardane, K.D.D., “Sustainable development of the Dutch Canal and related water bodies”. Study report and proposal submitted to North-Western provincial council, Sri Lanka, 2000.

Proceedings of the Tenth Asian Congress of Fluid Mechanics
17-21 May 2004, Peradeniya, Sri Lanka

BIWEEKLY OCEAN CURRENT FLUCTUATIONS SOUTH OF SRI LANKA

D. Sengupta and R. Senan
Centre for Atmospheric and Oceanic Sciences, Indian Institute of Science, Bangalore 560012, India

V. S. N. Murty
Physical Oceanography Division, National Institute of Oceanography, Dona Paula, Goa 403004, India

ABSTRACT: Observations of east-west (zonal) currents in the upper ocean south of Sri Lanka exhibit large fluctuations with a dominant 10-20 day ("biweekly") period. Current meter observations at the equator in the central and east Indian Ocean show biweekly oscillations in the north-south (meridional) ocean currents. An ocean model driven by daily surface winds reproduces the observed fluctuations of ocean currents. We show using the ocean model that the oscillation is associated with waves with biweekly period, 4000-5500 km zonal wavelength and westward phase propagation. The horizontal structure of the waves is similar to that of equatorially trapped mixed Rossby-gravity (MRG) waves.

1. INTRODUCTION

A mooring with six subsurface recording current meters (Aanderaa RCM) was deployed at 0°, 93°E in February 2000 by the National Institute of Oceanography, Goa under the Ocean Observing Systems Programme of the Department of Ocean Development (DOD), New Delhi [1]. In December 2000, this mooring was re-deployed and another mooring was installed at 0°, 83°E. The observations from these moorings, last retrieved in March 2002, are the first long time series of subsurface currents from the eastern equatorial Indian Ocean (EqIO). The observations show continuous 10-20 day, or biweekly, oscillations of meridional velocity. Recent measurements from a moored ADCP at 90E on the equator are consistent with the present observations they show prominent biweekly variability of *v* in the upper 400m, with a spectral peak at 12-day period [Yukio Masumoto, personal communication]. In this study, we focus on the nature and genesis of this distinct biweekly variability.

Evidence of 10-20 day variability has been found in previous observations of horizontal currents in the central and eastern EqIO. It has been suggested, based on the 1973-1975 current records from Gan Island (0°41`S, 73°10`E), that there might be variability with periods shorter than 20 days in the central EqIO [2]. The first clear demonstration of biweekly variability came from observations in the eastern half of the EqIO in the 1990's. Schott and his co-workers observed a distinct 15 day oscillation of equatorial *v* and off-equatorial *u* from moored current meter arrays along 80.5°E south of Sri Lanka [3,4]. In this study we use an ocean general circulation model to show that that the biweekly oscillations in the observations are consistent with the presence of wind forced equatorially trapped MRG (Yanai) waves which have an equatorial *v* maximum and off-equatorial *u* maxima (Figure 1); *u* is antisymmetric about the equator.

2. MODEL SETUP

We use the Modular Ocean Model [5] set up for the Indian Ocean basin between 30°S-30°N and 30°E-110°E, with horizontal resolution of 1/3° 1/3° north of 5°S. There are 19 levels in the vertical, six of which are in the top 100 metres. Horizontal eddy diffusivity and viscosity are 2000 m^2 s^{-1}.

Vertical mixing is based on the scheme of Pacanowski and Philander [5]. Ocean bottom topography is based on the 1/12° 1/12° resolution data from the U.S. National Geophysical Data Center. Surface temperature and salinity fields are relaxed to the observed seasonal cycle. The model ocean is driven at the surface by daily wind stress.

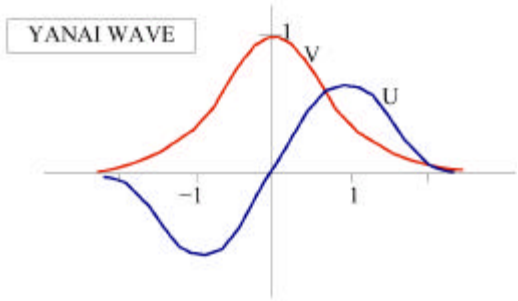

Fig. 1: Meridional structure of MRG (Yanai) wave. *v* is symmetric about the equator, *u* is antisymmetric about the equator. The distance is in units of Rossby radius.

3. COMPARISON WITH OBSERVATIONS

The observed volume transport in the upper 300 metres across an array of moored current meters south of Sri Lanka [3], and the corresponding transport from the model are shown in Figure 2. The generally westward flow in winter is associated with the North-east Monsoon Current and the eastward flow in summer with the Southwest Monsoon Current (SMC). It is important to note that the intraseasonal fluctuations in the model transport are in phase with the larger of the observed fluctuations. The amplitudes are generally smaller in the model. Comparison with vertical profiles of observed currents shows that model upper ocean currents are systematically weak, perhaps due to limitations in model horizontal or vertical mixing.

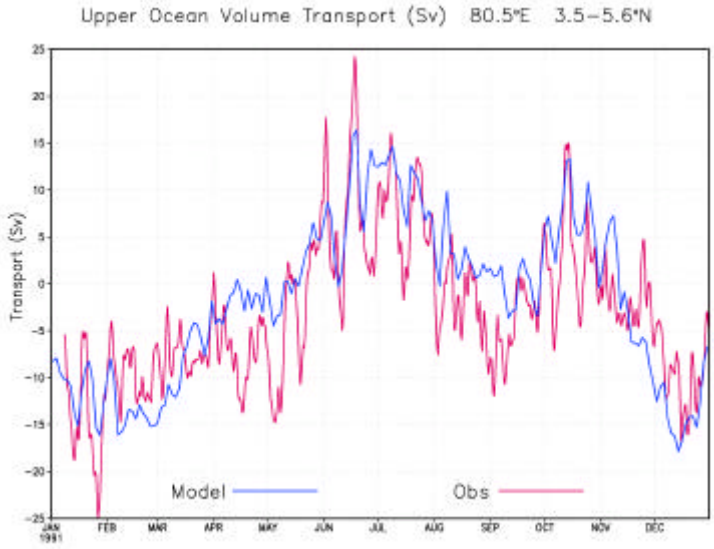

Fig. 2 Transport in Sverdrup (1Sv = 10^6 m ^{3} s ^{1}) in the upper 300m across a section (3.5-5.6°N) along 80.5°E south of Sri Lanka from the observations (red) and the model (blue).

Daily *v* for 2001 from the shallowest current meter at 93°E is shown in Figure 2a, together with daily meridional velocity at the mooring location from the model, interpolated to the daily instrument depth. Figure 3b,c,d shows similar comparisons of 10-20 day filtered *v* at 106m, 265m and 465m. Simulation of the biweekly variability is reasonably accurate at least in the upper 500m at this location, as well as at 83°E (not shown). Daily *v* from a model run forced by the seasonal cycle of daily winds at the mean current meter depths are also shown in Figures 3b,c,d. The biweekly oscillation is absent in this run, demonstrating that it is forced by intraseasonal wind variability. However, there is some intraseasonal variability of currents in this run, particularly at the uppermost level, although the wind stress used to force the model has no intraseasonal variability. This variability must be generated by dynamic instability of seasonal currents. However, it has dominant periods longer than 20 days.

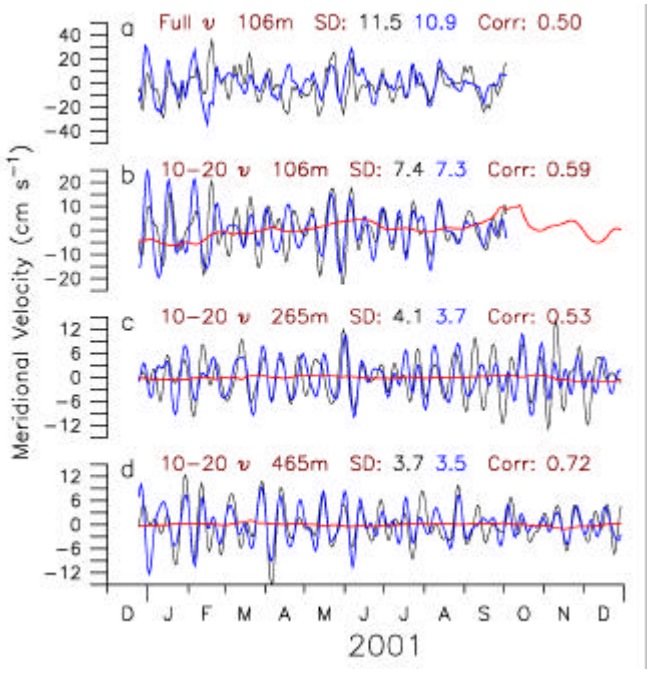

Fig. 3 . Comparison of observed and model *v* at 0° N, 93°E. (a) Observed (black) and model (blue) unfiltered *v* at uppermost instrument depth; (b,c,d) observed (black) and model (blue) 10-20 day filtered *v* at the three shallowest instrument depths; model *v* from the run with seasonal winds (red) at mean instrument depths (106m, 265m and 465m) is also shown. The current meter at 106m gave no data beyond October. The standard deviations and correlation coefficients of observed and model time series are mentioned above each panel.

4. THE BIWEEKLY MODE

The biweekly wave has westward and generally upward phase propagation (not shown). Westward phase speed is generally between 3.6 and 4.8 ms^{-1}, and zonal wavelength is between 4000km and 5500km. The vertical scale of the wave below the thermocline is large relative to the model vertical grid spacing, which is about 125m at a depth of 500m.

The horizontal structure of the 10-20 day variability of surface wind stress and ocean circulation is brought out with the help of composites based on filtered fields. Figure 4 shows composite structures in the east and west, based on 15 biweekly events from June to September 2000 and 2001.

Wind stress variability over the eastern EqIO consists of vortices of alternating sign centered on the equator (Figure 4a,b). Wind stress variability in the western EqIO is best characterized by alternating episodes of northward and southward meridional wind stress (t_y; Figure 4e,f). The composite biweekly mode in the eastern (Figure 4c,d) and western (Figure 4g,h) ocean at the seventh model level (~ 106m depth) has the structure of an MRG wave with half-wavelength of about 2000km. Both zonal wavelength and meridional trapping length appear to be somewhat larger in the east. The vertical velocity associated with the biweekly mode has amplitudes of a few metres per day. The *w* field is antisymmetric about the equator with maxima located at 2-3° latitude. The composite horizontal structure at 500m (not shown) has similar character. The composite structure in the latitude-depth plane (not shown) has deep upwelling/downwelling on either side of the equator, connected by cross-equatorial meridional flow.

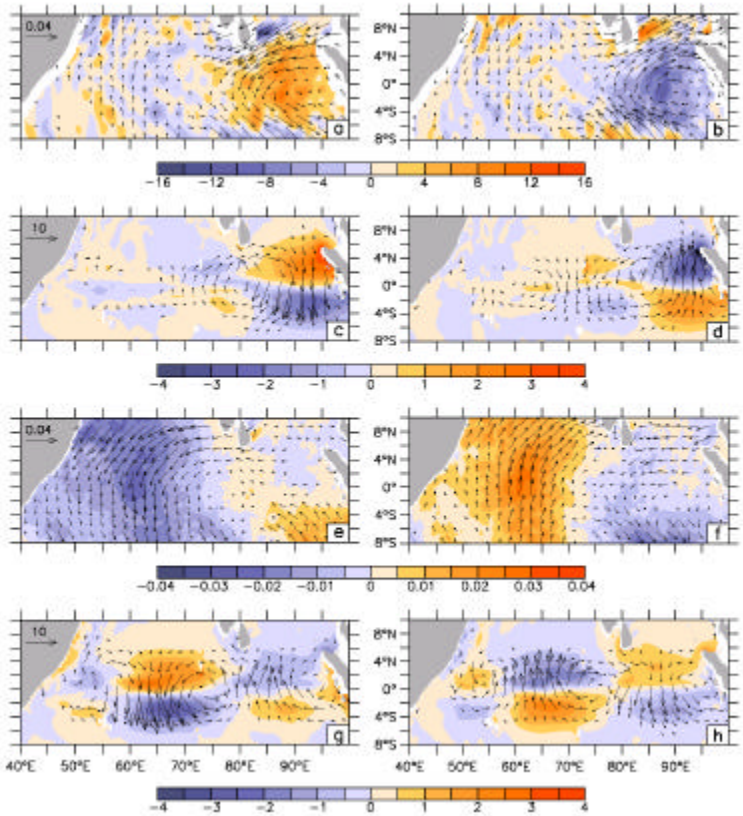

Fig. 4 Composite horizontal structure of biweekly variability in the east and west. (a,b) Wind stress curl (10^8 N m^{-3}; shaded) and wind stress vector (N m^{-2}) composites based on dates of maximum positive (left) and negative (right) curl averaged over 5°S-5°N, 85-95°E (e,f) t_y (N m- 2 ; shaded) and wind stress vector composites based on dates of maximum negative (left) and positive (right) t_y averaged over 5°S-5°N, 55-65°E; (c,d,g,h) composite vertical velocity (m day^{-1};shaded) and current vectors at 106m depth (cm s^{-1}), based on dates of maximum southward (left) and northward (right) meridional volume transport in the upper 100 metres across the equator during June to September of 2000 and 2001; the transport is computed over five degree segments in the (c,d) eastern EqIO, 90-95°E, and (g,h) western EqIO, 60-65°E.

5. CONCLUSIONS

The biweekly mode, whose structure and origin are studied here, explains aspects of previously observed variability in the equatorial Indian Ocean. It appears to be present throughout the year, with largest amplitudes in the eastern EqIO. We have shown that the biweekly mode is generated by intraseasonal variability of surface wind stress rather than dynamic instability of seasonal ocean currents. The biweekly upwelling documented in this study might have interesting implications. Eastward equatorial jets in the Indian Ocean in spring and fall, forced by westerly winds [6], lead to downwelling and a deep thermocline in the eastern Indian Ocean [7]. The appearance of sustained easterly winds in the EqIO during strong "dipole" episodes such as those of 1961, 1994 or 1997 can drive upwelling off the coast of Sumatra as well as at the equator [8], giving rise to high chlorophyll concentrations in the east [9]. We have presented evidence that upwelling in the EqIO is not confined to dipole events or to the eastern basin: Deep upwelling and downwelling associated with the biweekly mode is present throughout the year all along the EqIO. Since upwelling followed by mixing is an irreversible process, this mode is likely to influence the vertical distribution of temperature, nutrients and chlorophyll in the equatorial Indian Ocean.

ACKNOWLEDGMENTS

The moored current meter observations are funded by DOD. DS acknowledges support from DOD and the Department of Science and Technology, New Delhi. We thank B. N. Goswami for useful discussions at all stages of the work, and Dr. E. Desa, Director NIO, for support.

REFERENCES

[1] Murty *et al.* First results of Indian current meter moorings along the equator: Vertical current structure variability at equator, 93E during February-December 2000. *Proc. 6th Pan Ocean Remote Sensing Conference, PORSEC 2002*, Bali, Indonesia, 3-6 September 2002. 1, 25-28.

[2] McPhaden MJ: Variability in the central equatorial Indian Ocean Part I: Ocean dynamics. *J. Mar. Res*., 1982, **40**, 157-176.

[3] Schott F, Reppin J, Quadfasel D, Fischer J: Currents and transports in the Monsoon Current south of Sri Lanka. *J. Geophys. Res*., 1994, **99**, 25127-25141.

[4] Reppin J, Schott F, Fischer J, Quadfasel D: Equatorial currents and transports in the upper central Indian Ocean. *J.Geophys. Res*., 1999, **104**, 15495-15514.

[5] Pacanowski RC. ***MOM2 Version 2.0 (Beta): Documentation, user's guide and reference manual*** , GFDL Ocean Technical Report 3.2, Geophysical Fluid Dynamics Laboratory, Princeton NJ, 1996.

[6] Knox RA: On a long time series of measurements of Indian Ocean equatorial currents near Addu Atoll. *Deep Sea- Res.*, 1976, **23**, 211-221.

[7] Wyrtki K, An equatorial jet in the Indian Ocean, *Science*, 1973, **181**, 262-264.

[8] Murtugudde R, McCreary JP, Busalacchi AJ: Oceanic pro-cesses associated with anomalous events in the Indian Ocean with relevance to 1997-1998, *J. Geophys. Res.*, 2000, **105**, 3295-3306.

[9] Murtugudde R, Signorini SR, Christian JR, Busalacchi AJ, McClain CR, Picaut J: Ocean color variability of the tropical Indo-Pacific basin observed by SeaWiFS during 1997-1998, *J. Geophys. Res*., **104**, 1999,18351-18366.

Proceedings of the Tenth Asian Congress of Fluid Mechanics
17-21 May 2004, Peradeniya, Sri Lanka

NUMERICAL MODELING & A FIELD TEST OF GROUND PENETRATING RADAR FOR SOIL MOISTURE CONTENT ESTIMATION

L. W. Galagedara,
Department of Agricultural Engineering, University of Peradeniya, KY 20400, Sri Lanka

G. W. Parkin
Department of Land Resource Science, University of Guelph, Ontario, N1G 2W1, Canada

J.D. Redman and A.P. Annan
Sensors and Software Inc., Mississauga, Ontario, L4W 3R7, Canada

ABSTRACT: Numerical simulation of electromagnetic radiation was performed using GPRMAX2D to estimate the penetration depth of the ground penetrating radar (GPR) direct ground wave. Two modeling approaches were used with two different soil layers: i) dry soil over wet soil layer, ii) wet soil over dry soil layer. The depth to the wet layer was estimated by analyzing the two way travel time of the reflected event from the wet layer. In both models, the top layer thickness was gradually reduced and the simulation was performed using four different frequencies from 100 to 900 MHz. Simulation was carried out using the common mid point (CMP) survey type with antenna separations starting at 0 m. A very high correlation was found between the GPR direct ground wave influence depth and the radar wavelength, λ ($\lambda = V/f$), where V is the electromagnetic wave velocity and f is the frequency. No difference was found between the estimated depth to the wet layer using the reflected wave and the true depth of the model. Field experiments showed that the GPR ground wave could be used to estimate the spatial soil moisture variability at shallow depths when antenna offsets close to 1 m were used.

1. INTRODUCTION

Soil moisture content is one of the most important hydrological parameters in many field applications such as irrigation management, modeling contaminant transport to the ground water, erosion-runoff modeling etc. Estimating depth to the ground water table and its horizontal extent are essential in water resources development and management for essential water supplies such as irrigation water, drinking water or industrial waters. Current methods of soil moisture measurements and water table depth explorations are time consuming, destructive and the sampling volumes are restricted to small areas.

Ground penetrating radar (GPR), a high frequency electromagnetic method has been identified and tested in the recent past as an effective geophysical tool for field scale soil moisture and water table depth mapping over large areas. Mapping of water table depth and groundwater contamination distribution is limited by the high cost associated with conventional approaches; nondestructive and rapid electromagnetic methods could solve this problem. Ground penetrating radar has been used to estimate soil moisture and water table depth variation during pumping test analyses [5]. The GPR direct ground wave method was used for non-destructive estimate of soil moisture variability over different field scales [3,4,6,8,9,10]. The reflected GPR wave from the advancing wetting front during uniform irrigation was used to estimate the soil moisture content and wetting front depth variability with time [13].

Several authors have concluded experimentally that GPR direct ground wave penetration is restricted to the near surface, perhaps less than 0.2 m below the surface [3,4,6,8,10]. According to [4,6,8], the direct ground wave penetration depth is frequency dependent. As the GPR ground wave is an unguided electromagnetic wave, its penetration depth, hence the sample volume is not well documented. The main objectives of this paper are: i) to investigate the GPR ground wave penetration depth using a simple two layer electromagnetic radiation model with various frequencies, ii) to estimate the depth to the bottom wet layer which is at near saturation, and iii) to assess the GPR direct ground wave method in the field under two different land use types. To fulfill objectives i and ii, GPRMAX2D V1.5 [7] (Electromagnetic simulator for Ground Probing Radar) was used to solve Maxwell's equations using the Finite-Difference Time-

Domain (FDTD) approach. In this study, the thickness of the upper layer in the two-layer model is decreased until the velocity of the direct ground wave is influenced by the different dielectric constant assigned to the lower layer.

2. MODELING APPROACH: CONCEPTUAL TWO-LAYER MODEL

Conceptual two-layer soil models (dry soil over wet soil and wet soil over dry soil) for GPR direct ground wave penetration depth determinations are shown in Figure 1. Common mid point (CMP) surveys were conducted starting at 0 m antenna offset at the middle of the model domain with stepwise increasing antenna offsets at a constant increment. For each CMP survey, 20 traces were simulated. After each CMP survey, the overlying dry soil layer (Figure 1A) or wet soil layer (Figure 1B) thickness was reduced gradually and each time a new CMP survey was simulated. This process was continued until the upper layer thickness was zero and the model became a homogenous medium made up of the bottom layer. Each CMP survey was used to calculate the direct ground wave velocity using the inverse slope of the time-offset relationship of the direct ground wave [4,6,9,10]. Several model runs using 100, 200, 450 and 900 MHz frequencies were performed with different dielectric permittivities assigned to each layer (Fig. 1) and with all layers assigned an electrical conductivity of zero. Volumetric soil moisture contents (θ_v) were calculated first by converting the velocity, V into dielectric permittivity, K_r [$K_r = (c/V)^2$], where c is the speed of light (0.3 m/ns) and then converting the dielectric permittivity into soil moisture using the equation 1[12]:

$$\theta_v = -5.3\times10^{-2} + 2.92\times10^{-2} K_r - 5.5\times10^{-4} K_r^{\,2} + 4.3\times10^{-6} K_r^{\,3} \quad (1)$$

After modeling CMP surveys for each frequency with parameters given in Table 1, the dielectric permittivity of the dry layer was changed and the simulation was repeated to investigate the effect of soil moisture content of the dry soil layer on ground wave penetration depth.

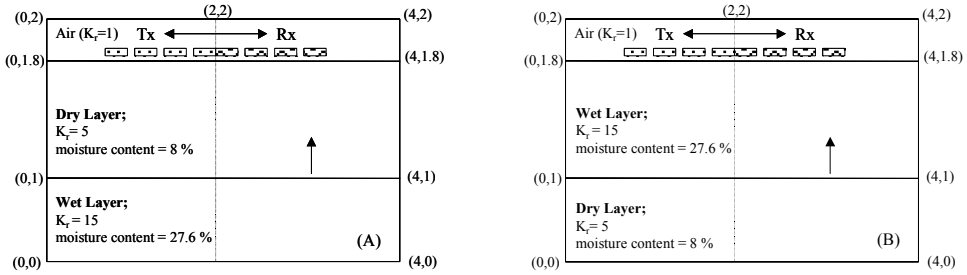

Fig. 1: Schematic diagram of conceptual two-layer model for GPR direct ground wave modeling (A: dry soil over wet soil model, B: wet soil over dry layer model). K_r is relative dielectric permittivity. Tx: Transmitter antenna, Rx: Receiver antenna. Numbers in parenthesis show spatial coordinates starting from bottom left corner of the domain.

Table 1: Parameters used in the two-layer model of GPR electromagnetic radiation with different frequencies.

Model Description	100 MHz	200 MHz	450 MHz	900 MHz
Model Size (m^2)	3 x 6	2 x 4	2 x 4	2 x 4
Time Window (ns)	60	30	30	30
Cell Size (Δx, and Δy) (m)	0.01	0.005	0.005	0.005
Antenna Step Size (m)	0.20	0.10	0.10	0.05

3. RESULTS AND DISCUSSIONS

3.1 GPR Wave Fronts in a Two-Layer Soil Model (dry soil over wet soil layer model)

Numerous wave fronts can be identified when a point source wave generator is used [1,8,9]. Simulated wave fronts from a point source after 6 ns for a two-layer earth model (dry soil over wet soil layer model)

are shown in Figure 2. Wave A is the direct airwave (spherical) and A^1 is the reflected "spherical" wave from the subsurface interface emitted into air. The ground wave (also a spherical wave) in the second layer is identified as B. The direct ground wave (GW) is a combination of the evanescent wave in air (b) and spherical ground wave (C) in first layer. The spherical ground wave reflected from the subsurface interface is identified as D.

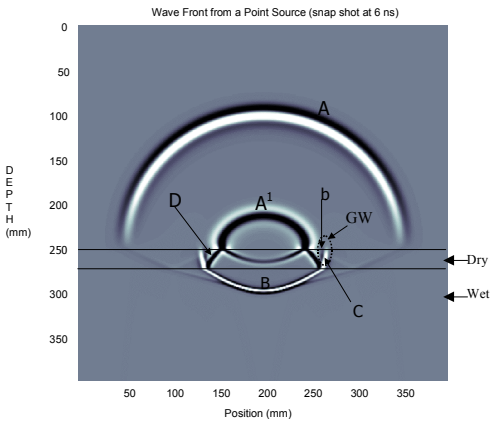

Fig. 2: Simulated wave fronts from a point source on the soil surface for the dry over wet soil layer model.

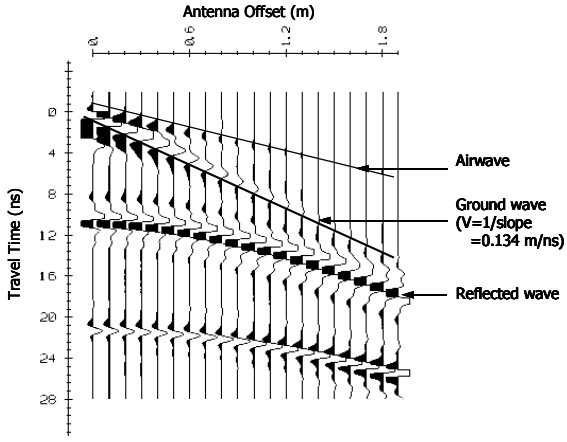

Fig. 3: Raw data obtained from a simulated CMP survey with 450 MHz frequency for dry over wet soil layer model.

3.2 Synthetic Data Analysis: CMP Survey for the Dry over Wet Soil Layer Model

Figure 3 shows CMP data gathered during dry over wet soil layer model run with 450 MHz frequency, which shows direct airwave, direct ground wave and the reflected wave from the dry/wet layer boundary. The velocity of the direct ground wave was calculated from the inverse slope of the regression line as shown and was found to be 0.134 m/ns (correct for $K_r = 5$) in Figure 3 for the dry over wet layer model.

3.3 Ground Wave Velocity Analyses and Moisture Content Estimation

GPR ground wave penetration depth modeling was performed using simple dry over wet and wet over dry soil layer models using GPRMAX2D. Figure 4 shows the soil moisture content dependence on depth to the wet layer for the dry soil over wet soil case (Fig. 4A) and to the dry layer for the wet soil over dry soil case (Fig. 4B) for GPR centre frequencies of 200 and 450 MHz. As seen in both Figures, when the upper layer thickness decreases gradually, estimated moisture content starts to increase as influenced by the bottom wet layer (Fig. 4A) or starts to decrease as influenced by the bottom dry layer (Fig. 4B). The depth of influence is found from the depth to the wet layer or depth to the dry layer as moisture content starts to change as the upper layer thickness decreases. It is clear in Figure 4 that the ground wave influence depth varies with frequency as the moisture content starts to change at different depths to the wet layer (Fig. 4A) or dry layer (Fig. 4B). The greatest depth of influence was found for the lowest frequency while the smallest depth of influence was found for the highest frequency.

It was found during the different model runs that when the upper soil layer thickness decreases, eventually the direct ground wave travels entirely through the bottom soil layer below instead of the very thin dry or wet soil layer near the surface. Evidence to support this hypothesis is that the model estimated moisture content becomes equal to the moisture content in the wet soil layer as the depth to the wet soil layer decreases (Fig. 4A) or equal to the moisture content in the dry soil layer as the depth to the dry soil layer decreases (Fig. 4B). This behavior has been documented elsewhere [3], that the layer thickness was more dominant for the ground wave influence than the moisture content of that layer. Also, note that the thickness of the upper soil layer when the ground wave starts to travel through the bottom soil layer

below is also dependent on the GPR frequency. Depths of influence of the GPR direct ground wave were lower for all frequencies in the wet soil over dry soil layer model (similar to an irrigation condition) compared to the dry soil over wet soil layer model (similar to a drainage condition). Estimated ground wave influence depths for all frequencies simulated for two different modeling approaches are given in Table 2. Linear (Eq. (2)) and power (Eq. (3)) relationships were found from this modeling approach between the ground wave influence depth (D) and the wavelength (λ) of the ground wave with very high correlation.

For all models there was a range of upper layer thicknesses for which the ground wave could not be clearly identified and picked, due to the interference between the ground wave and the reflected wave from the bottom of the upper layer. Practically, in field applications, this would only likely to occur if a sharp boundary exists such as a wetting front during an irrigation event. This problem can be avoided under normal field conditions since sharp changes in moisture content stratification rarely exists. From further simulations performed for very low contrasting permittivity values between two layers, continuous data could be obtained.

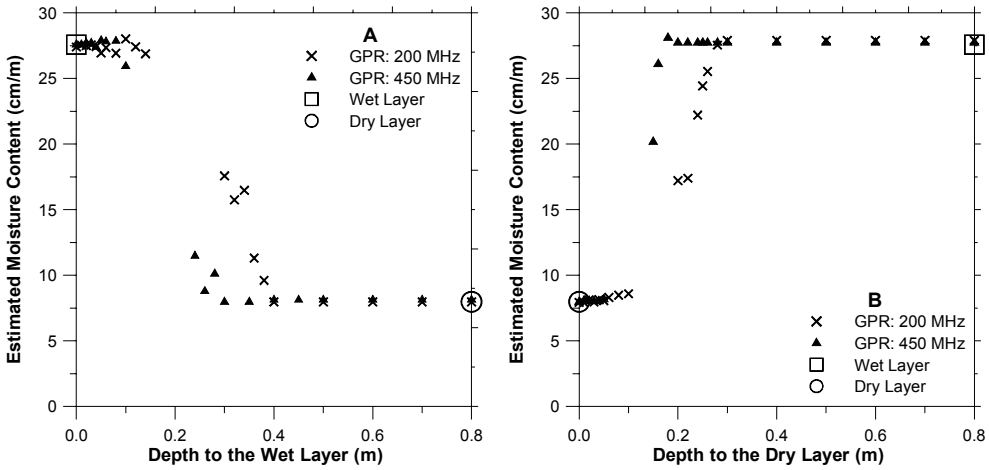

Fig. 4: Variation of the estimated soil moisture (cm/m) for two different frequencies obtained from dry soil over wet soil model (A) and wet soil over dry soil layer model (B).

Table 2: Modeled GPR direct ground wave penetration depth and maximum influence depth for different frequencies.

Model Description	100 MHz	200 MHz	450 MHz	900 MHz
1. Dry Over Wet Layer Model				
Ground Wave Influence Depth (m)	0.80~1.00	0.35~0.45	0.25~0.35	0.12~0.16
Ground Wave Traveling Depth (m)	0.25	0.14	0.06	0.03
2. Wet Over Dry Layer Model				
Ground Wave Influence Depth (m)	0.55~0.65	0.25~0.35	0.14~0.18	≤0.10
Ground Wave Traveling Depth (m)	0.20	0.10~0.12	0.05	0.02

Linear: $D = \lambda * 0.6292 + 0.0579$ ($R^2 = 0.975$) (2)

Power: $D = \lambda^{0.7941} * 0.6729$ ($R^2 = 0.978$) (3)

3.4 Depth to the Reflector (wet layer)

Depth, h to the reflector (i.e. the wet layer in this case) can be estimated from CMP surveys by analyzing the two-way travel time to the reflection event at different antenna offsets, as commonly used

in seismic reflection theory. As seen in Figure 3, the reflected event is a parabolic curve and plotting time squared, t^2, vs offset squared, x^2, gives the following linear relationship:

$$t^2 = \frac{1}{V^2} \times x^2 + \frac{4 \times h^2}{V^2} \tag{4}$$

where the average velocity V in the soil profile above the reflector can be estimated using the slope m [$V = (1/m)^{0.5}$]. The intercept C of the x^2 vs t^2 relationship for the reflected event can be used to estimate the depth h to the reflector [$h = C^{0.5} * V/2$]. As several authors have documented, this method can be used to estimate the depth to the water table. However, [2,11] showed that water table depth estimation is some times difficult due to weak reflection events when there is a gradational interface between the unsaturated zone and the water table due to capillary rise. Estimation of the depth to the water table thus, could be difficult especially in fine textured soils with high GPR frequencies. Figure 5 shows the comparison of the estimated depth to the wet layer with the true depth for the dry soil over wet soil layer model simulated using two different frequencies. In this modeling approach, very accurate depths to the wet layer could be estimated since there was a sharp boundary between the dry layer above and the wet bottom layer.

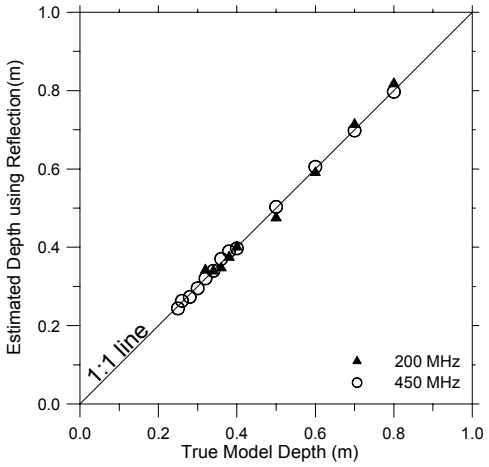

Fig. 5: Comparison of estimated depth to the reflector with the true depth of the model.

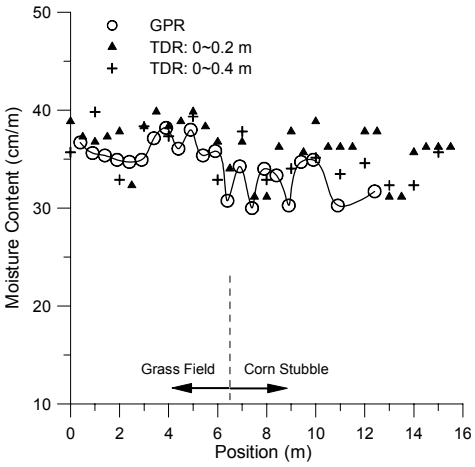

Fig. 6: Soil moisture variability estimated with GPR and TDR at two depths on two different land use types.

3.5 Field Application of the GPR Ground Wave Method

A field experiment was conducted at the Elora Research Station of the University of Guelph, Ontario, Canada to assess GPR water content measurements on a harvested cornfield and a grass field as two distinct vegetative covers. Soil type is silt loam and the subsurface is very stony below 0.6 m. The selected survey line was 16.0 m long, of which 6.5 m was within the grass field and the remaining 9.5 m was within the cornfield. The corn grain had been harvested with most of the crop residue left on the soil surface. Surface GPR survey was conducted along a line from the grass to the cornfield using high frequency (450 MHz) radar antenna. Multiple offset surveys were conducted with transmitter-receiver offsets ranging from 0.4 m to 0.8 m with 0.1 m increments. GPR estimated soil moisture contents were assessed using TDR measured values at two different depths (0-0.2 and 0-0.4 m). Figure 6 shows GPR estimated moisture contents using 0.8 m antenna offset compared with TDR measured moisture contents at two different depths. GPR method agrees fairly well with the TDR method moisture contents at both depths, but is closer to the 0-0.4 m depth. It was found that the GPR estimated moisture contents using 0.8 antenna offset is less variable than shorter offset distances and generally followed the same pattern as the

TDR measured values. The GPR method with shorter antenna offsets such as 0.4 and 0.5 showed higher variability than larger offsets compared to the TDR method, especially on the cornfield. This high moisture content variability could be due to: i) the spatial variability in cornfield and ii) poor ground contact (ground coupling) of GPR antennas on corn stubble, whereas larger offsets reduce this error by averaging over larger areas.

4. CONCLUSIONS

4.1 Numerical modeling shows that the GPR direct ground wave influence depth varies with antenna frequency and soil moisture content. Very strong linear and power relationships were found between the GPR direct ground wave influence depth and the wavelength.

4.2 Depth to the reflector (wet layer) estimated by analyzing the reflected event compares well with the true depth in the model. Application to ground water table depth mappings could be problematic when a sharp boundary does not exist due to capillary rise, especially in fine textured soils.

4.3 A field study shows that the GPR direct ground wave method can be used to estimate the spatial variability of soil moisture when antenna offsets near 1 m are used and these measurements agreed fairly well with TDR measured soil moisture content values.

ACKNOWLEDGEMENTS

Authors wish to acknowledge Ontario Ministry of Agriculture and Food (OMAF) and Natural Science and Engineering Research Council of Canada (NSERC) for providing the financial support. Valuable comments and suggestions given by Dr Anthony Endres of University of Waterloo, Canada are highly appreciated. Kevin Kingdon of Sensors and Software Inc. gave an excellent support in GPR simulation.

REFERENCES

[1] Annan AP: Radio interferometry depth soundings: part I – theoretical discussion. *Geophysics*. 1973, **38** (3), 557-580.

[2] Annan AP, Cosway SW, Redman JD. Water table detection with ground penetrating radar. Expanded Abstracts SEG 61st Annual Meeting, Houston, Texas, November, 1991, 494-496.

[3] Chanzy A, Tarussov A, Judge A, Bonn F: Soil water content determination using a digital ground-penetrating radar. *Soil Sci. Soc. Am. J.* 1996, **60,** 1318-1326.

[4] Du S and Rummel P. Reconnaissance studies of moisture in the subsurface with GPR. In *Proceedings of the Fifth International Conference on Ground Penetrating Radar*, Waterloo Center for Groundwater Research, Waterloo, Ontario, Canada, June 12-16 1994, Vol. 3 (3), 1241-1248.

[5] Endres AL, Clement WP, Rudolph DL: Ground penetrating radar imaging of an aquifer during a pumping test. *Groundwater*. 2000, **38** (4), 566-576.

[6] Galagedara LW, Parkin GW, Redman JD: An analysis of the GPR direct ground wave method for soil water content measurement. *Hydrol. Process*. 2003, **17** (in press).

[7] Giannopolous A: Electromagnetic simulator for ground probing radar: GPRMAX2D V 1.5 User's manual. 2002, University of Edinburgh, Scotland.

[8] Hubbard S, Grote K, Rubin Y: Mapping the volumetric soil water content of a California vineyard using high-frequency GPR ground wave data. *The leading edge.* 2002 June, 552-559.

[9] Huisman JA: Measuring soil water content with time domain reflectometry and ground penetrating radar: accuracy, reproducibility and feasibility. PhD-Thesis. 2002, Universiteit van Amsterdam, The Netherlands.

[10] Huisman JA, Sperl C, Bouten W, Verstraten JM: Soil water content measurements at different scales: Accuracy of time domain reflectometry and ground penetrating radar. *J Hydrol.* 2001, **245,** 48-58.

[11] Redman JD, DeRuck SM, Annan AP. Detection of LNAPL pools with GPR: theoretical modeling and surveys of a controlled spills. In *Proceedings of the Fifth International Conference on Ground Penetrating Radar*, Waterloo Center for Groundwater Research, Waterloo, Ontario, Canada, June 12-16 1994, Vol. 3 (3), 1283-1294.

[12] Topp GC, Davis JL, Annan AP: Electromagnetic determination of soil water content: Measurements in coaxial transmission lines. *Water Resour. Res.* 1980, **16** (3), 574-582.

[13] Vellidis G, Smith MC, Thomas DL, Asmussen LE: Detecting wetting front movement in a sandy soil with ground penetrating radar. *Trans. Am. Soc. of Agric. Engi.* 1990, **33** (6), 1867-1873.

Proceedings of the Tenth Asian Congress of Fluid Mechanics
17-21 May 2004, Peradeniya, Sri Lanka

INITIAL STAGE OF UPSLOPE FLOW DEVELOPMENT ON INCLINED SURFACES

M. Princevac and H. J. S. Fernando
Department of Mechanical and Aerospace Engineering, Arizona State University, Tempe, AZ 85287, U.S.A.

ABSTRACT: Turbulent convection over a heated horizontal plane is characterized by updrafts and downdrafts with no net mean motion, but a mean upslope (or anabatic) flow will be generated if the plane is even slightly inclined. Theoretical and laboratory investigations of the upslope flow phenomena have been conducted, with the aim of understanding the mechanisms responsible for the generation of upslope flow. It is argued that the tendency of the heated fluid to follow the slope is inversely proportional to the Prandtl number of fluid. Laboratory experiments performed by observing the motion of different water-glycerin solutions over heated plate with a specified inclination angle confirmed this proportionality. This finding can explain the existence of well-developed upslope flows above very gentle slopes in the areas of complex terrain.

1. INTRODUCTION

World's population centers are often located in topography replete with mountains, valleys, escarpments and basins (also known as complex terrain). These areas are prone to air circulation (winds) driven by local diurnal variation of solar heating, i.e. cooling of the topography at night and heating during the day. Of major significance are the slope and valley wind systems, wherein downslope and down-valley winds occurring at night and upslope and up-valley winds flowing during the day. The formation mechanisms and dynamics of downslope and down-valley winds have been well studied using laboratory and numerical modeling as well as field studies ([16]; [2]). Upslope and up-valley flows, however, have attracted only little attention of the research community, perhaps because of their profound practical importance in air pollution dispersion has not been fully realized until recently. The handful of reported studies of up-slope/valley flows were mainly confined to observational and numerical studies ([3]; [4]; [11]; [12]). Recent field studies show that upslope flows can effectively transport pollutants and their precursors from one area to another, tens of kilometers within a day, causing one area to bear the brunt of pollution of another ([6]; [7]). This effect is exacerbated by the fact that, during such transport, some of the pollutants, colluding with turbulent mixing and intense sunlight, can generate additional hazardous pollutants such as ozone.

Whiteman ([16]; [17]) explained the genesis of up-valley flows by considering a simple topographic configuration of a valley located adjacent to a plane. Whereas solar energy per unit area arriving at the brim of the valley and at the same height of a plain is the same, beneath the same area, on average, the valley contains a lesser air mass compared to that of the plain due to the sloping topography. Therefore, the daytime temperature of a valley tends to be higher than that of a contiguous plane, which causes a hydrostatic pressure differential to build up and drive the upslope flow. This effect is quantified using the so-called "topographic factor." Conversely, to our knowledge, there are no explicit physical explanations to describe the formation of upslope flows nor have there been reported criteria to ascertain whether thermal convection over a given slope leads to an upslope flow, although it is known that plumes located near sloping boundaries tend to flow along the slope rather than rising vertically [10].

In this paper, we advance an explanation for the formation of slope flows on an inclined plane subjected to surface heating. As proposed by Howard [8] and demonstrated by laboratory experiments ([14]; [11]), at high Rayleigh numbers, turbulent thermal convection on a horizontal plane is initiated via thermals rising vertically due to the breakdown of thermal boundary layer that develops on the heated surface. When the plane is inclined, however, a horizontal pressure gradient can be developed across rising thermals (signifying the Coanda effect), causing them to cling on to the surface, thus deflecting the thermals upslope. By considering two competing tendencies, one responsible for the vertical rise of the thermals and the other favoring their clenching to the sloping plain, a criterion is advanced in Section 2 to predict the conditions under which the upslope (anabatic) flow prevails over rising thermals. The interest is on high heat-flux (or turbulent convection) conditions with applications to atmospheric convection in complex terrain. Laboratory experiments conducted to verify theoretical predictions are described in Section 3. The results of the experiments are given in Section 4.

2. THEORETICAL ANALYSIS

In the case of flow development at the inclined plate there are two major forces: buoyancy force that drives flow vertically up and pressure force which drive the flow horizontally towards the slope (see Figure 1). For analyzing competing tendencies of vertical rising vs. horizontal motions of the thermal blob, a model based on the phenomenological description of turbulent thermal convection by Howard [8], wherein convection on a flat surface is initiated and maintained by the development and breakdown of a molecular boundary layer near the surface, is presented. The thickness δ of this boundary layer grows with time t according to $\delta \sim c_1(\kappa t)^{1/2}$ and breaks down to form thermals (heated fluid blobs) after reaching a critical Rayleigh number

$$Ra_c = \frac{g\alpha\Delta T\delta_c^3}{\nu\kappa} \approx 10^3, \tag{1}$$

where κ is the thermal diffusivity, g the gravitational acceleration, α the thermal expansion coefficient, δ_c the limiting value of δ at the breakdown, and ν the kinematic viscosity. The density of the fluid is expressed using the equation of state $\rho = \rho_0(1-\alpha\Delta T)$, where ΔT is the temperature difference between the thermal and the (reference) background fluid of density ρ_0. Thereafter, a new boundary layer is formed and the sequence of growth/breakdown events continues, intermittently releasing buoyant thermals that feed into convection. Sparrow *et al*. [14] and Adrian *et al*. [1], among others, have provided experimental support for this model, particularly for the initial development phase of turbulent convection.

Initial motion inside the boundary layer is determined by the balance of viscous and buoyancy force:

$$\nu\frac{\overline{U}_b}{\delta^2} \sim \alpha g\Delta T\beta, \tag{2}$$

where $\overline{U}_b$ is the averaged flow velocity. The heat balance in the boundary layer takes the form

$$q_0 t \sim g\alpha\Delta T\delta, \tag{3}$$

where q_0 is the buoyancy flux at the bottom boundary, $q_0 = \alpha g Q/\rho_0 c_p$, Q the bottom heat flux and c_p is the specific heat (see [9]). Now $\overline{U}_b$ can be expressed as

$$\overline{U}_b \sim \beta\frac{q_0 t\delta}{\nu}. \tag{4}$$

The time for which the blob will travel along the slope, before it separates from it, can be estimated from (1) and (3) as

$$t_c \sim \left(\frac{Ra_c\nu}{q_0}\right)^{1/2}. \tag{5}$$

As mentioned before, the layer depth, in this initial stage grows according to $\delta \sim c_1(\kappa t)^{1/2}$. The length of travel before the detachment occurs can be estimated as

$$L = \int_0^{t_c}\overline{U}_b dt \sim \tfrac{2}{5}c_1\beta\frac{Ra_c^{5/4}}{\mathrm{Pr}^{1/2}}\left(\frac{\nu^3}{q_0}\right)^{1/4}, \tag{6}$$

which is on the order of several centimeters. These motion sets the wall conditions for the upslope flows. The major forcing for the maintenance for the upslope flow, however, comes soon after the blob detachment, where its rise is deflected by the horizontal pressure gradient forces.

Buoyancy force in a detached thermal blob leads to its vertical rise. A horizontal pressure gradient also develops, however across the entire blob, thus generating an additional horizontal force that deflects the thermal along the slope (see Figure 1). These two forces can be expressed as

$$B \sim (\rho_0 - \rho)g\delta^3 = \rho_0\alpha\Delta T\delta^3 g, \tag{7}$$

and

$$P \sim \Delta p\delta^2 \sim \rho_0(u_1^2 - u_2^2)\delta^2, \tag{8}$$

where u_1 and u_2 are the entrainment velocities from the sides of the thermal. The pressure gradient can be estimated by assuming that the thermals entrain the same total volume of fluid from all directions, and hence the characteristic entrainment velocity of the down-slope facing side of the thermal (u_2) is lower than the up-slope facing side u_1, viz.

$$U\delta^2 \sim u_1\delta^2(1-\beta) = u_2\delta^2(1+\beta), \tag{9}$$

where U is the characteristic velocity of the entrainment flow based on total entrainment due to the rise of the thermal. The horizontal pressure differential, thus, can be scaled as

$$\Delta p \sim \rho_0 U^2 \beta. \tag{10}$$

which when substituted back in (8) gives

$$P \sim \Delta p \delta^2 \sim \rho_0 U^2 \beta \delta^2. \tag{11}$$

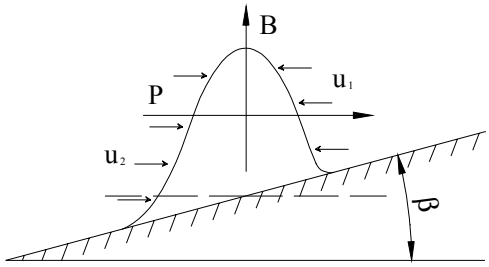

Fig. 1: Thermal blob at the moment of detachment from inclined surface subjected to heating. Note the vertical buoyancy force and horizontal pressure force.

The characteristic velocity of the entrainment flow can be scaled as $U \sim \delta_c / t_c$.

Using (3) and (1) δ_c can be expressed as $\delta_c = \left(c_1^2 Ra_c\right)^{1/4}\left(\kappa^2 \nu / q_0\right)^{1/4}$ and U as $U \sim \left(c_1^6 / Ra_c\right)^{1/4}\left(\kappa^2 q_o / \nu\right)^{1/4}$.

Now using (1) and (7), the buoyancy force can be expressed as

$$B \sim \rho_0 Ra_c \kappa \nu, \tag{12}$$

and similarly from (11) pressure force can be expressed as

$$P \sim c_1^4 \rho_0 \beta \kappa^2. \tag{13}$$

It is interesting to check the ratio of these two forces combining (12) and (13) as

$$\frac{B}{P} \sim \left(\frac{Ra_c}{c_1^4}\right)\frac{P_r}{\beta}. \tag{14}$$

Note that, for smaller angles the buoyancy force dominates and after detaching the blob will rise vertically. An interesting result is that this ratio is proportional to the Prandtl number of fluid. This proportionality means that for a very high *Pr* the blobs will not follow the slope but will rise like in the case of very small slope angles β. This ratio determines whether or not the upslope flow dominates vertical rising.

3. EXPERIMENTAL SETUP

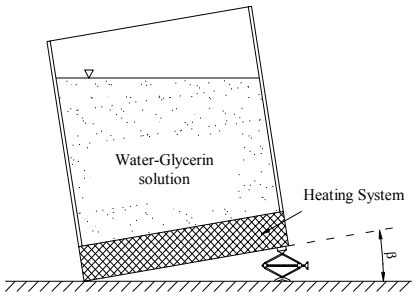

Fig. 2: A schematic of the experimental apparatus.

The experiments were carried out in a tank of cross section 60 x 60 (cm) and depth 70 cm, constructed with Plexiglas sidewalls (1.25 cm thick) and an aluminum bottom (1 cm thick); see Figure 2. The heating system lay beneath the aluminum plate and was comprised of a custom designed heating pad insulated from below by two layers of 1.25 cm marsonite sheet, a single layer of 2.5 cm thick foam insulation and a 0.8 cm thick aluminum base plate. Insulation from the sides was provided by 2.5 cm foam sheets. A removable window in the sidewall insulation allowed optical access to visualize the flow. The heating pad was custom designed by Watlow Inc. and consisted of an array of closely spaced heating wires embedded in a conducting seating (base) material, the maximum total heat output being 1 kW/m^2. The heat flux was regulated using a rheostat. The slope angle of the bottom heating plate was realized by uniformly elevating one side of the tank using a precision adjustable jack. The beam of a small laser diode attached to a tank wall, parallel to the slope, was projected on to a screen placed 2 m from the tank, and the position of its image was used to calculate the inclination of the heating plate. The accuracy and resolution of inclination measurements were 0.25 and 0.125 degrees, respectively. In the experimental planning, the apparatus was tested to ensure uniformity of temperature distribution along the slope. (It should be noted that an apparatus designed with a longer length of 2 m and heating provided by a heat exchanger had to be abandoned due to failure of realizing temperature uniformity along the slope). The rheostat was calibrated by measuring the temperature rise of a 15 cm layer of water in the tank over a time period 30 min, in the absence of the slope. Here the heat input was calculated considering the energy balance of the water layer and losses (which were estimated using the technique used by Voropayev and Fernando [15], to be less than $\pm$ 4%). These measurements agreed within $\pm$ 6% with independent flux measurements made using a heat flux meter.

Glycerin-water mixtures were used as a working fluid, allowing a wide range of Prandtl Numbers. Suspended particles of different densities and fluorescent dye were used to visualize the flow. Once the tank was at the desired inclination angle, enough time was allowed for the fluid to settle, insuring no residual motion, and then the bottom heating was initiated. A CCD camera and a SVHS/VCR recorded the motion field in the tank. The particle paths so recorded were digitized and analyzed using the DigImage software package (see [5]). The heat input during experiments was kept at a maximum of 1000 W/m^2 to ensure turbulent motion.

The purpose of the experiments was to investigate the formation and development of the upslope flow. For the purpose of quantifying results, the critical angle (β_c) was introduced. Critical angle is a limiting value of β below which upslope flow is not discernible, i.e. vertical rising of thermals dominates the flow.

For each mixture, an initial experiment was performed using a slope angle where well-developed upslope motion existed. Experiments were repeated with a slope decrement of 0.25°, until the upslope flow was no longer dominant over vertical rising. Several more experiments were conducted with sub-critical and super-critical slopes to ensure the accuracy of β_c. The heat input during selected experiments were also determined *a posteriori* by measuring the temperature rise and heat losses, and found to agree with those obtained during the rheostat calibration within ±5%. In flow visualization experiments with dye, homogeneous salt water of density 1.035 g/cm was used; these experiments delineated the mechanisms of the blob growth. Both the particles and the dye were illuminated using a 1 cm thick light sheet entering through a slit from the top opening of the tank. Particle paths recorded were later evaluated to determine the critical angle of the fluid.

4. EXPERIMENTAL RESULTS

A large number of experiments were conducted covering the Prandtl Number range from 6 (pure water) to 9500 (pure glycerin), and β_c for each case was determined. The influence of the temperature change to the Prandtl Number of the glycerin-water solution was estimated using the regression analysis results given by Shankar and Kumar [13]. Errors resulting from the temperature dependence of the Prandtl Number were added to the results (horizontal error bars). As shown, such errors cannot be neglected at high Prandtl Numbers (Pr>150). In addition, errors due to the angle measurement resolution were considered (vertical error bars). The results of β_c as a function of Pr is shown in Figure 3. The relation between the two quantities are not straight forward, and can be interpreted as belonging to three regimes. The best fit curves for the data are also shown in Figure 3. Although there is an increase of β_c with Pr, there appears to be no linear relationship over a wide parameter range.A question arises with regard to the evolution of a thermal (or a heated blob) on the inclined plate: Does the vertical growth follow the upslope motion or vice versa? This question is related to the previously posed question on the time scales required for the two competing tendencies to attain their full dynamical balances. The experiments showed that from the very beginning of its formation the blob is following the slope. This can be attributed to the transient period needed for the heat flux to reach the value for driving the turbulent flow. During this short period flow in a thin layer near the plate will be laminar, and follows the slope according to (2). The blob is advected by this laminar upslope flow while growing, and

finally detaches from the heated surface, contributing to the turbulent upslope flow. Figure 4 shows the initial development of the thin boundary layer that slides along the slope, the development of the blobs from this layer, its internal breakdown and detachment as a turbulent blob that carries buoyancy from the heated plate.

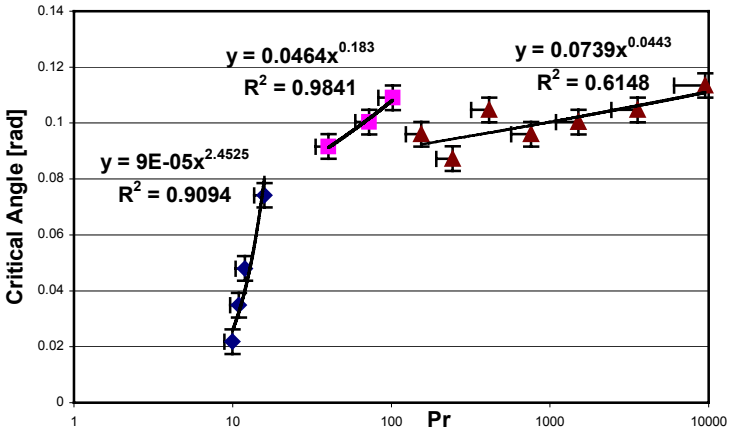

Fig 3: Critical angle (β_c) dependence on the Prandtl Number (*Pr*). The regression lines between the critical angle and *Pr* are shown for different regimes.

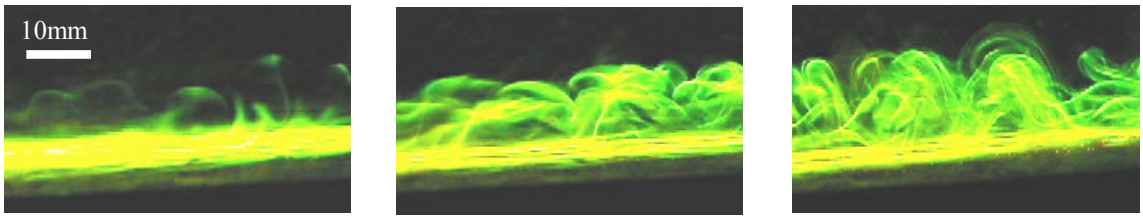

Fig. 4: The formation of thermals on a sloped plane (β=3°, Q=1000 W/m^2). Pictures taken 2 seconds apart.

ACKNOWLEGMENTS

This research was supported by the Environmental Meteorology Program of the Department of Energy (Grant # DE-FG03-99ER62846). The authors wish to acknowledge Mr. Gerardo Brigido for his help with laboratory experiments.

REFERENCES

[1] Adrian, R. J., Ferreira, R. T. D. S. and Boberg, T.: Turbulent thermal convection in wide horizontal fluid layers. *Exp. Fluids,* 1986, **4**, 121-141.

[2] Baines, P. G.: Mixing in flows down gentle slopes into stratified environments. *J. Fluid Mech.* , 2002, **471,** 315-337.

[3] Banta, R. M.: Daytime Boundary Layer Evolution over Mountainous Terrian. Part I: Observations of the Dry Circulations. *Amer. Metero. Soc.,* 1984, **112**(**2**), 340-356.

[4] Banta, R. M.: Daytime Boundary Layer Evolution over Mountainous Terrian. Part II: Numerical Studies of Upslope Flow Duration. *Amer. Metero. Soc.,* 1986, ***114(6)*** 1112-1130.

[5] Dalziel, S. B.: Rayleigh-Taylor Instability: experiments with image analysis. *Dyn. atmos Ocean.,* 1993, **20**, 127-153.

[6] Ellis, A. W., Hildebrandt, M. L., Thomas, W. M. and Fernando, H.J.S.: Analysis of the climatic mechanisms contributing to the summertime transport of lower atmospheric ozone across metropolitan Phoenix, Arizona, USA, *Climate Research*, 2000, **(15)**, 13-31.

[7] Fernando, H. J. S., Lee, S. M., Anderson, J., Princevac, M., Pardyjak, E., and Grossman Clarke, S.: Urban Fluid Mechanics: Air circulation and contaminant dispersion in cities, *Env. Fluid Mech.,* 2001, **1**, 107-164.

[8] Howard, L. N.: Convection at high Rayleigh number. In *Applied Mechanics*, *Proc. 11th Congr. of Appl. Mech., Munich* (ed. H. Görtler), 1966, 1109-1115. Springer.
[9] Hunt, J.C.R.: Turbulent structure in thermal convection and shear free boundary layers. *J. Fluid Mech*., 1984, **138**, 161-184.
[10] Hunt, J.C.R.: Industrial and Environmental Fluid Mechanics. *Annual Review of Fluid Mechanics*, 1991, **23**, 1-41.
[11] Kondo, J., Kuwagata, T. and Haginoya, S.: Heat budget analysis of nocturnal cooling and daytime heating in a basin. *J. Atmos. Sci.,*1989, **46(19),** 2917-2933.
[12] Kuwagata, T. and Kimura, F.: Daytime Boundary Layer Evolution in a Deep Valley. Part II: Numerical Simulation of the Cross Valley Circulation. *Amer. Meteorological Soc.*, 1997, **36,** 883-895.
[13] Shankar, P.N., and Kumar, M.: Experimental determination of the kinematic viscosity of glycerol-water mixtures. *Proc. R. Soc. London A*, 1994, **444**, 573-581.
[14] Sparrow, E. M., Husar, R. B. and Goldstein, R. J.: Observations and other characteristics of thermal. *J. Fluid Mech*., 1970, **41**, 793.
[15] Voropayev, S. I., and Fernando, H. J. S.: Evolution of two-layer thermohaline systems under surface cooling. *J. Fluid Mech.*, 1999, **380**, 117-140.
[16] Whiteman, C. D.: "Observations of thermally developed wind systems in mountainous terrain." Chapter 2 in Atmospheric Processes Over Complex Terrain, (W. Blumen, Ed.), *Meteor. Monogr*., 1990, **23** (no. 45), Amer. Meteor. Soc., Boston, Massachusetts, 5-42.
[17] Whiteman, C. D.: Mountain meteorology: fundamentals and applications. Oxford University Press, 2000, 355 pp.

Proceedings of the Tenth Asian Congress of Fluid Mechanics
17-21 May 2004, Peradeniya, Sri Lanka

A PHYSICAL MODEL FOR THE LAYERED STRUCTURE OF A DENSITY DRIVEN FLOW OVER A SLOPE

A. A. Bidokhti and M. Noroozi
Institute of Geophysics, Tehran University, Tehran PO Box 14155-6466, Iran.
bidokhti@ut.ac.ir

ABSTRACT: Down slope valley winds in a stratified environments, as the one observed typically in the northern Tehran (in sodar observations of Geophysics station, Tehran) show layered structure in their vertical profiles of the velocity. Here we present a physical model to show that the vertical modal structure of low frequency internal waves may generate these layers.

1. INTRODUCTION

Slope flows are the result of horizontal pressure gradients due to the thermal forcing on topographic surfaces. Upslope (anabatic) flows occur during the day, because of uneven heating of the slope and valley. Since the air mass within the valley is smaller than that of near the slope, the temperature within the valley is higher [1], so mass continuity requires closed circulating motion. Down slope flow valley winds happen at night as the result of radiation cooling of the surface. For typical length scales these currents occur with the slopes more than 10 deg. and their span ranges of a few km to more than 100 km [2].

Slope currents tend to flow toward the direction of maximum buoyancy forces, that is toward the region of maximum slopes [3]. Transition time between katabatic and anabatic winds occur after one or two hours after sunrise and sunset. Meteorologists are interested in studying these periods of time since winds are very weak in that time (<2 m/s), there is convergence/divergence and mixing, so they can dilute pollution in rush hour traffic in that periods [3].

While studying the turbulence structure of the nocturnal valley winds, Monti et al. [4] showed that katabatic winds have stably stratified layers. Turbulence in each of these layers, is subsided, thus the rate of changing momentum and other properties in the vertical direction reduces. Therefore the down slope flows may have large velocity shears in their vertical structure and they [4] referred them to different air sources around the valley.

Turbulence structure of these flows changes in time, and it depends on the gradient Richardson number, $Ri = N^2/(\partial u/\partial z)^2$ (the critical value of Ri=1) where N is the buoyancy frequency and $\partial u/\partial z$ is the vertical gradient of the horizontal velocity (wind shear).

Fig.1a shows the multilayer structure of velocity and direction and Fig 1b shows potential temperature of a down valley wind at 2:4 LST in Colorado, which the former displays the shear layers. Vertical structure of Ri related to Fig-1a also shows a layered structure.

When Ri >1(strong stability) internal waves prevail with $\omega \le N \cos\theta$ (where ω is the frequency of internal waves and θ is the phase speed angle with respect to horizontal). In closed systems with internal waves, normal mode structure in the vertical direction causes the formation of shear layers [5]. These shearing modes exist in the outflows from semi enclosed to open seas such as Persian Gulf and the Red Sea, and they may lead to breaking up the flow into a number of layers with a vertical scale determined by the structure of the upward propagating wave modes [6].

Monti et al., [4] observed oscillations with long periods in katabatic flows and they attributed them to the internal waves, but they did not mention the role of these waves in causing the layers in down slope valley winds.

Wong et al., [5] observed shear layers in a stably stratified fluid, due to the vertical structure of the normal modes in a laboratory experiment in which the outflow plume at the bottom of the fluid layer had exited these waves and formed these normal modes.

Here we present field observations from katabatic winds in a valley area north of Tehran that show shear layers in the vertical profiles. Then a physical model of a sloped and stratified channel flow driven by an outflow plume is presented. We also represent a model for modal structure of the vertical velocity profile in a stratified channel flow driven by a bottom outflow (as [5]).

2. SOME OBSERVATIONS

Figure 2 shows the vertical profiles of velocity at Geophysics sodar station at the outflow from the Daraka valley north of Tehran at 00.30 local time for the 6th to 9th of February 2003 under a high pressure condition. The city of Tehran into which the outflow enters is in a basin area. The shear layers, as also seen in Monti et al. [4] observations (Fig. 1a), are clearly observed. Wong et al. model [5] predicts the thickness of these layers as $\lambda = 2\pi E(H/W)^{1/2}$, where E is the coefficient of the entraining the plume with the environment,

generating the outflow, H is the depth of the flow (depth of valley or stable boundary layer) and W is the width of the channel (valley). For typical values, W=5 km, E=0.1, H=0.6 km, for the valley in the north of Tehran we found λ=130 m which is in good agreement with the layers thickness observed in the vertical profiles in observations. Fig.3 shows the temporal variation of the flow for three consecutive nights and shows semi regular oscillations which may be due to internal waves. Fig.4 shows the power spectral density of this signal that shows two peaks around 40 and 70 minutes. Here we suggest a physical model on the basis of normal modal structures of the internal waves due to down slope flow that generate these shear layers.

3. NORMAL MODES IN A CONTINUOUSLY STRATIFIED FLUID

In stratified fluid with horizontal scale much larger than the vertical, we use separation of variables technique for solving the governing equations. For small amplitude motions in a rotating fluid it is possible to write equations of motion (x, y and z components of Boussinesq equations and the buoyancy equation respectively) as:

$$\rho(U_t - fV) = -P'_x \tag{1}$$

$$\rho(V_t + fU) = -P'_y \tag{2}$$

$$\rho(W_t) = -P'_z - g\rho' \tag{3}$$

$$\rho_t' + W\frac{d\rho}{dz} = 0 \tag{4}$$

Where U, V, W are the velocity components, f is the Coriolis parameter and P' and ρ' are the deviations in pressure and density fields. If we merge these equations in terms of say W, we find the following (e.g. [7])

$$\frac{\partial^2}{\partial t^2}\nabla^2 W + N^2\nabla_H^2 W + f^2\frac{\partial^2 W}{\partial z^2} = 0 \tag{5}$$

that admits a wave solution as

$$W = \hat{W}(z)e^{i(kx+ly-\omega t)} \tag{6}$$

Where $\hat{W}(z)$ is the normal mode amplitude of the vertical velocity and k, l are the horizontal components of the wave number. By putting (6) in (5) we find

$$\frac{d^2\hat{W}}{dz^2} + \frac{(N^2-\omega^2)(k^2+l^2)}{\omega^2}\hat{W} = 0 \tag{7}$$

That for the boundary conditions of:

$$\hat{W} = 0 \quad \text{at} \quad z = 0 \text{ and } z = H \tag{8}$$

we can write a solution as

$$\hat{W} = \sin\left(\frac{(N^2-\omega^2)(k^2+l^2)}{\omega^2}(z+H)\right) \tag{9}$$

Provided that the eigenvalue $m = \frac{(N^2-\omega^2)(k^2+l^2)}{\omega^2}$ so mH is an integer multiple of π.

$\hat{W}(z)$ is the amplitude of the vertical velocity fluctuations which may consist of several modes, W_n (where n=0,1,2,…).These modes are orthogonal and are called normal modes.

The structure of these functions for different modes is not alike. For example for n=1 ,the function has just one peak, and for n=2, it has two peaks or layers (maxima) and so on, in the vertical profiles of the velocity [5]. Normal modes are also damped with depth due to viscosity and this is observed in lab observations Fig.5 [5].

4. LABORATORY EXPERIMENTS

This experiment was performed in a rectangular water tank with the size of $15 \times 25 \times 350$ cm as sketched in Fig.6. By the filling box method the tank is stratified, and the shape of the density profile is also indicated in Fig.6. The bottom slope angle is 15° and the plume outflow is over the slope with a buoyancy flux of about $3 \times 10^{-8} m^4 s^{-3}$. After about 30 minutes the vertical structure of the normal modes is observed as seen in the dye line from falling dye crystals (Fig.7). Time variations of electrical conductivity which is proportional to density in the experiment is seen in Fig. 8. The power spectral density of this signal is shown in Fig. 9 indicating spectral peaks at about 40 and 90 seconds. Regular fluctuations explain the wavy motions due to internal waves that may cause these layered structures.

4. DISCUSSION

The layered structure of the down slope flow may be due to different sources of air sheds as Monti et al. [4] have indicated. However, as the observations show, semi regular time oscillations in the velocity, that are caused by the low frequency internal waves. We suggest that the normal modes of these waves may lead to the formation the layers, as laboratory experiments show. Although the down slope valley flows may be considered as a semi-enclosed flow as opposed to the laboratory experiments which are in a closed basin, but the vertical structure of the flow, in the two cases are at least qualitatively, similar. Also the top boundary condition has been considered rigid that may be a big approximation, although the stratification in the valley air flow is normally, under high pressure condition, much stronger than that of the free atmosphere above, hence justifying this assumption.

4. CONCLUSIONS

Vertical velocity profiles of down slope valley winds in a stable nocturnal boundary layer is often associated with shear layers. Observations of this type of flow (such as katabatic winds) often show the existence of low frequency internal waves. Observations of down slope flow along the valleys in the northern part of Tehran show long period oscillations (typically longer than 40 minutes). Also vertical profiles of wind speed and direction of this flow show horizontal shear layers which according to the Wong et al.[5]model appears to be about 130 m thick similar to the observed valued. Here we propose a model that the vertical normal modal structure of the low frequency internal waves observed in this flow is responsible for these shear layers. Based on a physical model in laboratory using a plume outflow on a sloped boundary, low frequency internal waves with typical period of 50 seconds seemed to generate the horizontal shear layers. These layers are also observed in Monti et al. [4] but attributed to flows of different origins. Here we argue that such layers are probably due to the presence of low frequency internal waves.

REFERENCES

[1] Whiteman, C. D.: Observations of thermally developed wind systems in mountainous terrain. Chapter 2 in ***Atmospheric Processes Over Complex Terrain***, (W. Blumen, Ed.), Meteorological Monographs, 23, no. 45. American Meteorological Society, Boston, Massachusetts, 5-42, 1990.

[2] Bossert, J. E., and W. R. Cotton: Regional-scale flows in mountainous terrain. Part I: A numerical and observational comparison. *Mon. Wea. Rev.,* 122, 1449-1471, 1994.

[3] Hunt, J.C.R., H.J.S. Fernando, and M. Princevac: Unsteady Thermally Driven Flows on Gentle Slopes, *Journal of the Atmospheric Sciences*, Vol. 60, No. 17, pp. 2169–2182, 2003.

[4] Monti, P., Fernando, H.J.S., Princevac, M., Chan, W.C., Kowalewski, T.A. and Pardyjak, E.R., 'Observations of flow and turbulence in the nocturnal boundary layer over a slope.' *J. Atoms. Sci*., vol. 59, 17, 2513- 2534, 2002.

[5] Wong, A. B. S., Griffiths, R. W. and Hughes, G. O., 'Shear layer driven by turbulent plumes.' *J. Fluid Mech*., 434, 209-244, 2001.

[6] Bidokhti, A. A. and Griffiths, R. E., Internal waves as an additional mechanism for layering in the outflows from semi enclosed seas. ***14th Australasian Fluid Mechanics Conference*** (10-14 Decembar 2001), 2001.

[7] Gill, A. E***., Atmosphere- Ocean Dynamics***. International Geophysics Series. Vol. 30, Acad. Press, 662pp. 1982.

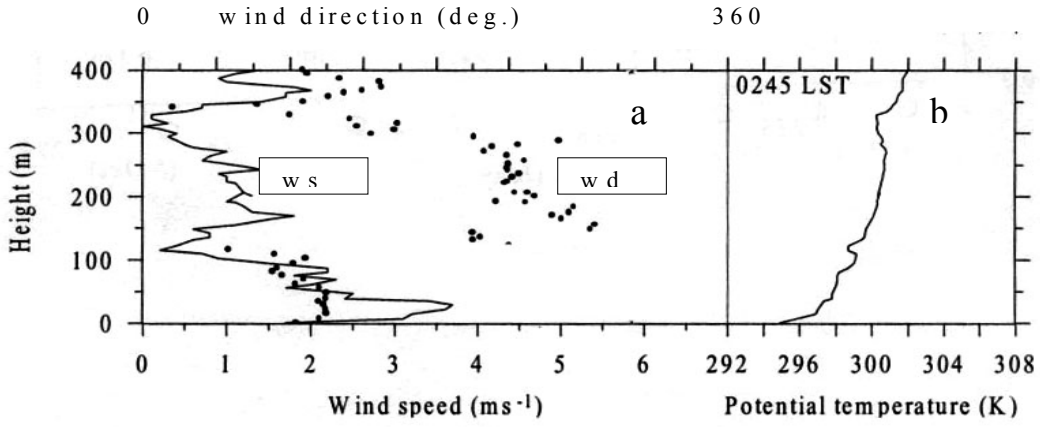

Fig.1a- Vertical profiles of wind speed (ws) and direction (wd); b-potential temperature in a katabatic flow [4]

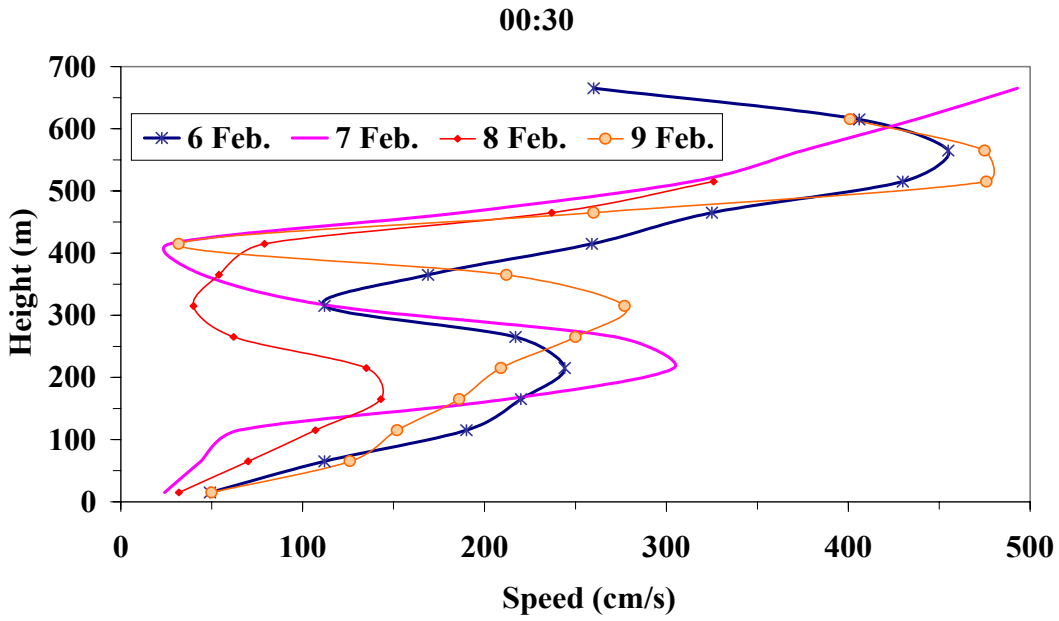

Fig. 2 Vertical profiles of wind speed, measured by sodar at Geophysics station at 00.30

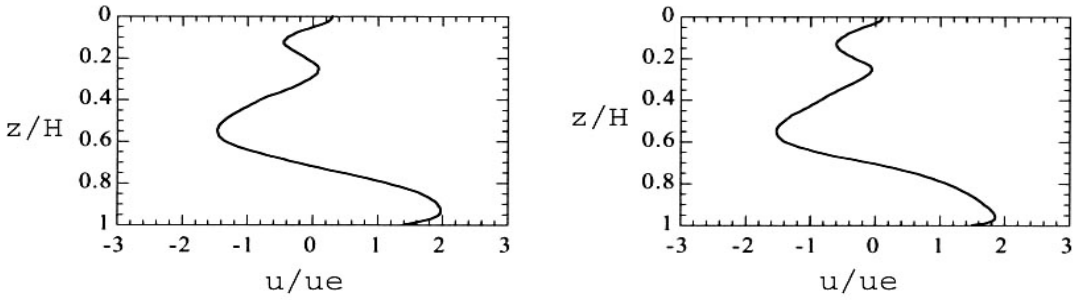

Fig. 3 Typical vertical profiles of velocity (normalized by plume entrainment speed) [5]

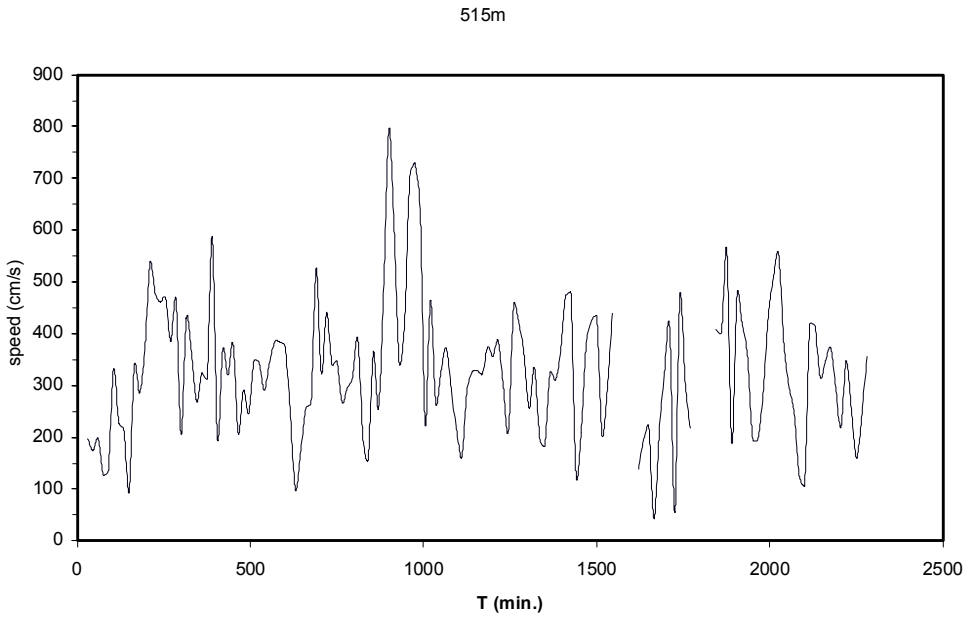

Fig. 4 Typical record of velocity variations at z=515 m during 3 consecutive nights.

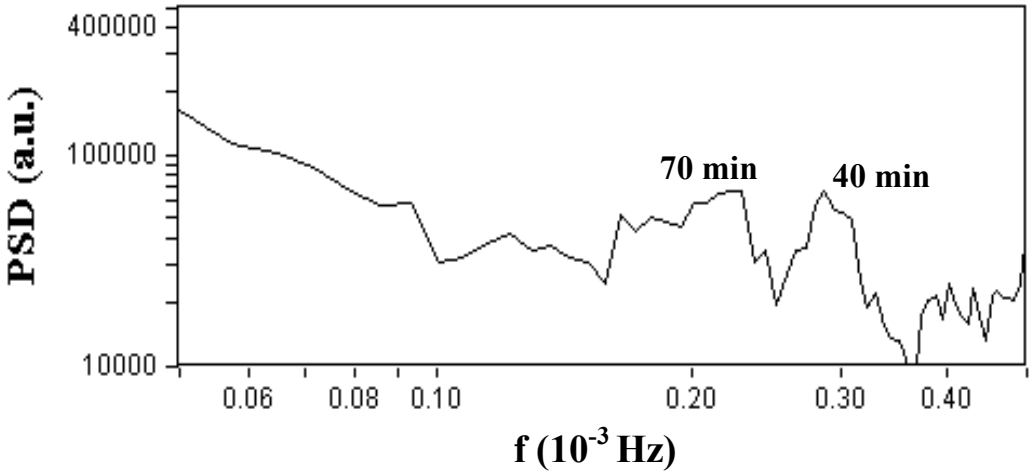

Fig. 5 Power spectral density of signal in Fig. 4

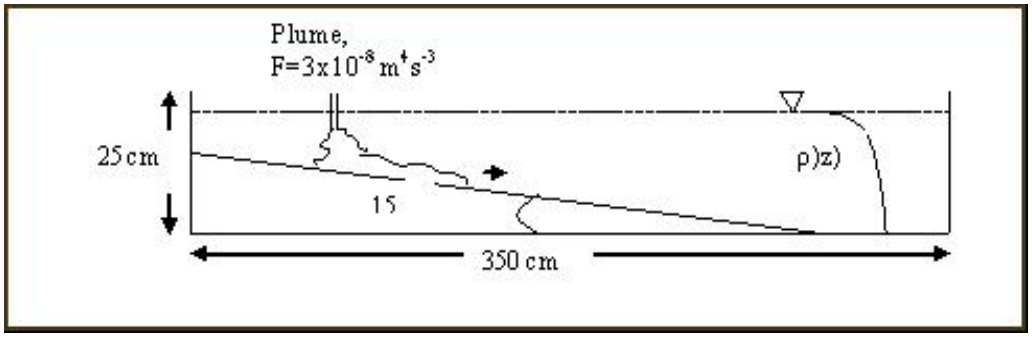

Fig. 6 Experimental set-up

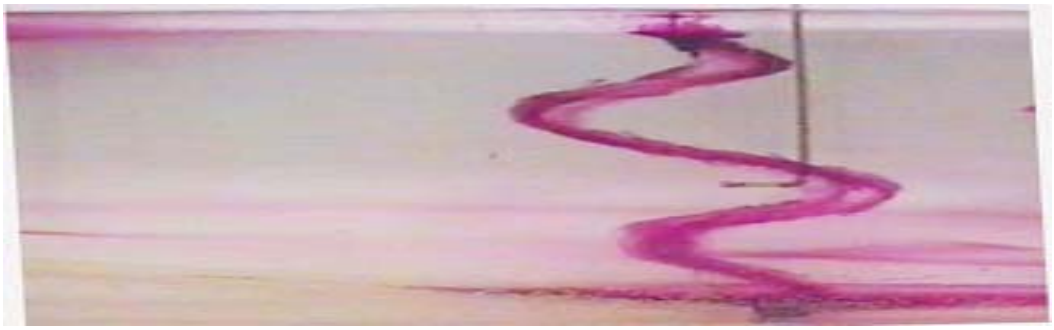

Fig.7 Typical velocity structure in down slope flow in the lab. (notice the conductivity probe as a bent rod).

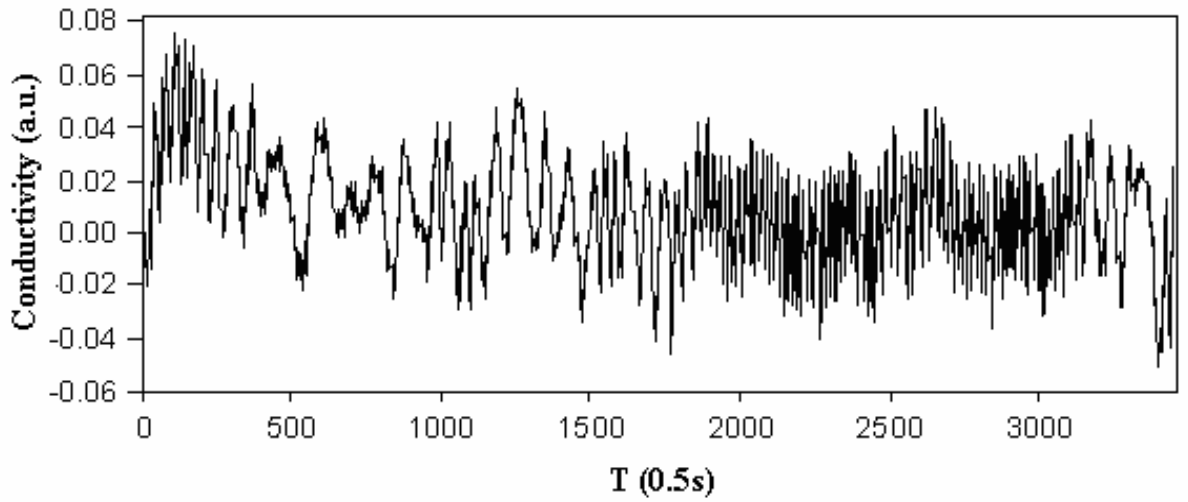

Fig. 7 Conductivity signal observed in the down slope flow in the lab.

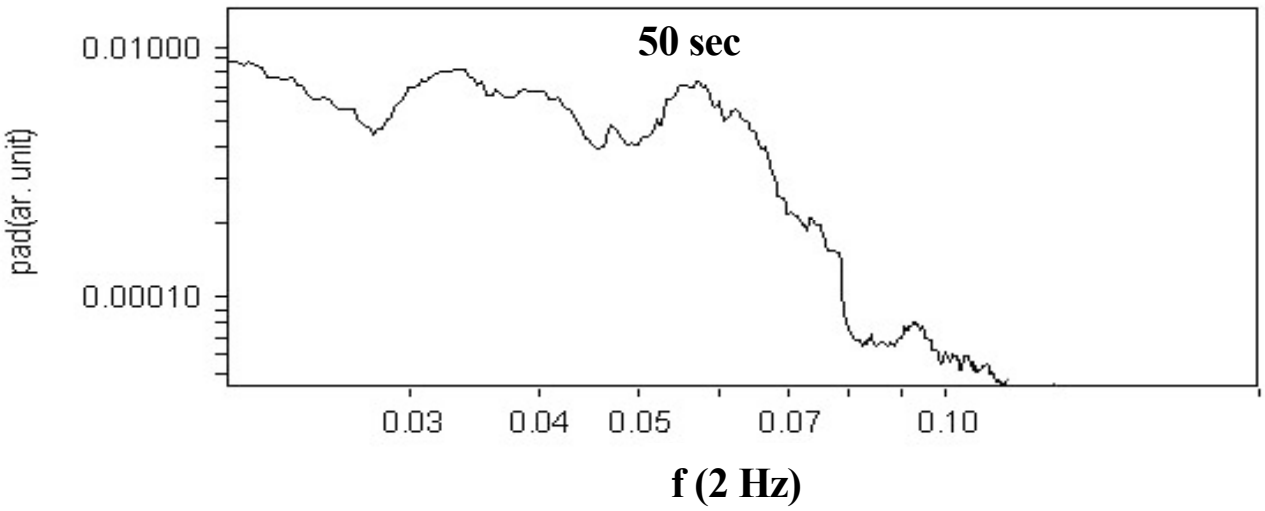

Fig. 8 Power spectral density of the signal shown in Fig. 7

Proceedings of the Tenth Asian Congress of Fluid Mechanics
17-21 May 2004, Peradeniya, Sri Lanka

ARIZONA STATE UNIVERSITY'S CONTRIBUTION TO THE JOINT URBAN 2003 EXPERIMENT: AN OVERVIEW

M. Princevac, R. Calhoun, D. Zajic, J. E. Holeman, R. Heap and H. J. S. Fernando
Department of Mechanical and Aerospace Engineering, Arizona State University, Tempe, AZ 85287, U.S.A.

R. K. Newsom
Cooperative Institute for Research in the Atmosphere, Colorado State University, Fort Collins, CO 80523, U.S.A.

ABSTRACT: During the period from June 28 to July 31, 2003. Joint Urban 2003 Atmospheric Dispersion Field Study took place in Oklahoma City, Oklahoma, USA. The purpose of this study was to study the transport and dispersion of contaminants in urban environments. Knowledge gained from this study will be used to improve, refine and validate computer models that simulate flow in urban areas. Meteorological instrumentation and tracer samplers were installed at various locations in and around the city to provide detailed measurements of the key meteorological variables and tracer gas concentrations. Arizona State University, Environmental Fluid Dynamics Group fielded a suite of instruments, including sonic anemometers, hygrometer, energy balance station and a Doppler LIDAR for whole field velocity measurements.

1. INTRODUCTION

Urban areas of the world are experiencing a rapid growth of population and industrial activity, which have raised serious concerns and problems related to environmental deterioration and public safety [3]. Environment in and around cities is very complex and not well understood. Additionally, increased threat of toxic agents being released into urban atmospheres makes improvement of our understanding and modeling of atmospheric flows in and around cities essential. In order to broaden our understanding of the urban environment, Joint Urban 2003 (JU2003) experiment was conducted in Oklahoma City, Oklahoma, during the period from Jun 28 to July 31, 2003. A number of investigators from government laboratories, universities and private companies are funded by U.S. Department of Defense – Defense Threat Reduction Agency (DTRA), Army Research Office (ARO) and the U.S. Department of Homeland Security (DHS) to conduct the JU2003 study. Details and updates can be found on the official website: http://ju2003.pnl.gov. Arizona State University (ASU) - Environmental Fluid Dynamics Program (EFD) was one of the grantees. The main experimental objective was to provide much needed high-resolution dispersion (transport and diffusion) data at scales of motion ranging from flows in and around a single city block to the scale of the suburban area covering several kilometers from the downtown. These data will be used to evaluate and improve existing outdoor dispersion models, including fine-scale computational fluid dynamics models, and fast-response dispersion models that typically rely on empirical or semi-empirical relationships describing the atmospheric processes [6]. The data will lead to improved algorithms and parameterizations within these models.

Meteorological instruments and tracer samplers were positioned in such a way to enable resolving atmospheric dispersion at scales of motion ranging from flows in and around a single city block, around several blocks in the downtown Central Business District (CBD), and into the suburban Oklahoma City (OKC) area, several kilometers from the CBD. Besides the dispersion related problems, JU2003 data set is of great importance in addressing many other issues associated with urban environments (e.g. heat island effect). In Section 2 ASU's instrument deployment is described. Some examples from the preliminary data analysis are given in Section 3.

2. EXPERIMENTAL SETUP

The instrumentation deployed by the ASU team consisted of a Coherent Technologies, Inc. Doppler LIDAR (LIght Detection And Ranging), 3-D sonic anemometers, radiation sensors, infrared temperature sensors, thermistors, soil heat flux plate and soil water content sensor. Instruments were located in three separate locations: the Lidar location, Energy station location and an urban canyon (sonics) location (see Figure 1). The LIDAR was located approximately four kilometers to the south-southeast from the CBD on the southwest corner of 25th Street and Amin Drive (N 35°26.330', W 97°29.533', and altitude 384 m above MSL). The LIDAR operated during the Intensive Observational Periods (IOPs), as well as during non IOPs. Most of the scanning strategies were coordinated with the

Army Research Laboratory (ARL) LIDAR group to capitalize on the opportunity for Dual Doppler scanning strategies ([7], [4]). The first (sonic instrumented) tower was located in the CBD on the northwest end of the Park Avenue, close to the Broadway Avenue. It was equipped with three sonic anemometers (sampling rate 10Hz): Applied Tech. at 2.5m above ground level (agl), Young at 5m agl, and Metek at 8.5m agl. Besides sonic anemometers, an IR sensor (sampling rate 8Hz) was mounted on the same tower to measure street surface temperature. Raw data from three velocity components and temperature were stored. One minute averages and rms of the surface IR temperature were stored. The Young sonic and the IR thermometer were working 24/7 during the whole campaign period. During the first part of the campaign, the two other sonics were working only during the IOPs. Starting with the IOP 6, all three sonics operated continuously. Second ("Energy") tower was located on the grassy field with a slope angle 1.3 deg near the intersection of N Walker Avenue and NW 11th Street. Energy Tower was located at N 35°28.764', W 97°31.202', and 378 m MSL and was instrumented with: Kipp and Zonen Net Radiometer at 9.2 m agl, one cup anemometer at 8.9 m agl and the other at 1.5 m agl, one thermistor at 8.3 m agl and the other at 1.1 m agl, IR thermometer, upward facing pyranometer and downward facing pyrgeometer at 3.5 m agl, 3D Sonic anemometer (Campbell Sci.) and Krypton Hydrometer at 2.5 m agl. A soil heat flux plate (6.5 cm below the ground level), six thermistors (2 x 2 cm, 3 cm, 4 cm, 5 cm and 8 cm below the ground level) and a soil water content reflectometer were added on July 13. Data from the net radiometer, cup anemometers, thermistors, pyranometer, pyrgeometer and soil heat flux plate were stored as five-minute averages. Data from IR thermometer, sonic anemometer, Krypton Hydrometer and soil water content reflectometer were stored as one minute averages. For both IR sensors, emissivity of the surface was assumed as unity.

Fig. 1: Locations of the ASU experimental sites during the JU2003 experiment. Interstate highways I-40 (West-east) and I-35 (235) (North-south) are visible. Location of the sonic tower in the CBD is marked with a star (north of I-40); energy tower is marked by circle (further north from I-40) and LIDAR location is marked with triangle (far south, west of I-35).

3. MEASUREMENTS

Skin temperature measured at two sites, downtown (street canyon) site and energy tower site (open grassy field) are presented in Figure 2 for a five day period (190 to 195 Day of Year[1]; July 10 to July 15). A warming trend throughout these five days can be noted. Sharp increase of temperature above the open grassy field occurs several hours after sunrise. Sunrise time was around 6:30 AM local time and skin temperature begins rising around 8:30 AM. Morning heating in the urban canyon is retarded due to the shading effects of the buildings. As the solar input starts penetrating into the urban canyon, skin temperature starts its fast growth around 10:30 AM. During the daytime skin temperature in urban canyon is slightly lower, again due to the shading effects of buildings and trees located on the sidewalk. Temperature begins to drop rapidly around 4:00 PM at both sites. However, after one hour the temperature drop in urban canyon slows down, but continue to cool steadily through the night until warming takes place in the morning. On the other hand, skin temperature in the open field keeps very rapid cooling rate (~ 9 ^{o}C/hour) until it reaches a state with very low cooling rate (~ 0.17 ^{o}C/hour)) that lasts until morning.

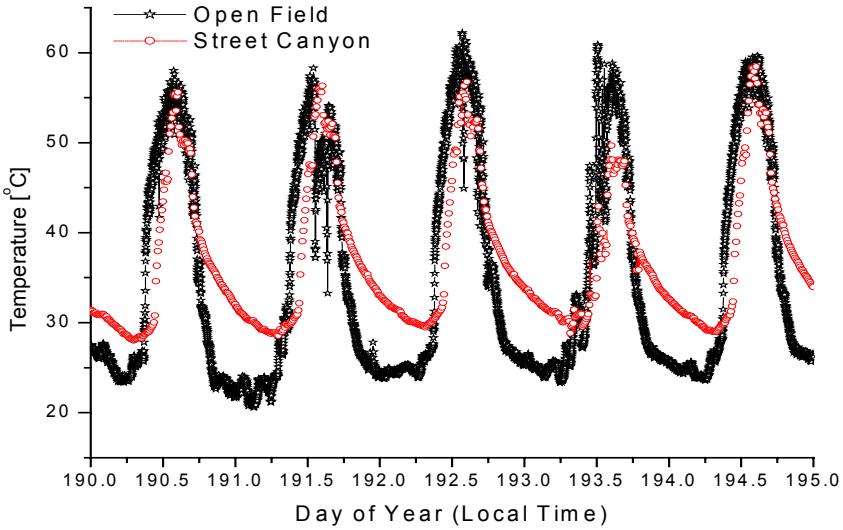

Fig. 2: Surface ("skin") temperatures measured in street canyon and in open grassy field

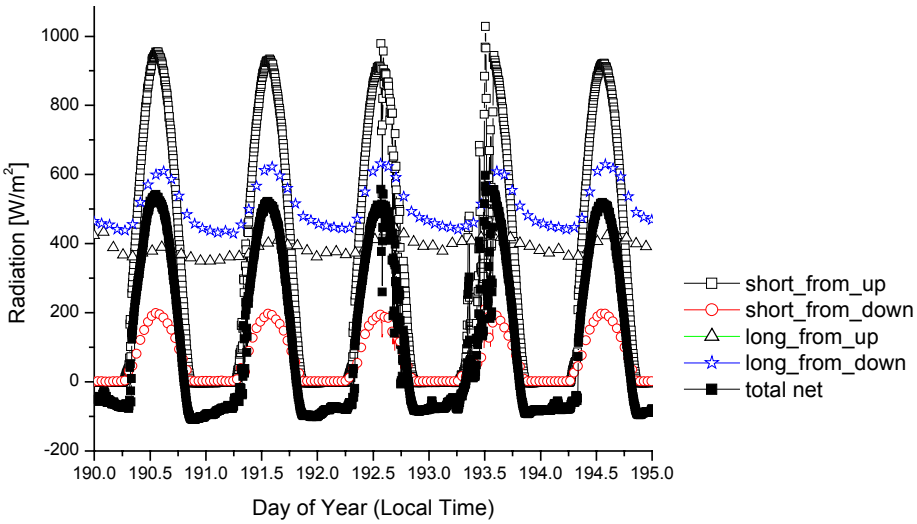

Fig. 3: Incoming and outgoing short (0.3 to 3 µm) and long (5 to 50 µm) wave radiation components and total net radiation measured at the Energy Tower site.

[1] January 1st at 0:00 (midnight December 31st) is 0.0 Day of Year. This means that January 1st at noon is 0.5 DofY.

Note the nighttime temperature difference between two sites, which is on the average 7 ^{o}C. Having in mind that the two sites were only 1.3 kilometers apart, this significant temperature difference points to the urban heat island effect introduced by the high heat capacity land use material in the CBD. Figure 3 presents radiation measurements taken at the Energy Tower's site for the same period as in Figure 2. Daytime incoming radiation excess (positive net radiation) produces soil heating, sensitive and latent heat flux. Nighttime radiation deficit (negative net radiation) cools the ground and eventually can produce negative sensitive and latent heat flux.

The highlight of the ASU's instrumentation was a Doppler LIDAR. It can make fast three-dimensional scans measuring wind speed and relative aerosol concentration. Its location (see Figure 1) allowed scanning of flows upstream of the CBD (the predominant winds were Southeasterly). ASU group took the opportunity of scanning the firework celebration on July 4, performing PPI (Plan Position Indicator) scans over CBD where the firework display took place. Figure 4 shows two PPI scans, in which the firework's smoke plume can be seen. Winds were southerly with small westerly component (approximately 7.5 m/s).

To our knowledge this is the first time that a two (Dual) Doppler LIDAR setup was deployed to collect data in both daytime and nighttime boundary layers. Single LIDAR is capable of collecting radial velocity component, but a dual setup can yield a complete three-dimensional velocity field. This technique is already adopted for radars, and it is at initial stage for LIDARs. Figure 5 presents velocity field obtained from co-planar coordinated PPI scans with ARL's LIDAR.

Further analysis of LIDAR data will include mapping of flow above the buildings. Velocity profiles in the urban boundary layer (UBL) will be compared with theoretical profiles [1] and those derived using laboratory experiments (These experiments are in progress at ASU). The response of turbulence to the building cluster will be of interest in dealing with neighborhood-scale modeling [5]. The mean profiles are expected to respond to the turbulent shear stress adjustments taking place in the urban boundary layer, which should be evident from LIDAR's mean profiles. Recently, a model has been developed [2] to predict the adjustment of mean profiles due to the presence of an urban canopy, which changes the structure of turbulence. The predictions of this model will be evaluated using the JU2003 LIDAR data and laboratory measurements.

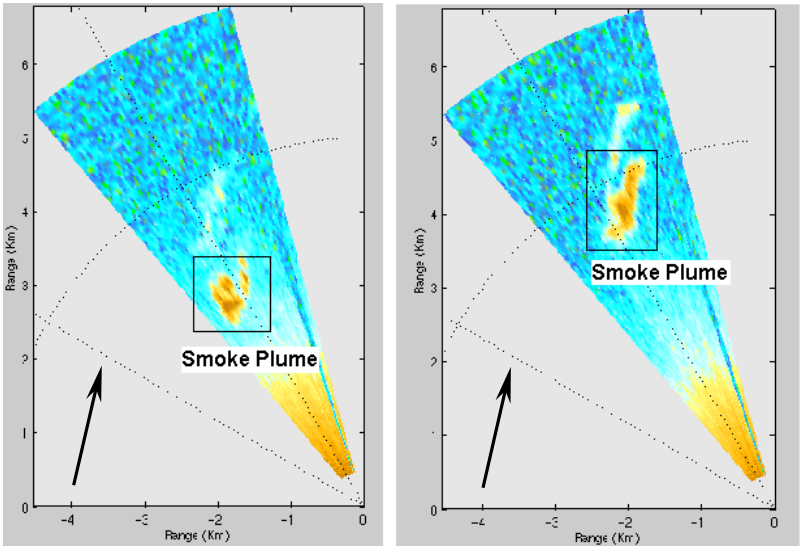

Fig. 4: ASU LIDAR tracks smoke plumes in Oklahoma City (July 4, 2003). Arrows represent mean wind direction. Time interval between these two scans is 4 minutes.

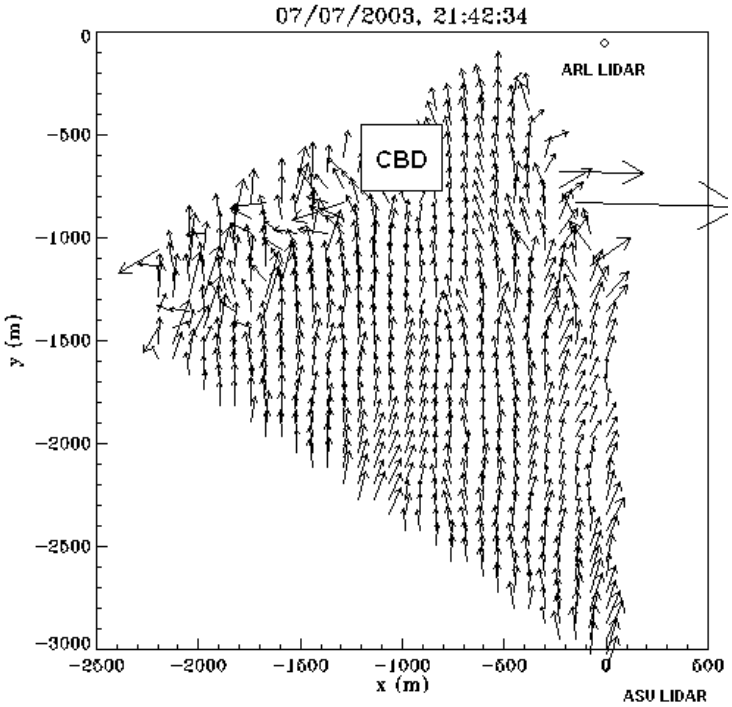

Fig. 5: Velocity wind vectors south of the CBD Oklahoma City.

ACKNOWLEGMENTS

This research was supported by the grants from Army Research Office, U.S. Department of Defense and U.S. Department of Energy. The authors wish to acknowledge Drs. Jerry Allwine (PNNL), Marty Leach (LLNL), Walter Bach (ARO), Michael Brown (LANL), Eric Pardyjak (UofU), David Ligon (ARL) and Edward Creegan (ARL) for their invaluable help and support during the study period. Special thanks goes to Coherent Technologies Inc. for rapid field support.

REFERENCES

[1] Cionco , R.: A Mathematical Model for Airflow in Vegetative Canopy. *J. Appl. Meteor*., 1965, **4**, 517-530.

[2] Coaceal, O. and Belcher, S.E.: Adjustment of Rural Boundary Layer to a Heated Urban Canyon, *4th Symposium on Urban Environments*, Norfolk, VA, 20-24 May, 2002, 213-214.

[3] Fernando, H. J. S., Lee S.M., Anderson J., Princevac M., Pardyjak E., and S. Grossman-Clarke: Urban Fluid Mechanics: Air circulation and contaminant dispersion in cities, *Env. Fluid Mech.,* 2001, **1**, 107-164.

[4] Hannon, S.: WindTracer Doppler Lidar Measurements for the 2000 Urban/SF6 VTMX Program, Coherent Technologies, Inc. Test report, CTI-TR-2001-02, 2001.

[5] Jerram, Perkins, J.R., Fung J.C.H., Davidson, M.J., Belcher, S.E. and Hunt, J.C.R.: Atmospheric Flow through a Group of Buildings and Dispersion from Isolated Sources. *Wind Climate in Cities* (Eds. J.E. Cermak, A.D. Davenport, E.J. Plate and D.X. Vegas) Kluwer Publishers, Dordrecht, 1994, 109-130.

[6] Joint Urban 2003 Atmospheric Dispersion Study, Oklahoma City, Jun-July 2003. Experimental Plan

[7] Newsom, R.K., Banta, R.M.: Shear-flow instability in the stable nocturnal boundary layer as observed by Doppler lidar during CASES-99. *J. Atmos. Sci*., 2003, **60**(1): 16-33.

Proceedings of the Tenth Asian Congress of Fluid Mechanics
17-21 May 2004, Peradeniya, Sri Lanka

HIGH-RESOLUTION DYNAMIC REGIONAL CLIMATE DOWNSCALING OVER SRI LANKA

J.-H. Qian and L. Zubair
International Research Institute for climate prediction, LDEO, Columbia University, Palisades, NY 10964, USA

ABSTRACT: The ensemble dynamic regional climate downscaling is studied by using a global atmospheric general circulation model ECHAM4.5 and a regional climate model RegCM3. The regional climate model with high resolutions of 100km and 20km grid downscales large-scale global model outputs to generate regional mesoscale climate information over South Asia.

1. INTRODUCTION

By using electronic computers, weather and climate on the earth have been simulated by atmospheric and oceanic numerical models, with either global or regional domains. Because of the constraint of computational resources, current climate prediction global circulation models (GCMs) typically use coarse resolution with grid size of about 200-500km, which is too coarse for users in applications such as hydrology, agriculture, etc. One solution to this problem is to drive a regional climate model with higher resolution (20-100km grids) over the area of interest by a GCM simulation, to get more detailed regional information.

Sri Lanka is an island country in South Asia with the east-west width of 224 km and the north-south length between 400 and 500 km. A mountain range with a narrow peak over 2 km is in the middle of the country. Located in the center of the monsoon region, the climate of Sri Lanka is strongly affected by monsoon and orography. In this study, the numerical simulation covers the second intermonsoon season (SIM, October-November) and the Northeast monsoon season (NEM, December-February).

2. ATMOSPHERIC MODELS AND EXPERIMENTAL DESIGN

ECHAM4.5 is a spectral atmospheric GCM with T42L19 resolution (triangular truncation at wavenumber 42 corresponding to the horizontal grid size of 250-300 km, and 19 levels in the vertical) [1]. The model is based on Navier-Stokes equations of the atmosphere with a hydrostatic approximation in the vertical. The prognostic variables are vorticity, divergence, surface pressure, temperature, specific humidity, and mixing ratio of total cloud water. Seven members of the AMIP run (atmospheric model forced by observed sea surface temperature, SST) is used to drive the regional climate model RegCM3.

RegCM3 was developed by the Physics of Weather and Climate Group at the Abdus Salem International Center for Theoretical Physics (ICTP), Trieste, Italy. Its dynamical core is close to that of the hydrostatic version of the Penn State/NCAR Mesoscale Model version 5 (MM5), a grid-point model (with Arakawa-B grid) based on primitive atmospheric equations. The vertical resolution is based on a pressure-based terrain-following sigma coordinate.

RegCM3 is driven by lateral boundary conditions provided by the ECHAM4.5. To avoid discrepancies between the outer driving fields and the model internal physics, an exponential relaxation scheme is applied in the lateral buffer-zone with a width of 12 grid intervals, which consists of Newtonian and diffusion terms added to the model tendency equations for wind components, temperature, water vapor mixing ratio, and surface pressure [2, 3].

The RegCM3 is run over South Asia with 100km and 20km grid size, with its domain and the topography shown by Fig.1a and 1b, respectively. The domains are centered over Sri Lanka at (7.5N, 80.5E). The 20km-grid runs use a smaller domain than the 100km-grid runs because of the restriction of computational cost. The 20km run would be 125 times more expensive in computational cost than the 100km run, if the same model domain were adopted. Because of the strong orographic effect on the rainfall in Sri Lanka, the

adequate representation of terrain in the regional model is desired. Figure 1 shows that the 100km-grid resolution only gives a mountain top less than 200 m, but the 20km-grid shows a peak value over 1000 m. Due to the orographic effect, the climate over the western and eastern hillslopes of Sri Lanka strongly depends on the seasonal change of predominant wind directions.

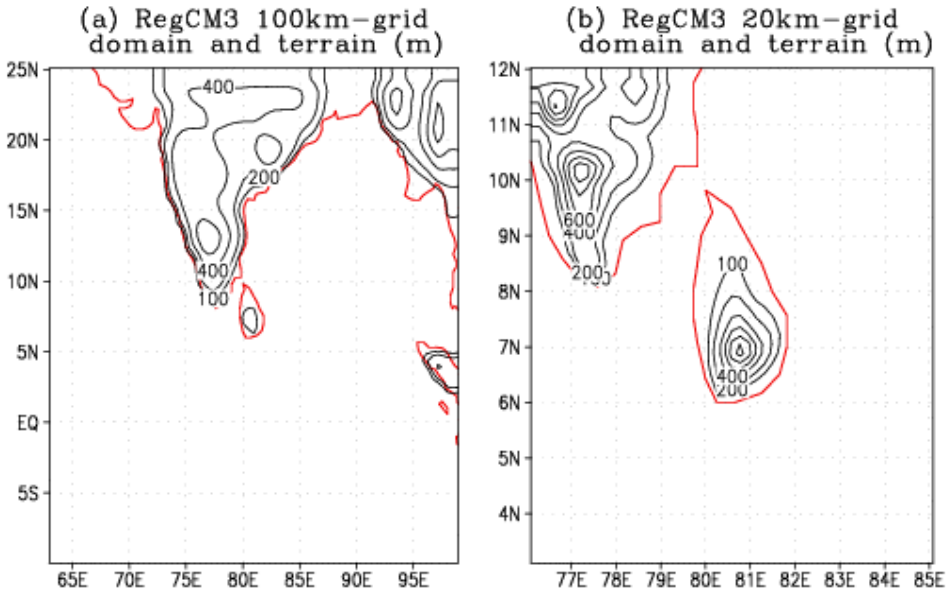

Fig.1 The 100km-grid (a) and 20km-grid (b) model domain and topography (m).

3. SPATIAL DISTRIBUTION

The simulated precipitations were compared to three observational datasets: (1) the TRMM satellite rainfall observation (1.0x1.0 degree grid), (2) the Climate Prediction Center (CPC) Merged Analysis of Precipitation (CMAP), a blended monthly precipitation dataset (2.5 x 2.5 degree grid) using gauge, satellite observations and numerical model results, and (3) the gridded station observation (0.2x0.2 degree grid) covering Sri Lanka.

Figure 2 shows the observed (left three panels) and model simulated (right three panels) monthly precipitation (in unit mm/day) and 850hPa winds of October 2000. The resolutions of CMAP and TRMM data (panel a, b) are too coarse to represent the fine spatial structure of the topographic rainfall over Sri Lanka shown by the 0.2-degree gridded station precipitation in panel c. The 850hPa winds of the NCEP-NCAR reanalysis are also shown in Fig.2a, as a validation for the model simulated winds. In October 2000, northwesterly wind is predominant in the lower atmosphere over Sri Lanka. In the ECHAM simulation, the wind direction is westerly, and the wind speed is smaller than that in the NCEP-NCAR reanalysis. The resolution of ECHAM4.5 is so coarse that the area of a grid box is almost as large as Sri Lanka, therefore, it is unable for the GCM to solve the fine-scale spatial distribution of fields within the island. In the RegCM3 simulation with 100km grids, which more than doubles the resolution of ECHAM4.5, the magnitude and direction of the winds are still very similar to its driving fields from ECHAM, and the resolution is still not fine enough to simulate the orographic effect on precipitation. The maximum precipitation is in the northern Sri Lanka, different from the TRMM and station observations. The RegCM3 runs with 20km grids, which has a mountain top of 1000 m, produced orographic precipitation near the central mountain. However, the precipitation center is near the mountain top, while in the station observation, the rainfall maximum is in the windward side of the western hillslopes. The wind field in the RegCM3 20km-grid runs is similar to that of the 100km-grid runs as well as the ECHAM simulations, indicating the dominant role of mechanical forcing from the GCM to the regional model.

Similarly, in the NEM season, the RegCM3 20km-grid runs captured the orographic effect on the rainfall. The northeasterly winds in December 2000 are faithfully simulated by both the ECHAM and RegCM3 in magnitude and direction (figure not shown). But the RegCM3, particularly the 20km-grid runs, simulated more rainfall in the eastern hillslopes than in the western hillslopes, as in the observations, the feature that cannot be seen in the ECHAM simulation. Hence, the high-resolution regional model can provide geographically more detailed climate information for the local users.

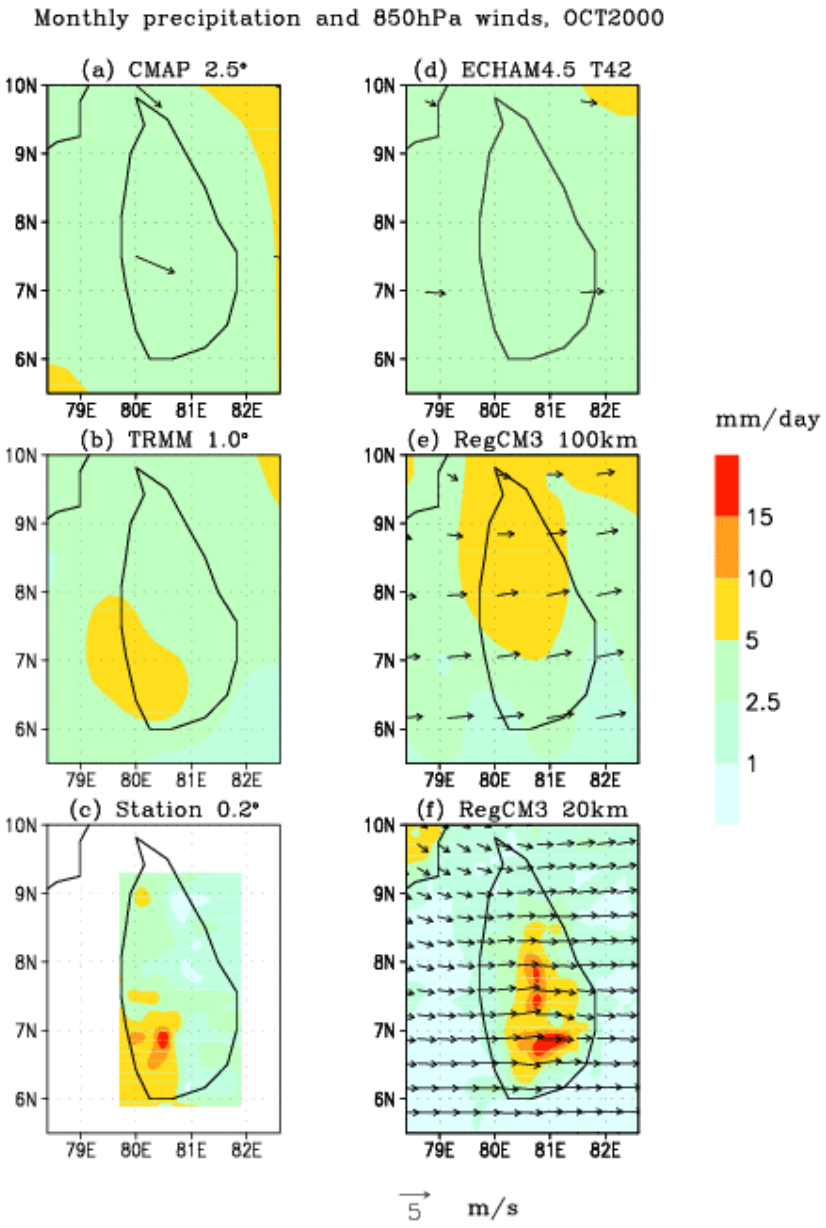

Fig.2 October 2000 monthly precipitation (shaded, mm/day) and 850hPa winds. (a) CMAP precipitation and NCEP-NCAR reanalysis winds; (b) TRMM precipitation; (c) gridded Sri Lankan station precipitation; (d) Seven-member ensemble mean precipitation and winds of the ECHAM4.5 T42; (e) Seven-member ensemble mean precipitation and winds of the RegCM3 with 100km grid resolution; (f) Seven-member ensemble mean precipitation and winds of the RegCM3 with 20km grid resolution.

4. TIME SERIES

The monthly precipitation time-series of the GCM and regional model simulations are plotted to compare with the observational time series, as shown in Fig. 3. The area averaged monthly precipitations in the western, eastern, and all Sri Lanka are shown in the top, middle, and lower rows of panels, respectively. And the results of the ECHAM4.5, RegCM3 100km-grid runs, and the RegCM3 20km-grid runs are in the left, middle and right columns of three panels, respectively. The solid lines are the model-simulated results, thin solid for seven ensemble realizations, and thick solid for ensemble mean. For observations, the dashed line is the station observation (the dotted line is the long-term averaged climate value of precipitation for each month, plotted as a reference), the dot-dashed line is the TRMM precipitation, and the long-short-dashed line is the CMAP precipitation.

The station precipitation of October 2000 is less than half of its climate value, indicating it is a month of rainfall deficit. November 2000 is the rainiest month in this period, then the precipitation decreases in the NEM season, from December to February. The TRMM precipitation also shows similar trends, except that precipitation increased slightly from January to February. The 2.5-degree grid CMAP data are too coarse to give separate lines for eastern and western Sri Lanka, but only showing the averaged precipitation of Sri Lanka as a whole. The temporal trends of the CMAP and TRMM data are similar to that of the station observations. However, the magnitudes of the CMAP and TRMM data are significantly smaller than the station data, particularly from November to January and in eastern Sri Lanka.

The simulated rainfall intensity is underestimated by ECHAM4.5. The rainfall is increased in the downscaled RegCM3 simulations. However, the rainfall intensity in the RegCM3 100km-run is still too low. The 20km-grid runs has increased the intensity to the similar magnitude to the observations, but the spread or the variance among the ensemble members is also increased.

As for the temporal evolution of the monthly precipitation, it decreased from October to November in the ECHAM4.5 and the RegCM3 100km-grid runs, opposite to the observations. The RegCM3 20km-grid simulation gives the correct trends, with the maximum rainfall in November, consistent with observation.

5. CONCLUSION

By using a regional climate model RegCM3, the GCM ECHAM4.5 ensemble simulations have been downscaled over Sri Lanka. The high-resolution of 20km grid is needed for the RegCM3 to produce reasonable spatial distribution of precipitation which is strongly affected by the island's topography. The high-resolution regional model also corrects the intensity and temporal trend of the precipitation in this simulation period. Further studies will be in the examination of high-resolution precipitation processes [4, 5, 6] and the application of the variable-resolution stretched grids to focus high-resolution of the RegCM3 over Sri Lanka [7, 8].

ACKNOWLEDGMENTS

We wish to thank Dr. Filippo Giorgi and the ICTP Physics for Weather and Climate Group, the developers of RegCM3. Thanks also to Huilan Li and Sara Rauscher for processing ECHAM and observed data. The International Research Institute for climate prediction (IRI) represents a cooperative agreement between U.S. NOAA Office of Global Programs and Columbia University.

.

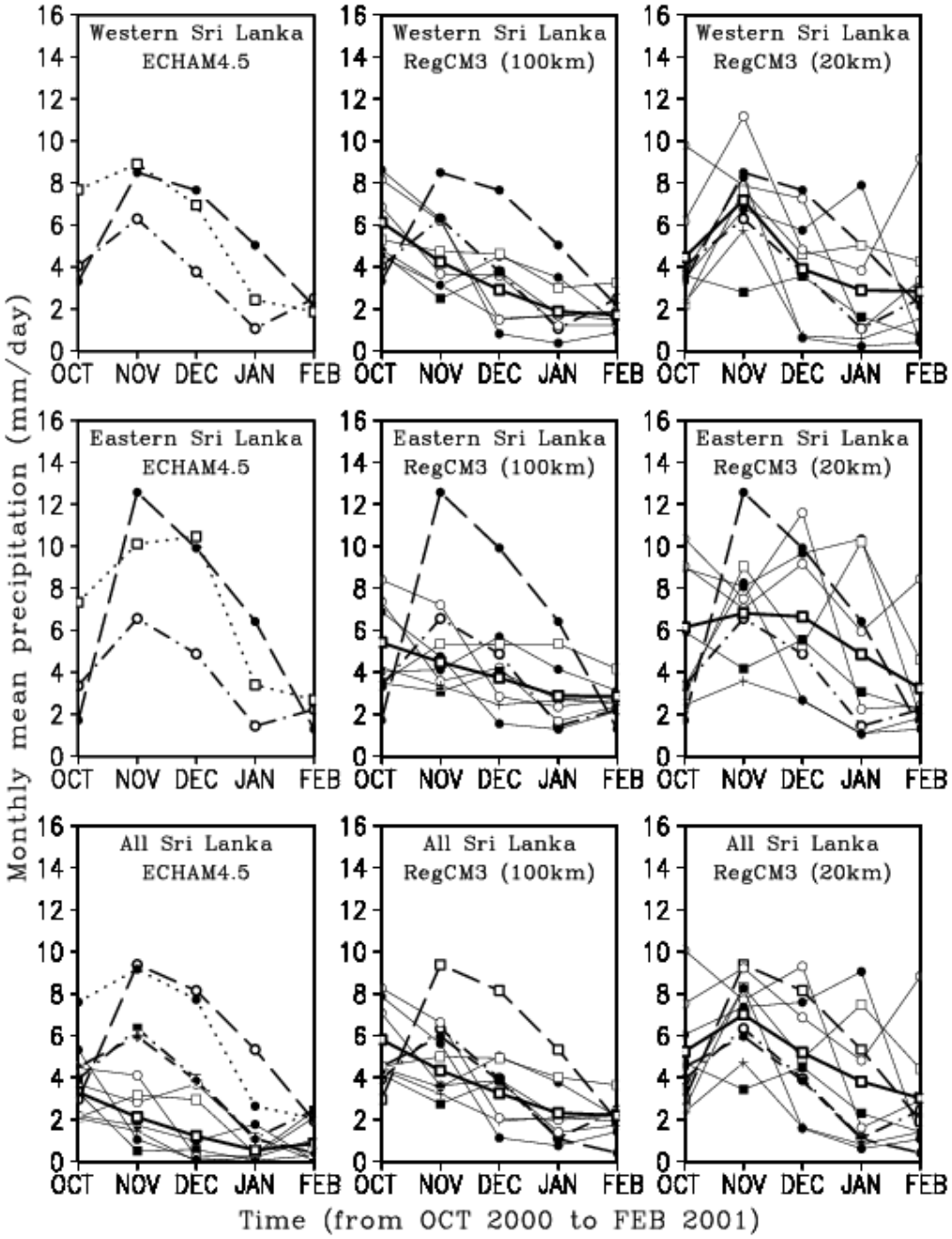

Fig.3 Time-series of monthly precipitation (mm/day) from October 2000 to February 2001. The observations are station observation (dash), climate mean of station observation (dot), TRMM (dash dot), and CMAP (long short dash). The thin solid lines are the seven ensemble realizations, and the thick solid line is the ensemble mean. The area averaged monthly precipitations in the western, eastern and all Sri Lanka are shown in the top, middle, and bottom rows of panels, respectively. The simulation results of the ECHAM4.5 GCM, RegCM3 100km-grid runs, and the RegCM3 20km-grid runs are in the left, middle and right columns of three panels, respectively.

REFERENCES

[1] Roeckner E and Coauthors: The atmospheric general circulation model ECHAM4: model description and present-day climate. Max-Planck-Institut fur Meteorologie Rep. 218, 1996, Hamberg, Germany, 90pp.

[2] Giorgi F., Marinucci MR, Bates GT: Development of a second generation regional climate model (RegCM2). Part II: convective processes and assimilation of lateral boundary conditions. *Mon. Wea. Rev*. **121**, 2814-2832.

[3] Qian JH, Seth A, Zebiak S: Reinitialized versus continuous simulations for regional climate downscaling. *Mon. Wea. Rev*. 2003, **131**, 2857-2874.

[4] Qian JH, Tao WK, Lau KM: Mechanism for torrential rain associated with the Mei-yu development during SCSMEX 1998, *Mon. Wea. Rev*. 2004, **132**, 3-27.

[5] Qian JH, Semazzi FHM, Scroggs JS: A global nonhydrostatic semi-Lagrangian atmospheric model with orography. *Mon. Wea. Rev*. 1998, **126**, 747-771.

[6] Qian JH, Kasahara A: Nonhydrostatic atmospheric normal modes on beta-planes. *Pure Appl. Geophys*. 2003, **160**, 1315-1358.

[7] Qian JH, Giorgi F, Fox-Rabinovitz MS: Regional stretched grid and its application in the NCAR RegCM. *J. Geophys. Res*. 1999, **104**, 6501-6514.

[8] Qian JH, Zebiak SE, Giorgi F: A regional climate model with a variable-resolution stretched grid. *Mon. Wea. Rev*. 2004, pending review.

Proceedings of the Tenth Asian Congress of Fluid Mechanics
17-21 May 2004, Peradeniya, Sri Lanka

APPLICATION OF THE P-VECTOR METHOD TO THE CIRCULATION IN THE WESTERN NORTH PACIFIC

R. F. Li and X. B. You
LASG, Institute of Atmospheric Physics, Chinese Academy of Sciences, Beijing 100029, China

P. C. Chu
Department of Oceanography, Naval Postgraduate School, Monterey, CA 93943, USA

ABSTRACT: By using the P–vector method on isopycnal surface, the monthly circulations in the western North Pacific are calculated from the Navy's Generalized Digital Environmental Model (GDEM) climatological temperature and salinity data on a $0.5° \times 0.5°$ grid. The basic current system, consisting of the North Equatorial Current, Kuroshio and its Countercurrent, the Subtropical Countercurrent (STCC) has been well revealed by the method. Emphasis is on discussing STCC in this paper. At $\sigma_\theta = 24.6$ kg m^{-3} surface which locates in the flow core of STCC, the distribution and origin as well as flow status of STCC have strongly seasonal variability. From May to November, a branch is separated from the Kuroshio Countercurrent south of Japan, and then merges into STCC, which makes the velocity of STCC increasing andits width widening. The eastward volume transport of STCC across 139.5° E is the strongest in summer with a maximum of 8.7 Sv (1 Sv$=10^6$ m^3 s^{-1}) in August, and weaker in spring with a value of 1.8 Sv in April.

1. INTRODUCTION

The classic Sverdrup theory suggests that the water movement in the central subtropical gyre of the North Pacific Ocean should be slowly westward or southwestward. In the mid of 1960s, the existence of a curious eastward flow at 20° ~ 25° N in spring was theoretically predicted and it was named the Subtropical Countercurrent (STCC) although direct observational evidence was yet insufficient to confirm whether or not the eastward flow at 20° ~ 25° N was of any persistent and continuous flow at that time [1]. Features similar to those of the eastward transports appear in the South Pacific, North Atlantic and South Indian Ocean [2]. This means that STCC is a worldwide phenomenon. Therefore, the study of STCC is useful to understand the current system in the world. Since STCC was predicted, investigations of its existence and forming mechanism have continued. The existence of STCC is not doubted, but the spatial distribution of STCC still remains earlier stage. In addition, most of previous studies excluded the area of the western North Pacific, and lacked analysis of the vertical structure of STCC, and also couldn't discuss the origin of STCC. The data of temperature and salinity observed in an extensive area last 40 years are fairly precise, hence they should contain more information of STCC. With Navy's GDEM data and P-vector method, the monthly three-dimensional absolute velocity fields in the western North Pacific are

calculated. The velocity vector field on isopycnal surface more vividly shows the flow status of STCC. In this paper we analyze the horizontal distribution, vertical structure and seasonal transport of STCC.

2. NAVY'S GDEM DATA AND P-VECTOR METHOD ON ISOPYCNAL SURFACE

Data used in this paper are from the Navy's GDEM climatological temperature and salinity dataset with 0.5° × 0.5° resolution and a four-dimensional (latitude, longitude, depth, and time) display [3]. Data for building the current version of GDEM were obtained from Navy's Master Oceanographic Observational Data Set (MOODS), which has more than 5 million profiles during 1920 ∽ 1998.GDEM appears to render better representations of seasonal variability and regions of high current shear [3]. So it is useful to study STCC. The domain extends from 120° E to 145° E and from 0.5° N to 50° N. In order to resolve well the vertical structure of the stratification, we use a cubic spline to interpolate the T, S data into 246 z-levels with four different increments: 5 m from 0 to 100 m, 10 m from 100 m to 1000 m, 20 m from 1000 m to 2500 m, and 50 m below 2500 m depth. The sea surface (0 Pa) is taken as a reference level for calculating potential density, σ_θ (kg m^{-3}). We make discretization with a increment, $\Delta\sigma_\theta$=0.025. Thus we have 222 σ_θ–layers from 22.2 σ_θ to 27.725 σ_θ.

The P–vector method on isopycnal surface has been introduced in detail [4.5]. With assumptions of geostrophic balance, hydrostatic balance and incompressible approximation, dynamic principles, such as "thermal wind relation", conservation of mass are satisfied. Then we can lead to the conservation of potential vorticity q on isopycnal surface,

$$u\frac{\partial q}{\partial x}+v\frac{\partial q}{\partial y}=0 \tag{1}$$

Where $q=fg\left(\frac{\partial p}{\partial \rho}\right)^{-1}$, p is a pressure. The equation (1) leads to the fact that any water particle should move along q isolines on isopycnal surface, that is, any q isoline is a trajectory of water particles. For each trajectory, we can define a unit tangential vector,

$$\vec{c}=\frac{1}{|\nabla q|}\left(\frac{\partial q}{\partial y}\vec{i}-\frac{\partial q}{\partial x}\vec{j}\right) \tag{2}$$

Such a two-dimensional vector, $\vec{c}$, is equivalent to the earlier defined P-vector on z levels[6]. The necessary condition for the existence of the vector $\vec{c}$ is

$$\nabla q \neq 0 \tag{3}$$

At any point on isopycnal surface, the vector $\vec{c}=(c_x,c_y)$ indicates the tangential direction of

the trajectory and therefore, is parallel to the absolute velocity vector,

$$\vec{V} = \gamma(x, y, \rho)\ \vec{c}\,, \tag{4}$$

Where the absolute value of γ is the speed, $|\gamma| = \left|\vec{V}\right|$. Applying the thermal wind relation to any two different isopycnal surfaces ρ_k and ρ_m, a set of algebraic equations for determining the parameter γ is obtained:

$$\begin{aligned} \gamma^{(k)} c_x^{(k)} - \gamma^{(m)} c_x^{(m)} &= \Delta u_{km} \\ \gamma^{(k)} c_y^{(k)} - \gamma^{(m)} c_y^{(m)} &= \Delta v_{km}\,, \end{aligned} \tag{5}$$

Which are two linear algebraic equations for $\gamma^{(k)}$ and $\gamma^{(m)}$. Here $\gamma^{(i)} = \gamma\left(x, y, \rho_i\right)$, and

$$\left(\Delta u_{km}, \Delta v_{km}\right) = \frac{1}{f} \int_{\rho_m}^{\rho_k} \frac{1}{\rho^2} \left(\frac{\partial p}{\partial y}, -\frac{\partial p}{\partial x} \right) dp\,. \tag{6}$$

The velocity inversion can be divided into two steps: (i) determination of the unit vector $\vec{c}$, and (ii) determination of γ. There is detail information in references [4] and [5] about calculations.

3. RESULT ANALYSES

3.1 Eastward transport of STCC

The monthly total and layered eastward volume transport of STCC has been calculated along 139.5° E from 18° to 26° N (Fig. 1). Fig. 1a shows the monthly sum of the eastward transports in the water column above σ_θ = 27.0, excluding the eastward transports in the layers deeper than 27.0. It is obvious that there exists a remarkable seasonal variability in the total transport. It is the strongest in summer with a maximum of 8.7 Sv in August, weaker in spring with a value of 1.8 Sv in April. The very weak eastward transports in January, February and March are just corresponding to the eastward meandering of the current or to a flank of a local eddy, and it could not really represent the eastward transport. The monthly transports of STCC in four layers are calculated. The four layers are as follows, （1） the first layer: 22.3 $\leqslant\sigma_\theta\leqslant$24.0;（2）the second layer: 24.0$\leqslant\sigma_\theta\leqslant$25.0; （3）the third layer: 25.0$\leqslant\sigma_\theta\leqslant$26.0; （4）the fourth layer: 26.0$\leqslant\sigma_\theta\leqslant$27.0. The eastward transport in the fourth layer is almost zero. Fig. 1b shows the eastward transport in three layers. It can be clearly seen that the eastward transport is mainly in the second layer. STCC has a maximum transport of 5.1 Sv at the second layer in August, taking 59% in the total transport. Both the total transport and the layered one of STCC remarkably increase from May to November due to the branch of the Kuroshio Countercurrent merging

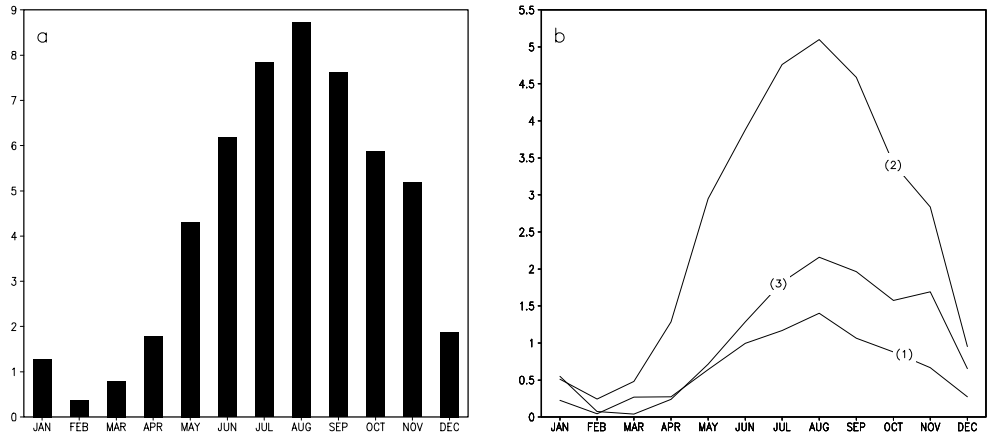

Fig. 1. Monthly total and layered eastward volume transports of STCC along 139.5° E (unit: Sv).
a. total; b. layered: (1) $22.3 \leqslant \sigma_\theta \leqslant 24.0$, (2) $24.0 \leqslant \sigma_\theta \leqslant 25.0$, (3) $25.0 \leqslant \sigma_\theta \leqslant 26.0$

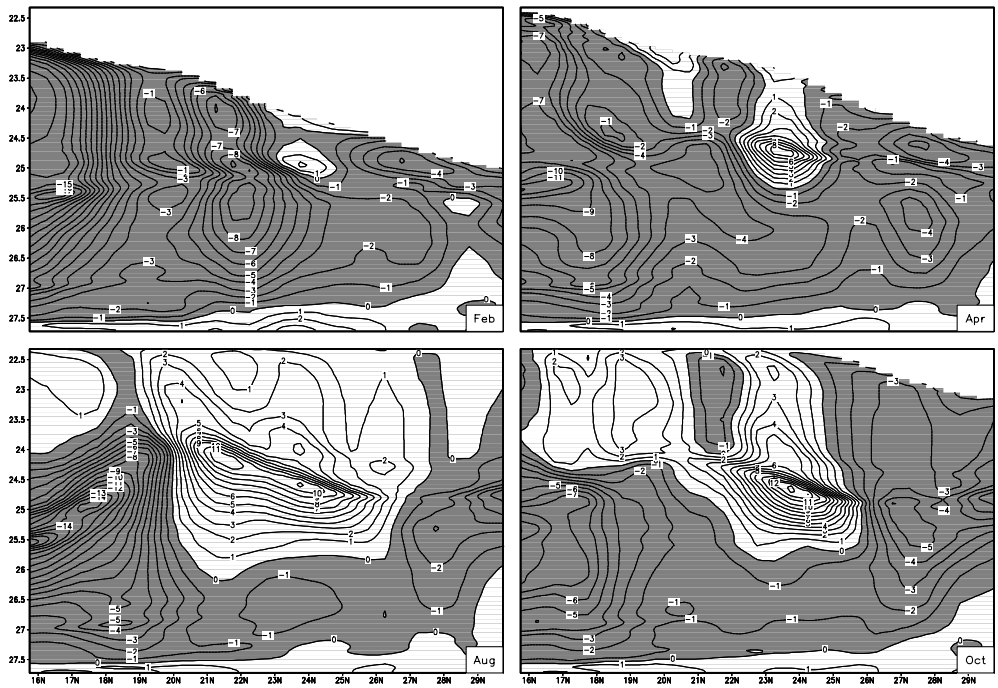

Fig. 2. East-west absolute velocity along 139.5° E for Feb., Apr., Aug., and Oct. Here, the contour intervals are 1 cm s^{-1}, and positive value represents eastward flow.

3.2 Vertical structure of STCC

The meridional sections of zonal current along 139.5° E for typical four months which represent four seasons in Fig. 2. Here, the positive value represents the eastward velocity. On the layer with a maximum velocity, the contour of 1 cm s^{-1} is taken to be as a limit for the width of STCC. We also define the contour of 1 cm s^{-1} as the deepest layer on which STCC exists. It is evident that a much weaker eastward current at

about 25.0 σ_θ and near 24.0° N is corresponding to a eastward detour of the Kuroshio Countercurrent in February. No STCC crosses 139.5° E in this month. In April, STCC has a core at 24.7 σ_θ and near 23.5° N with narrower width from 22.5° N to 24.5° N and with a maximum speed over 8 cm s^{-1}. The layers existing STCC are not deeper than 25.1 σ_θ. In August, the core of the main STCC lies at 24.2 σ_θ and near 21.5° N. STCC has the widest width between 20° N and 26.5° N with the largest speed over 11 cm s^{-1}. The deepest layer existing STCC is shallower than 25.8 σ_θ. The banded current structure on upper layers is clearly in October. The core of STCC situates at 24.6 σ_θ and near 23.5° N. The path of STCC is at 21° ~ 25° N with maximum speed larger than 13 cm s^{-1}. The layers existing STCC are not deeper than 25.6 σ_θ.

3.3 Horizontal distribution of STCC

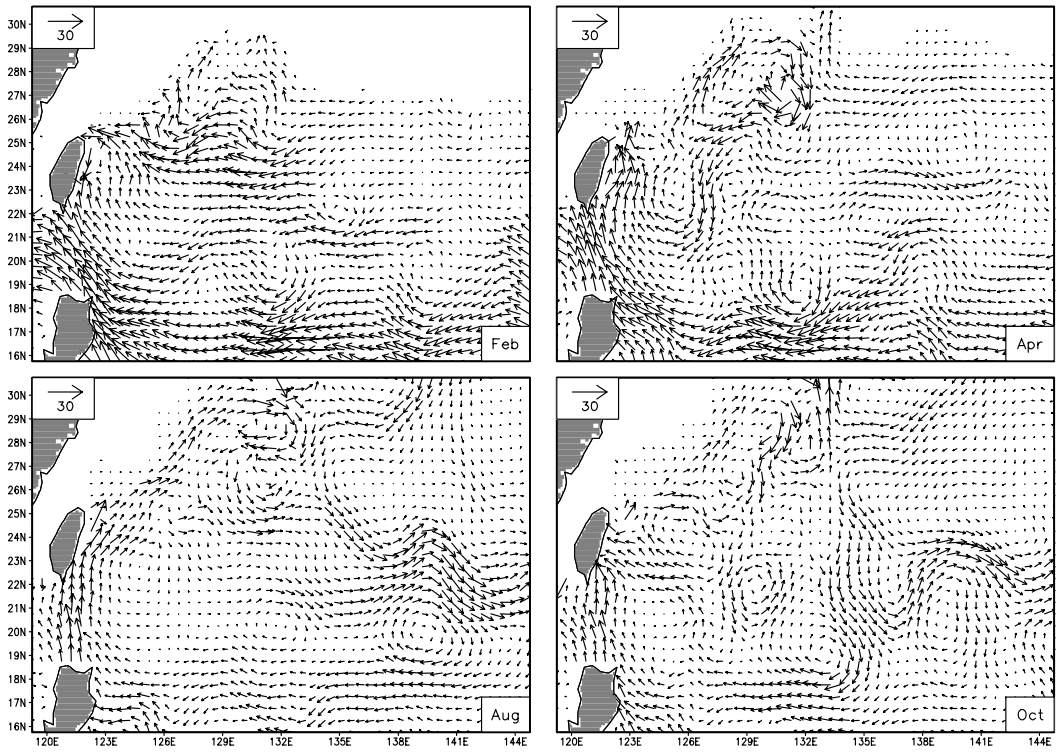

Fig. 3. Absolute velocity vectors on σ_θ = 24.6 for February, April, August and October

Fig. 3 shows the current vector distribution on σ_θ = 24.6 for February, April, August and October. The southern edge of the blank space in figures indicates the winter sea-surface outcrop of 24.6 σ_θ. From Fig.3, it can be clearly seen that nearly all of the water movement is westward except for the partial curving of the North Equatorial Current in February. In April, a continuous eastward flow east of 128° E at 21° ~ 25° N is corresponding to STCC. In August, STCC originates from the region east of Taiwan Island at about 23° ~ 24° N, and continuously flows to the area east of 144° E. There are three eddies south of STCC whose centers are near 22.5° N, 125° E, 20° N, 132° E and 20° N, 139° E, respectively. These eddies have not only influence on the path of STCC, but also seem to provide STCC with water so as to make

STCC exhibiting an increasing status downstream. In the course of the Kuroshio Countercurrent flowing southwestward, some branches separate and flow southward or southeastward, and then merge into STCC finally, hence the velocity of STCC east of 136° E is even more stronger than those of NEC and the Kuroshio in the East China Sea. In October, the path of STCC has most remarkable meander, at about 133 ° ~ 141° E, the core of STCC leaps over three latitudes from south to north, which probably results from the pressure of two eddies. The centers of these two eddies situate near 19° N, 133° E and 20° N, 139° E. During this month, STCC mainly originates from the branch of the Kuroshio Countercurrent separating at about 26° N, 134° E.

4. SUMMARY AND DISCUSSION

（1）It is difficult to present the distribution of STCC by means of direct observed data. In this study, P–vector method reproduces STCC obviously. The location of STCC here is in good agreement with previous studies, but its flow status exhibits many differences.

（2） We have mainly analyzed STCC in the western North Pacific, which was not studied adequately so far owing to shortage of observed data. The distributions of STCC shown by this study are very complicated. The absence of STCC in February is food for thought, and needs to be further investigated.

（3） Studying STCC based only on the section distribution of zonal current was deficiency because the eastward flow at a section can not demonstrate the existence of a continuous eastward current, and also can not identify the existence of STCC. Sometimes the eastward flow along a section is only a manifestation of the flank of a local eddy or of the detour of a current.

ACKNOWLEDGES

R.F. Li and X.B. You were jointly supported by the National Nature Science Foundation of China (Grant No. 40076009), and by the grant of the Knowledge Innovation Program of the Chinese Academy of Sciences (approved # KZCX1-SW-01-16). P. C. Chu was supported by the Office of Naval Research and the Naval Oceanographic Office. Comments from anonymous reviewers were helpful to improve our manuscript.

REFERENCE

[1] Yoshida, K., and T. Kidokoro, A Subtropical Counter-Current in the North Pacific – An Eastward Flow near the Subtropical Convergence, *J. Oceanogr. Soc. Japan*, 1967, **23** (2): 88 ~ 91.

[2] Yoshida, K., and T. Kidokoro, A Subtropical Countercurrent (II) –- A prediction of eastward flows at lower subtropical latitudes, *J. Oceanogr. Soc. Japan*, 1967, **23** (5): 231 ~ 246.

[3] Teague, W. J., M. J. Carron, and P. J. Hogan, A comparison between the Generalized Digital Environmental Model and Levitus climatologies, *J. Geophys. Res.*, 1990, **95**: 7167 ~ 7183.

[4] Chu, P. C., P-vector spirals and determination of absolute velocities. *J. Oceanogr.*, 2000, **56**: 591 ~ 599.

[5] Chu, P. C., and R. F. Li, South China Sea Isopycnal—Surface Circulation, *J. Phys. Oceanogr.*, 2000, **30**: 2419 ~ 2438.

[6] Chu,P.C., P-vector method for determining absolute velocity from hydrographic data, *Marine Tech. Soc. J.*1995, **29** (2):3-14.

IDEALIZED SIMULATION OF OROGRAPHIC RAINFALL WITH A MESOSCALE ATMOSPHERIC MODEL

Assela Pathirana
United Nations University 53-70, Jingumae 5Chome, Shibuya-ku, Tokyo 150-8925, JAPAN

Tadashi YAMADA
Chuo University, 1-13-27, Kasuga, Bunkyo-ku, Tokyo 112-8551, JAPAN

ABSTRACT: The impact of different atmospheric and topographic conditions on the rainfall distribution around a single, infinitely long ridge is investigated. The main objective of the study was the understand the conditions that are responsible for commonly observed rainfall patterns like high rainfall yields on the side of the ridge facing the wind and rain-shadows on the lee side. A modified version of MM5, a non-hydrostatic model that is widely used for limited area atmospheric simulations for research and operational purposes, was used for this study. The effects of different mountain ridge dimensions, large-scale wind conditions and large-scale moisture profiles on the amount and distribution of orographic precipitation, were clarified. Ridge height has a positive correlation with the amount of rainfall generated while the ridge width did not show such a clear relationship. Slowing of wind speed resulted in the spreading of rainfall outwards from the mountain peak. Reduction of moisture caused a reduced rainfall yield. Most of the simulations produced highest rainfall amounts on the windward slopes. However, changing the topography, wind speed or moisture, a rain shadow condition could not be attained. The introduction of a reversal of the winds in the upper atmosphere as observed in Asian summer monsoon and many other large-scale atmospheric flows on the globe, created a rain shadow by confining the rainfall completely to the upstream of the ridge top.

1 INTRODUCTION

Interaction of large topographical features with a wind field has dramatic effect on the generation of rainfall. It is observed and widely accepted that a mountainous terrain generally receives more rainfall than than lowland in the same geographic region and as a result there is a positive correlation between elevation and average rainfall yield. Rainfall in the worlds most rainy climates are determined by the different atmospheric mechanisms that are critically dependent on the presence of mountainous areas, making the knowledge on orographic rainfall a much needed ingredient of strategic planning on sustainable use of water resources or on water related disaster mitigation. Water availability of worlds major rivers depend on the rainfall occurring on mountainous watersheds.

The physical relationships that govern the atmospheric dynamics and the other phenomena related to rainfall generation, like phase changes of water substance, have long been formulated with sufficient clarity. When a large number of different factors that govern the destiny of water in the atmosphere interact, the resulting conditions are generally complex that the only feasible approach of resolving the water budget in the atmosphere is the use of numerical solution methods. Modern numerical models with complete sets of dynamical equations can forecast atmospheric conditions in the short-term, given suitable initial/boundary conditions and are widely used for operational and research purposes. However, the real atmospheric conditions are generally complicated due to the simultaneous action of a number of influences like constant and often rapid change of winds, pressure patterns, moisture, etc. Therefore, numerical simulations under controlled conditions of an idealized environment can contribute to the understanding of the influence of each of the factors that influence the rainfall patterns.

The dynamical behavior of the airflow over a mountain is a problem that has been subjected to extensive theoretical investigation (see Smith[12] for a review) and more recently to a number of numerical studies involving both real and idealized settings[7][1]). Pathirana et al.[9] used version 2 of the MM5 model to investigate the formation of lee-waves and rotors associated with mountain flow. Those idealized studies have focused on the dynamics of dry air, without incorporating the phase change of water substance and the rainfall generation. The objective of the present research was to understand the effect of different topographic and atmospheric parameters on the rainfall due to the interaction of large-scale wind fields with a long uniform ridge profile. An effort was made to identify conditions under which the rainfall is mainly limited to the wind side of the ridge, causing rain-shadows in the leeward slopes. The following sections present the methodology, details about selected experiments, results and conclusions.

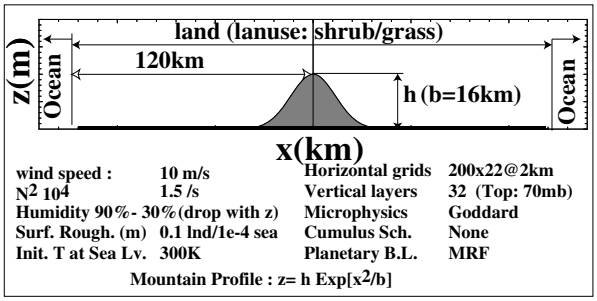

Fig. 1: Model configuration.

Table 1. Temperature (T) and moisture profiles (M.P.). Relative humidity given in percentages.

P (hPa)	1000	950	850	700	500	400	300	100
T (K)	300	298	293	284	269	259	246	200
M.P. I	95	95	95	95	80	75	50	30
M.P. II	95	95	85	80	75	40	30	30
M.P. III	90	85	70	60	50	40	30	30

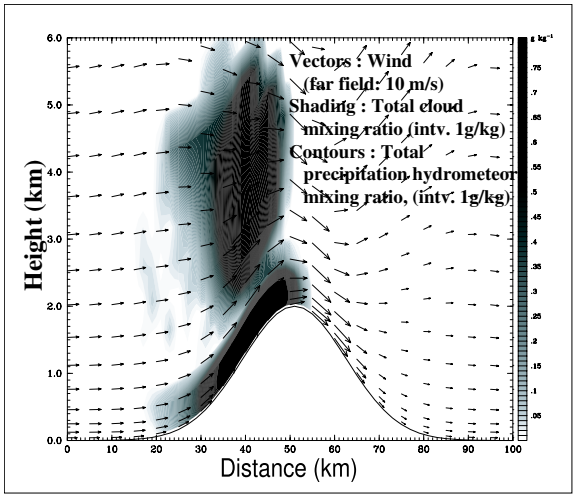

Fig. 2: Clouds after 10min of model start.

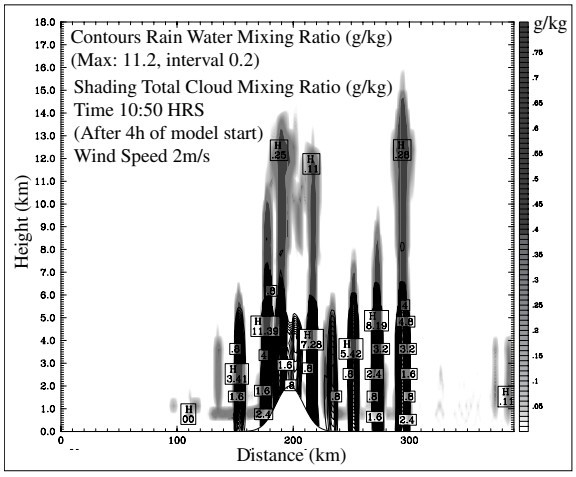

Fig. 3: Clouds and rainfall generated by convection triggered by mountain flow.

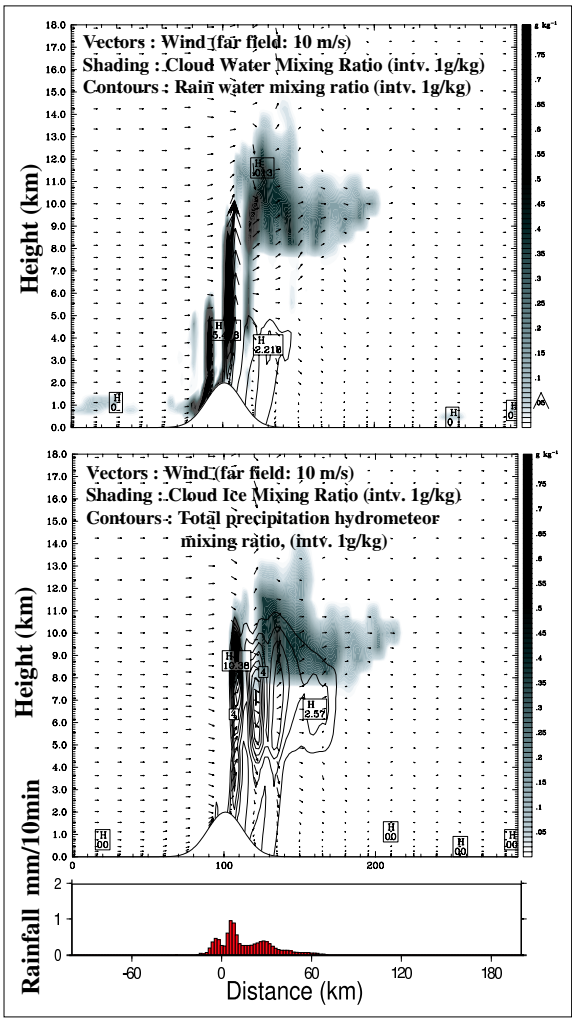

Fig. 4: Top and Middle: Development of clouds (200min after start). Bottom: Corresponding rainfall.

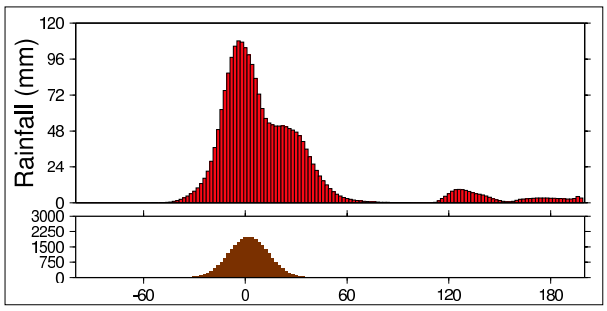

Fig. 5: Cumulative rainfall in 24h for the *control run*. The topography shown below.

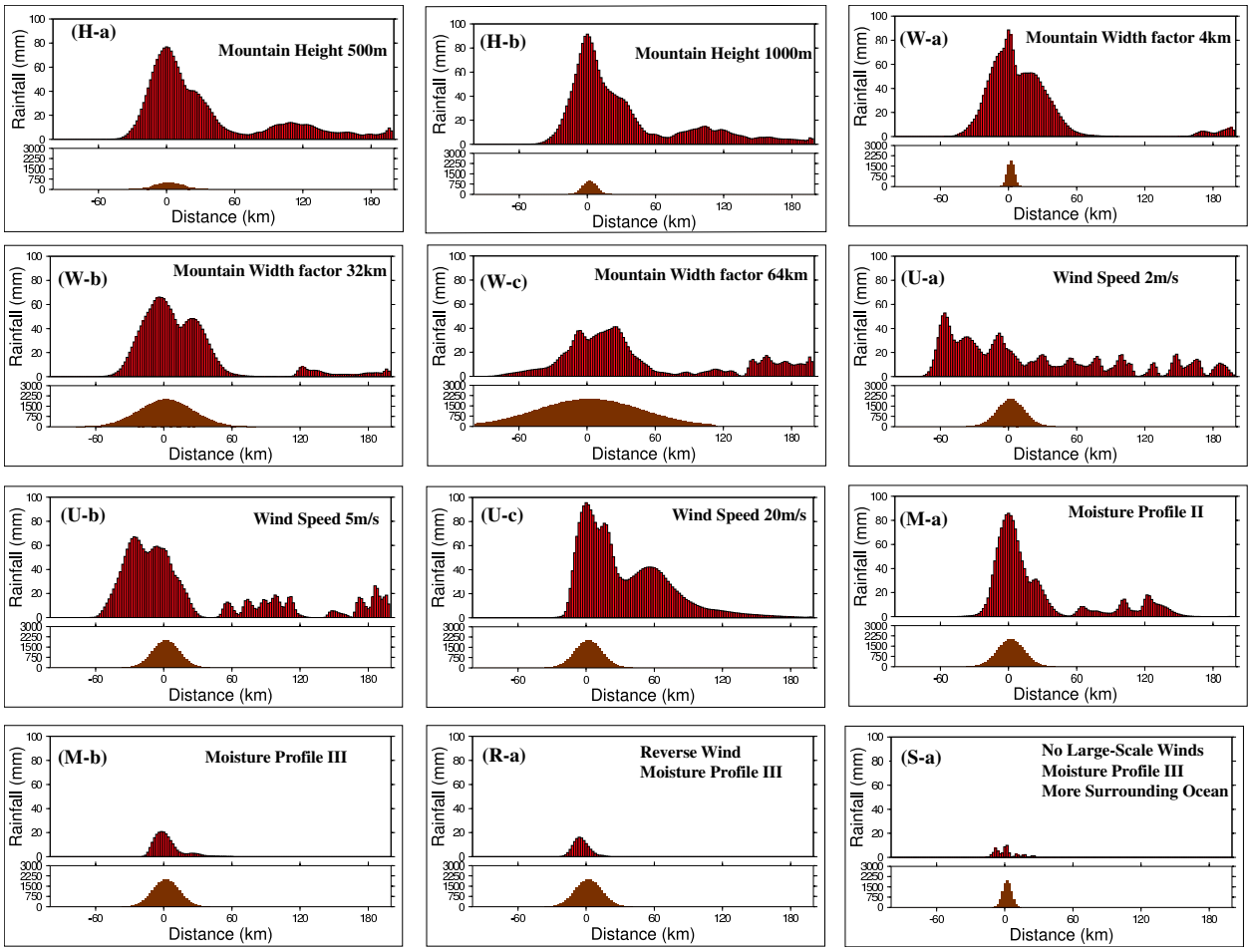

Fig. 6: Distribution of rainfall accumulated over 24h period. (H-a,b): Different ridge heights. (W-a,b,c): ridge width factors (b). (U-a,b,c): wind speeds. (M-a,b): Moisture profiles. (R-a): Presence of reverse flow in uppper atmosphere. (S-a) Case with no large-scale winds. (Corresponding ridge profile is shown below each plot.)

2 MODEL DESCRIPTION

The fifth generatoin Pennsylvania State University/National Center for Atmospheric Research mesoscale model, MM5[2][4]) solves a fully compressible, non-hydrostatic set of governing equations (for prognostic variables of velocity, pressure perturbation and temperature) on a terrain following (σ-z) coordinate system. The model requires the specification of the initial conditions all over the modeling domain and the lateral boundary conditions during the whole time period of model integration. Boundaries need to have specified horizontal winds, temperature, pressure and moisture conditions and optionally microphysical fields. In an operational scenario, the lateral boundary data are usually obtained from a global scale model results or analyses at some intermediate spatial scale, which ultimately depend on a global model. In historical studies lateral boundary conditions can be enhanced using observational data. Performing idealized simulations is not a standard usage of the modeling system and therefore a number of additional modifications of the prepossessing programs are needed before the model can be used for the purpose similar to the one of the present research. However, there are a number of distinct advantages in using MM5 as the basis for an idealized study. The model has been in operational and research use worldwide for more than a decade, resulting in a well-tested numerical system. The model source is freely available for use. Further, due to the model's ability to perform simulations based on real observational data and large-scale model outputs with relative ease, it is feasible to extend the ideal simulations to those using real data in future work, without switching models.

The available pre-processor programs of MM5 model sets up the model grid including surface topography using standard geographical datasets like GTOPO-30 of United States Gegraphical Survey. Further, they produce initial and lateral forcings using standard three dimensional pressure level datasets (first-guess fields) together with surface observations and soundings. In order to perform idealized simulations both these steps has to be altered to ingest idealized conditions. In the present research the former is achieved by producing fake GTOPO-30 like data cells with the desired idealized topography, for the standard preprocessor program to access. With

this approach the need to reprogram the model domain setup preprocessors is eliminated. To provide idealized forcing data, an alternative preprosessor program was created to provide the 3-d fields using the values for the horizontal wind velocities (w usually taken as zero), temperature and humidity (as relative humidity) at different pressure levels. Geopotential height is computed using the following relation derived from hydrostatic equation ($-dp = g\rho dz$, where ρ is density)

$$(Z_2 - Z_1) = \frac{R_d}{g_0} \frac{\log(P_1/P_2)(T_{v2} - T_{v1})}{\log(T_{v2}/T_{v1})}$$
for lower layers where $T_v \approx T_{v0} - \Gamma' Z$ and
$$(Z_2 - Z_1) = \frac{R_d}{g_0} T_v \log(P_1/P_2) \quad (1)$$
for isothermal layers

where R_d, g_0, Γ are dry gas constant, globally averaged gravitational acceleration and lapse rate of temperature with height, respectively. T_v is virtual temperature defined by

$$Tv = T\left[1 + 0.61\left(w_s \frac{RH}{100}\right)\right] \quad (2)$$

where w_s is the saturation mixing ratio of water and RH, relative humidity. A small adjustment based on horizontal velocity and latitudinal position, is applied to geopotential height to make the fields geostrophically balanced (details omitted).

3 SIMULATIONS

Fig. 1 and Table 1 shows the important model parameters. Due to the possibility of cloud formation at relatively high altitudes the model top was selected at 70mb (about 16km). Since the grid size is relatively small (2km), it is desirable to neglect the cumulus parameterization[10], leaving the explicit resolving of moisture as the only rainfall generation scheme. Goddard microphysics scheme[13], which has equations for vapor, cloud water, rain water, snow and graupel, was used for explicit resolving of moisture. The planetary boundary layer was represented by the Hong-Pan PBL scheme as implemented in NCEP MRF model[5] together with a single variable temperature soil slab above fixed-temperature substrate.

The atmospheric condition was set to reflect the typical conditions in the tropics. The temperature profile was selected such that the Brunt-väisälä frequency ($N^2 = g/T(\partial T/\partial z + g/C_p)$ for dry air, see Durran and Klemp[3] for definitions for moist air), is roughly a constant value of 1.5. The effects of clouds and diurnal cycle in atmospheric radiation were considered. Sea level temperature was set at 300K. Computation was started at 0600h (local time, in the morning) and the effect of solar heating was considered. The model was integrated at 6s time-steps and each run was continued for a full 24h cycle, producing output at every 10min.

In order to understand the effects of various topographic and atmospheric factors a number of simulations were done by changing the model parameters. The first model run (hereafter referred to as the *control run*) was conducted using a mountain with H =2000m and b =16m. The wind condition was set at 10m/s, constant with elevation. The moisture profile was such that the lower layers are nearly-saturated (RH >90%) and then dropping to a value less than 30% above 450hPa level. Table 1 lists the temperature and moisture profiles (M.P. I in the table) used. In the following sections the effects of changing Mountain height, Mountain width, Wind speed, Moisture profile and Wind profile, are discussed. In each of these experiments only the relevant parameter was changed while keeping others equal to those of control run.

4 RESULTS

Several minutes after the model initialization, the clouds first start to appear above the wind-side slope of the mountain. These clouds are of very low altitude (only several hundred meters above mountain surface). Fig. 2 shows the cloud structure after 10min of model start. The low-level cloud's base is at the level of the surface, so that this type of clouds may appear as fog to an observer on the mountain top. This type of clouds, due to their appearance as a wall to an observer on the lee-side, are known as a *Fohn-wall*. These are generally nonprecipitating clouds due to their lower elevation. However, low-elevation clouds can sometimes precipitate by working together with clouds aloft that are capable of providing large precipitation particles (Seeder-Feeder mechanism[6]). Though the simulation have generated a high-elevation cloud system aloft, there is no precipitation formed at this time.

During the next several 10min periods, the clouds develop rapidly in height aided by convective break-up due to the combined effect of topography and land-heating. These dense clouds with sharp outlines that develop vertically in the form of rising mounds (Cumulus) later develop in to precipitating clouds referred to

as *Cumulonimbus* under favorable conditions. Cumulonimbus is often characterized by the development of an *anvil* – the top part of the cloud that develops rapidly in the direction of wind (Fig. 4). It was observed that when the topography is higher, this growth takes place faster (within 2h in 2000m whereas 500m takes about 4h). As indicated by fig. 4-middle, the anvil is often made of ice crystals. A significant amount of rainfall starts to appear only after this cloud escalation and anvil development. The rain starts near the peak and then spreads towards the lee-side slope as the clouds spread that way. The precipitation starts often as snow or ice, but later transformed in to liquid rain as it descends to warmer lower levels of the atmosphere. However, some of the precipitation never reaches the surface (e.g. about 150km downstream of the ridge-peak) and gets re-evaporated during the decent through the atmosphere. This process in known as *virga*[8]. In the control run, the convective development occurs mostly on the slopes of the mountains. However, at lower speeds, the convective breakup occurs in the surrounding slopes as well (Fig.3).

After solving the model for a 24h period, the rainfall amount accumulated over that period was plotted. Fig. 5 is the distribution of this rainfall along a longitudinal cross section, for the *control run*. Fig. 6 shows the same for a number of cases with different model parameters.

There are some features of accumulated rainfall that are common to all the simulations performed: The general tendency is that the plains that are further away from the mountain gets relatively less rainfall compared with the slopes. However, non of the cases had the rainfall maxima at the peak of the ridge, but at a point some distance upstream of the peak. This is in agreement with rainfall patterns of some monsoon climates[14]. All the cases using moisture profiles I and II (Table 1) show a significant rainfall amount falling on lee-side plains, in addition to the rain on windward slope and ridge-top.

The mountain height has a positive correlation with the rainfall: Rainfall peak over the mountain as well as the total rainfall amount (results not shown) increased with ridge height. However, the rainfall amount on the downstream was not significantly affected. The increase of the width of the mountain leads to a decrease of ridge-top rainfall and an increase of rain on lee-side. This is contradictory to some of the accepted patterns of orographic rainfall. For example Smith[11] has stated that wider mountains cause lee-side rain shadows.

The results show a remarkable effect of wind speed on rainfall distribution: For low velocities the rainfall peak can occur more than 50km upwind from the crest. The overall rainfall pattern shows a distinct waviness, suggesting the possibility of mountain wave action. However, while all the cases generated gravity waves due to the ridge, they are of untrapped nature progressing nearly vertical above the ridge. The examination of the cloud structure (fig. 3) indicated that the rainfall at lower velocities are driven mainly by deep convection triggered due to the flow modification by the mountain as discussed by Houze[6]. Cases with higher large-scale wind velocities had most of the convective activities around the peak. However, the rainfall was not restricted only to the wind side of the mountain slope. The reason for the second (often smaller) rainfall peak at the lee-side may be the convection triggered by the interaction of the moist sea-breeze, warmed up over the land with drier and (relatively) cooler downslope wind.

The effect of reducing moisture causes reduction of peak over the mountain top. However, when the moisture profile is reduced to that of M.P. III (Table 1), the air becomes critically depleted of vapor by the upslope-condensation and other upwind-slope procesees, so that the convective rainfall on the lee-side becomes very much restricted (fig. 6M-b).

The actual wind profile of the summer monsoon, for example in Indian Ocean, is very much different from the constant wind fields used in the preceding analyses. Due to the action of the tropical easterly jet in the upper troposphere, the wind velocities gradually drop from a maximum near surface to a negative flow above a 6-7km height. Fig. 6R-a shows the results of a simulation with wind reversal above 6km height. The rainfall peak has moved further upwind compared with case M-b and there is almost no lee side rainfall. This pattern is quite in agreement with what is happening in some monsoon climates, e.g. Sri Lanka: The summer monsoon enters the island from west and passes through the central mountains, causing heavy rainfall on the western slopes, while the eastern slopes and plains remain dry during the season.

Finally, fig. 6S-a shows the results of a simulation with no large-scale wind field. (It should be noted that this particular simulation was done in a nested grid setup with about 400km of ocean on either side of the land, in order to have sufficient water space for sea-breeze to develop in the numerical domain.) Due to the differential heating of Ocean and land, the convergence of wind occurs over the mountain, causing small amounts of rainfall on and around the mountain.

5 CONCLUSIONS

A number of idealized simulations of the atmosphere surrounding a single mountain ridge was done, with changing different model parameters. Many features that are observed in orographic systems like Fohn wall, development of cumulus and cumulonimbus clouds, virga process and anvil formation were reproduced at different stages of simulations. Most of the simulations agree with the common observations of increase of accumulated rainfall with altitude, relatively larger rainfall amounts on upwind slopes compared with downwind slopes and the

occurrence of rainfall maxima on some distance upwind of the mountain peak. However, the exact distribution of rainfall is remarkably different among simulations with differing parameters. Effects of upslope-condensation, convection and convergence of sea-breeze above the mountain ridge dominated in different scenarios. However, the net accumulated rainfall of many simulations were contributed by more than one of these parameters.

None of the simulations with different ridge elevation, width, wind speed or moisture did not cause complete dryness on the lee-side. However, by the introduction of reversal of the wind field at the upper troposphere as it happens with many large-scale circulations in the globe, conditions of rain shadow was attained. This result suggests that the prevailant rainfall patterns around mountains in the path of large-scale floor, namely high rainfall on upstream slopes and virtually no rain on the downstream of the peak, are critically defendant on the occurrence of wind reversal in the upper atmosphere.

Acknowledgments: This work has been funded by a grant from the Japan Society for Promotion of Science.

REFERENCES

[1] J. D. Doyle and D. R. Durran. The dynamics of mountain-wave-induced rotors. *Journal of Atmospheric Science*, 59:186–201, 2001.

[2] J. Dudhia. A non-hydrostatic version of the Penn State-NCAR mesoscale model: validation tests and simulation of an atlantic cyclone and cold front. *Monthly Weather Review*, 121:1493–1513, 1993.

[3] D. R. Durran and J. B. Klemp. On the effects of moisture on the brunt-väisälä frequency. *Journal of Atmospheric Science*, 39:2152–2158, 1982.

[4] Georg Grell, Jimy Dudhia, and David Stauffer. A description of the fifth-generation penn state/ncar mesoscale model (mm5). Technical Report NCAR/TN-398+STR, National Center for Atmospheric Research, 1996.

[5] S. Y. Hong and H. L. Pan. Nonlocal boundary layer vertical diffusion in a midium-range forecast model. *Monthly Weather Review*, 124:2322–2339, 1996.

[6] R. A. Jr. Houze. *Cloud Dynamics*, chapter Orographic Clouds, pages 502–538. Academic Press, 1993.

[7] L. B. Nance and D.R. Durran. A modeling study of nonstation-ary trapped mountain lee waves, part i: Mean flow variability. *Journal of Atmospheric Science*, 54:2275–2291, 1997.

[8] World Meteorological Organization, editor. *International Cloud Atlas*. World Meteorological, June 1977.

[9] Assela Pathirana, Masafumi Yamaguchi, and Tadashi Yamada. Idealized simulation of airflow over a mountain ridge using a mesoscale atmospheric model. *Annual Journal of Hydraulic Engineering, JSCE*, 47:31–36, 2003.

[10] R. Pilke. *Mesoscale Meteorological Modeling*. Academic Press, San Diego, California, 2 edition, 2002.

[11] R. B. Smith. The influence of mountains of the atmosphere. *Advances in Geophysics*, 21:87–230, 1979.

[12] R.B. Smith. Hydrostatic airflow over mountains. *Advances in Geophysics*, 31:1–41, 1989.

[13] W.K. Tao and J. Simpson. Goddard cumulus ensemble model. part i: Model description. *Terrestrial, Atmospheric and Oceanic Sciences*, 4:35–72, 1993.

[14] Lareef Zubair. A dynamical model for orographic rainfall in sri lanka. In *Proceedings of Asian Fluid Dynamics Congress*, volume 8, pages 864–867, Shenzen, China, December 1999.

WIND CLIMATOLOGIES FROM A MASS-CONSISTENT WIND MODEL FOR SRI LANKA

Lareef Zubair
International Research Institute for climate prediction, Palisades, New York, USA
and
Ajith Gunaratne
Iowa State University, Ames, Iowa, USA.

ABSTRACT: Wind measurements in Sri Lanka are sparse particularly in the hill country of Sri Lanka and interpolation of these observations provides unrealistic wind patterns in mountainous areas. Here we use a mass-consistent wind model that takes account of topography to compute monthly wind climatologies for Sri Lanka at a resolution of 6 km. The model predicts realistic wind fields and brings out the high wind speed at various gaps in the mountain ridges in Sri Lanka. Quantitative comparison with measurements at stations across Sri Lanka show that the predictions are reasonably realistic. Thus this technique provides detailed and useful wind climatologies that can be used for research, development and applications purposes.

1. Introduction

Approximate mesoscale wind fields are useful to study the wind energy potential, pollution transport, wind forces on buildings, effects on aviation, impact on crops and indeed meteorology. The ground based wind measurements in Sri Lanka are sparse and the upper air measurements are even more limited. Thus a technique to predict wind fields at different heights will be useful. One approach to obtain wind fields over complex terrain is the use of the mass consistent wind model [1].

In this approach, wind fields are spatially evolved for a given domain topography and surface features which are consistent with observations of upper air or surface winds. The evolution of the wind field takes place under the constraint that the wind field is consistent with the equation of conservation of mass - thus leading to the nomenclature of mass-consistent wind model.

While this approach does not explicitly account for the dynamical equations or thermodynamic equations, it has been shown that the wind fields obtained from it are comparable in accuracy to those based on more precise approaches [1]. However, sea breezes, mountain breezes and wind modification due to moist processes are neglected.

We have modified the ATHIN software developed by the National Observatory of Athens in Greece [2], which again was a derivative from the NOABL code developed by SAI, Inc. in 1979 for the United States Department of Energy. While the analysis has been completed for all months, the performance of this model in predicting the wind conditions in January in Sri Lanka is reported here.

2. The Mass Consistent Wind Model

To obtain mass-consistent solutions, the model minimizes the variance E of the difference between the trial wind velocity (u, v, w) and observed wind values (u^0, v^0, w^0) in a domain V. $\alpha=\alpha_1 / \alpha_2$ is the transmissivity coefficient and is a measure of the tendency of the flow over the mountain rather than around it.

$$E(u,v,w)=\int\{\alpha_1^2[(u-u^0)^2+(v-v^0)^2]+\alpha_2^2(w-w^0)\}dV \tag{1}$$

The Lagrange multiplier method is used to minimize the variance E subject to the constraint of the continuity equation as follows:

$$J(u,v,w,\lambda)=\int_{\Omega}\{\alpha_1^2[(u-u_0)^2+(v-v_0)^2]+\alpha_2^2(w-w_0)\}+\lambda(\frac{\partial u}{\partial x}+\frac{\partial v}{\partial y}+\frac{\partial w}{\partial z})dV \tag{2}$$

The Lagrange Multiplier which represents the physical perturbation velocity potential, α_1 and α_2 are the Gauss precision moduli., *x, y* are horizontal directions, *z* is the vertical direction. The following fundamental elliptic equation for λ is obtained from equation 2,

$$\frac{\partial^2 \lambda}{\partial x^2} + \frac{\partial^2 \lambda}{\partial y^2} + \left(\frac{\alpha_1}{\alpha_2}\right)^2 \frac{\partial^2 \lambda}{\partial z^2} = -2\alpha_1 \left(\frac{\partial u_0}{\partial x} + \frac{\partial v_0}{\partial y} + \frac{\partial w_0}{\partial z}\right) \tag{3}$$

The coefficient α_1^2 is the weight of the horizontal velocity component (*u, v*) and the coefficient α_2^2 is the weight of the vertical velocity component (*w*). The elliptic equation (equation 3) was solved numerically by using the finite difference method. This method has second order accuracy at all interior grid points. Thus above formation leads to a system of linear equations. To solve these equations numerically, the Gauss-Seidel Iteration and the Jacobi method were used.

Previously this computation has been largely been implemented for temperate locations with a resolution of 20 km or above. Our implementation of this procedure in a region of high topographic and land use variations along with the modest Coriolis forces near the equator in a monsoonal region requires detailed testing and tuning of the model so as to optimize the procedure. We also had to develop procedures for preparation of input parameters such as topography, surface roughness and surface and radiosonde wind data for the appropriate ingest for the model.

3. Description of Computation

Initially, the model was run with an artificial topography, which comprised a mountain with a Gaussian profile. The parameters, which gave realistic wind fields for this trial, were chosen for the actual tests.

Domain: The domain between $5^0$5' to 9^0 5' N and 79^0 4' to 82^0 0' E was selected for the computations. Its area was 474 km x 270 km and it is shown as the frame in Fig. 1.

Horizontal Resolution: The domain was divided into a grid of 45 x 79 with each box of size 6 km x 6 km.

Vertical Resolution: The height of the domain was chosen as 5 km. 50 levels with the lowest at a height of 15 m were used. Sigma coordinates were used with the inter-level spacing increasing in geometric progression from the surface [1].

Topography: The topography values were derived from contour maps produced by the Survey Department of Sri Lanka. These maps had contour intervals of 30 m (figure 1).

Surface Roughness: Surface roughness was allocated in proportion to the topography as described by Lalas [2]. This allocation is not entirely satisfactory and a refined map of surface roughness is necessary.

Transmisivity Coefficient: This coefficient controls the flow over and around the mountains. A value of 0.1414 was found to be optimal.

Geostrophic Wind: Geostrophic wind values were obtained from the radiosonde measurements at Colombo [3]. The average zonal wind speed at the 850 mb pressure height for January from 1984 to 1991 was 4.9 m/s and the meriodional wind speed was 6.4 m/s.

4. Results and Discussion

The model provides output of three-dimensional wind fields through out the domain. The predictions for wind speeds at the lowest (15 m) level were compared with a surface wind map constructed by Yoshino [4]. The model wind field compares well with the surface wind map in general. The model captures high wind reported at various mountain gaps in keeping with qualitative observations of wind speed in these mountain gaps area available [5].

The predictions for wind speeds were compared (table 1) with observations in the stations identified in Fig. 1. Overall, the model wind speeds are fractionally higher than the measurements as expected. Batticaloa, Nuwara Eliya and Mannar have realistic results. The model overestimates the wind speeds at stations in the lee of the mountain massif such as Colombo. The wind speeds at the coastal stations of

Jaffna, Puttalam and Hambantota are underestimated perhaps as the sea breeze has not been incorporated into the model.

Location	Observed wind speed (m/s)	Model predicted speed (m/s)
Colombo	2.5	3.3
Hambantota	6.1	3.5
Batticaloa	3.3	3.7
Trincomalee	5.2	3.9
Nuwara Eliya	3.4	4.0
Mannar	4.1	3.7
Jaffna	6.9	3.8
Puttalam	2.5	3.5

Table 1: The mean wind speeds at mid-day at meteorological stations for January measured at 15 *m* height [6] and the prediction of the model at a height of 30 m.

The model overestimates the wind speeds on the lee regions of the mountain massifs. Further comparisons of vertical profiles of wind where observations from balloon ascents are available in the South (Hambantota), North-West (Mannar/Puttalam) and East (Trincomalee) show that the profiles from the model are realistic in the lower half of the domain. The better accuracy in the lower half of the domain is to be expected given the uniform geostrophic wind velocity which is applied as a boundary conditions at a height of 5 km.

5. Conclusions

The mass-consistent wind model gives realistic surface wind maps providing detailed predictions for the wind climatology through out Sri Lanka. It has also provided wind fields at various heights that were not available before. The model predictions are suspect on the lee of high mountains and modifications are necessary to rectify this anomaly. The model reproduces high wind speeds reported from mountain passes. Estimates for the contribution of the sea and mountain breezes to the wind circulation are needed. The model has been tested during other months as well and the model performs better during months of strong winds [7, 8] such as during the South-West monsoon period.

REFERENCES

[1] Ratto, CF, An overview of mass consistent models, in Eds. Lalas, DP, and Ratto, CF, *Modelling of atmospheric flow fields*, World Scientific, Singapore, 1996.

[2] Lalas, DP, Introduction to ATHIN, in Eds. Lalas, DP, and Ratto CF*, Modelling of atmospheric flow fields*, World Scientific, Singapore, 1996.

[3] Nakagawa, K, Edagawa, H, Nandakumar, V, and Aoki, M., **Long-term hydro-meterolological data in Sri Lanka**, University of Tsukuba, Tsukuba, 1995.

[4] Yoshino. MM, Wind and its effects on air temperature, humidity and rainfall in Sri Lanka, *Climatological Notes*, 33, 181-190, 1983.

[5] Schweinfurth, U. and Domroes, M. (1974), Local Wind Phenomena in the Central Highlands of Ceylon, *Bonner Meteorol. Abhandl*. 17: 387-401.

[6] Somasekeram, T, Perera, LAG, Perera, MP, De Silva, BG, Karunanayake, MM, and Epitawatta, DS, *National Atlas of Sri Lanka*, Survey Department, Colombo, 1988.

[7] Zubair, L., Diurnal and Seasonal Variations in Surface Winds at Sita Eliya, Sri Lanka*, Theoretical and Applied Climatology*. 71 (1-2): 119-127, 2002.

[8] Zubair, L., Diurnal and seasonal variation of surface winds at Hambantota, *Journal of the National Science Council, Sri Lanka*, 25(3).235-245, 1998.

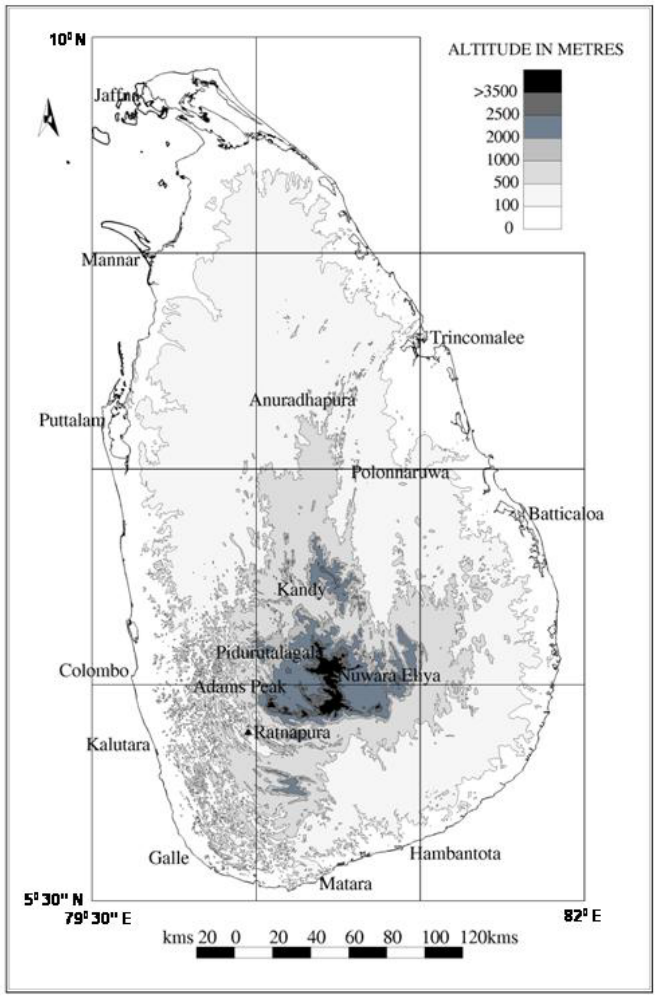

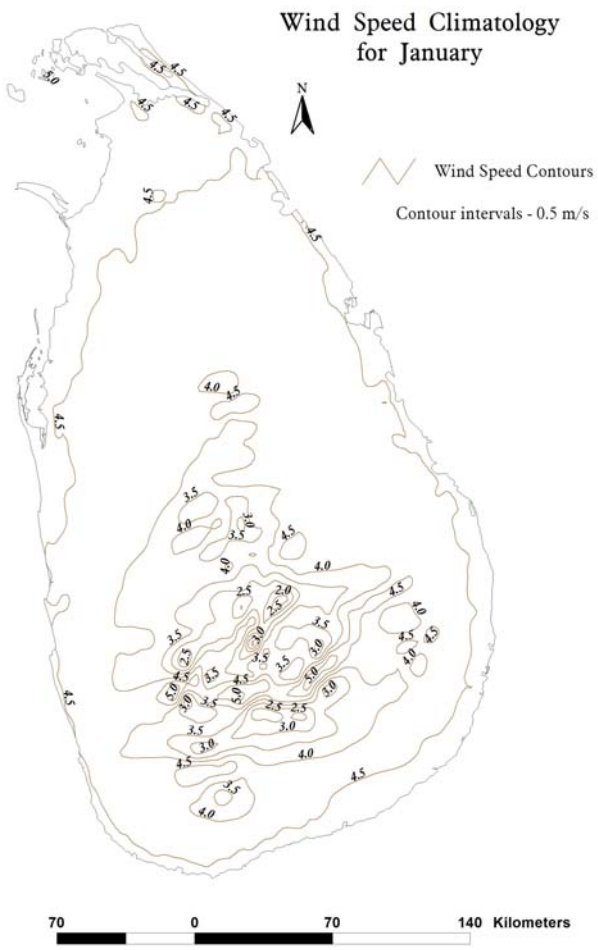

Figure 1(left): The topography of Sri Lanka.
Figure 2(right): The estimated wind speed climatology for January for Sri Lanka.

Proceedings of the Tenth Asian Congress of Fluid Mechanics
17-21 May 2004, Peradeniya, Sri Lanka

Wake structure behind a transversely spinning sphere at low Reynolds number.

M. Giacobello[1], A. Ooi[2], S. Balachandar[3] and M.S. Chong[2]

[1](Air Vehicles Division,
Defence Science and Technology Organisation, AUSTRALIA)

[2](Department of Mechanical and Manufacturing Engineering,
University of Melbourne, Victoria, 3010 AUSTRALIA)

[3](Department of Theoretical and Applied Mechanics,
University of Illinois at Urbana–Champaign, Urbana, IL, USA)

ABSTRACT: The flow past a sphere in uniform translation and forced transverse rotation is investigated for a Reynolds number, based on sphere diameter and freestream velocity, of 250. The numerical study identifies a number of wake transitions with increasing non–dimensional rotation speed w^* (the ratio of the surface speed to the freestream speed) of the sphere. For a stationary sphere the wake is steady. For $w^* = 0.1$ and 0.3 the wake is characterized by the shedding of vortex loops. Between $w^* = 0.5$ and 0.6, the wake shedding is suppressed. Vortex shedding is found to reoccur at $w^* = 0.8$.

1 INTRODUCTION

The motion of particles is of interest in a number of industrial applications which deal with particle laden flows. These include combustion processes and particulate transport processes. In general particles in these environments are subject to both translational and rotational velocities. The flow past a non–rotating sphere in uniform translation has been studied extensively and is reasonably well understood, while the problem of a rotating sphere in a uniform flow is not as well understood. Dimensional analysis shows that the flow past a rotating sphere can be characterized by two non-dimensional parameters, the Reynolds number $Re = U_\infty d/\nu$ and the non-dimensional angular velocity $\omega^* = \omega d/2U_\infty$. Here U_∞ is the free–stream velocity, d is the diameter of the sphere, w is the angular velocity of the sphere and ν is the kinematic viscosity. Analytical and experimental investigations into this problem have focused on relating Re and ω^* to the forces experienced by the sphere. Recently, the advances in computing power have allowed the problem to be tackled numerically. The more noteworthy of these is the work of Kim and Choi [6], who simulated a sphere spinning in the streamwise direction for $100 \leq Re \leq 300$ and $w^* \leq 1.0$. To the authors knowledge, the problem of a transversely spinning sphere in this Reynolds number range has not been investigated. In particular there are no details of the wake structure at any Re and w^*. This study aims to provide data at $Re = 250$. This allows direct comparison with the numerical study of Johnson and Patel [5], for the uniform flow past a non–rotating sphere. Simulations were conducted at discrete angular velocities of $w^* = 0.0, 0.1, 0.3, 0.5, 0.6$, and 0.8.

2 PROBLEM DEFINITION AND NUMERICAL FORMULATION

The time–dependent, incompressible Navier–Stokes equations are solved in a spherical domain using standard spherical polar coordinates. Figure 1 presents a schematic of the coordinate system and problem geometry. The freestream flow vector (U_∞) is along the positive z-axis and the sphere angular velocity vector (ω) is directed along the positive x-axis. The coordinate system comprises a radial direction, tangential and azimuthal direction (r, θ, ϕ), where

$$d/2 \leq r \leq D/2, \quad 0 \leq \theta \leq \pi, \quad 0 \leq \phi \leq 2\pi.$$

D is the outer diameter of the computational domain. The radial direction is discretized using Chebyshev polynomials and a collocation scheme. In the azimuthal direction, the dependent variables are intrinsically

periodic over 2π and a Fourier collocation method is employed in this direction. It is sufficient to define the tangential direction over π, while the dependent variable is periodic over 2π. Thus a Fourier collocation in this direction can only be used with some symmetry restrictions. The properties of an acceptable expansion are described by Boyd [2].

Temporal discretization is via a two–step time split method. This method is second order accurate in velocity and first order accurate in pressure. A detailed description of the numerical method used here is presented by Bagchi and Balachandar [1].

All simulations were initialized with a potential flow solution. For the non–rotating sphere, an artificial perturbation was needed to break the flow symmetry. This perturbation comprises a sinusoidal slip velocity at the sphere surface, with azimuthal mode 1 variation. For the spinning sphere simulations, the prescribed surface velocity boundary condition broke the flow symmetry and an artificial perturbation was not necessary.

Radially the domain extends to $d/D = 45$. A domain size sensitivity study showed that the force coefficients and the wake shedding Strouhal number ($St = fd/U_\infty$, where f is the shedding frequency) change by less than one percent by increasing the domain size to $d/D = 60$. The number of collocation points used in the radial, tangential and azimuthal direction is 121, 80 and 32, respectively. The adequacy of the grid resolution was also checked by ensuring adequate decay of the spectral expansion coefficients. Although the spectrum suggest the solutions are resolved, simulation at significantly higher resolution are currently being undertaken to insure grid independence.

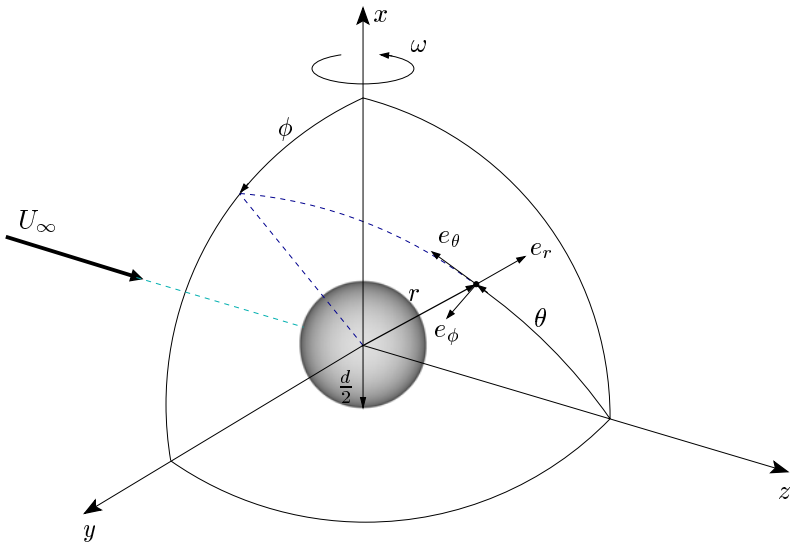

Figure 1: Problem geometry and coordinate system. The freestream flow is along the positive z-axis, while the sphere spins about the positive x-axis.

3 FLOW TOPOLOGY

Figure 2 presents a series of changes to the wake structure with increasing w^*. For cases where the flowfield is time dependent, the flow structure is shown at the instant when the magnitude of the lateral force is maximum. The focal structures in the wake are identified using the method of Chong *et al.* [3], by plotting an iso–surface of discriminant (D_A) in regions of the flow which experience stable focus/stretching. Preliminary experiments with the methods of Jeong and Hussain [4] and Zhou *et al.* [8] showed that for this problem, all three identification methods highlight the important structures in the wake. For a non–rotating sphere, the wake is steady and is characterized by two stream-wise vorticity tails, known as a 'double thread' wake. This structure has been observed both numerically and experimentally and is described in

some detail by [5]. For $w^* = 0.1$, the wake has undergone a bifurcation to an unsteady regime, characterized by the periodic shedding of so–called hairpin vortices at a single shedding frequency. This unsteady wake structure is similar to that observed for a stationary sphere above the Hopf bifurcation ($Re > 212$). At $w^* = 0.3$ the hairpin structures appear to be shed at a closer interval. The wake structures also appear to have a higher swirl strength, presumably due to the greater vorticity generated at the sphere surface as w^* is increased. Increasing the rotation to $w^* = 0.5$ suppresses the wake shedding. The steady wake now comprises two elongated focal threads. The wake structure at $w^* = 0.6$ is topologically similar to that at $w^* = 0.5$. A subtle difference is a higher wake deflection in the negative y-direction, consistent with the classical magnus effect. Increasing the rotation speed to $w^* = 0.8$ results in a further transition to a second vortex shedding regime. In this case the wake structures appear in closer succession, indicating a higher shedding St. Over the complete range of w^* studied, symmetry is maintained about the (y, z)–plane, as is evident from the (x, z) –projections shown in figure 2. This series of transitions from an unsteady, to steady, to unsteady flow again, is analogous to that observed by Mittal [7] for a spinning cylinder. However, in the case of a cylinder vortex suppression occurs at a significantly higher spin rate.

4 TIME AVERAGED PRESSURE AND VORTICITY FIELD

Time averaged pressure coefficient contours are shown in figure (3). Here pressure coefficient is defined as $C_P = (P - P_\infty)/(1/2\rho U_\infty^2)$, where ρ and P_∞ are the density and the freestream pressure, respectively. Contours range from -1.4 to 1.0 in increments of 0.08, with dashed lines used to indicate negative values. Flooded contours are used to identify pressure coefficient in the range -0.2 to -0.28. For $w^* = 0.0$ the pressure distribution is in close agreement with that found by [5]. The low pressure wake is asymmetric, with a low pressure lobe on the upper side of the sphere. The introduction of sphere rotation appears to smooth or equalize the pressure over the lee–side of the sphere. In particular, it is evident that the flooded regions coalesce to form a smooth band in the near wake for $w^* \geq 0.3$. This smoothing of the leeside pressure field appears to coincide with the suppression of vortex shedding seen in the topology field. As w^* is increased there is the appearance and progressive elongation of a low pressure stream–wise tail. This is caused by the focal stream-wise wake structures generating a centrifugal acceleration along their length. Increasing w^* also decreases the pressure over the upper hemisphere ($y > 0$) and it is expected that this will lead to an increased pressure induced lift force.

Figure (4) presents the time–averaged x–vorticity field in the (y, z)–plane. Contours range from -5.0 to 5.0 in increments of 0.25. For $w^* = 0.0$, the positive vorticity shed from the upper hemisphere is of greater, but of comparable magnitude, to the negative vorticity shed from the lower hemisphere. The line of flow separation can be identified by a change of sign in vorticity at the surface. The introduction of sphere rotation decreases the relative surface–to–freestream velocity on the upper hemisphere and increases it on the lower hemisphere. The result is that the negative vorticity produced on the upper hemisphere is weakened and becomes increasingly deflected in the negative y–direction. For $w^* \geq 0.3$ the x–vorticity produced by the sphere rotation is sufficiently large to inhibit the sign change in surface vorticity seen in the lower hemisphere at $w^* = 0.0$ and 0.1. There is also a progressive thinning of the negative vorticity layer shed from the lower hemisphere. This suggests that a shear layer instability may be the cause of the second transition to vortex shedding seen in the topology field at $w^* = 0.8$.

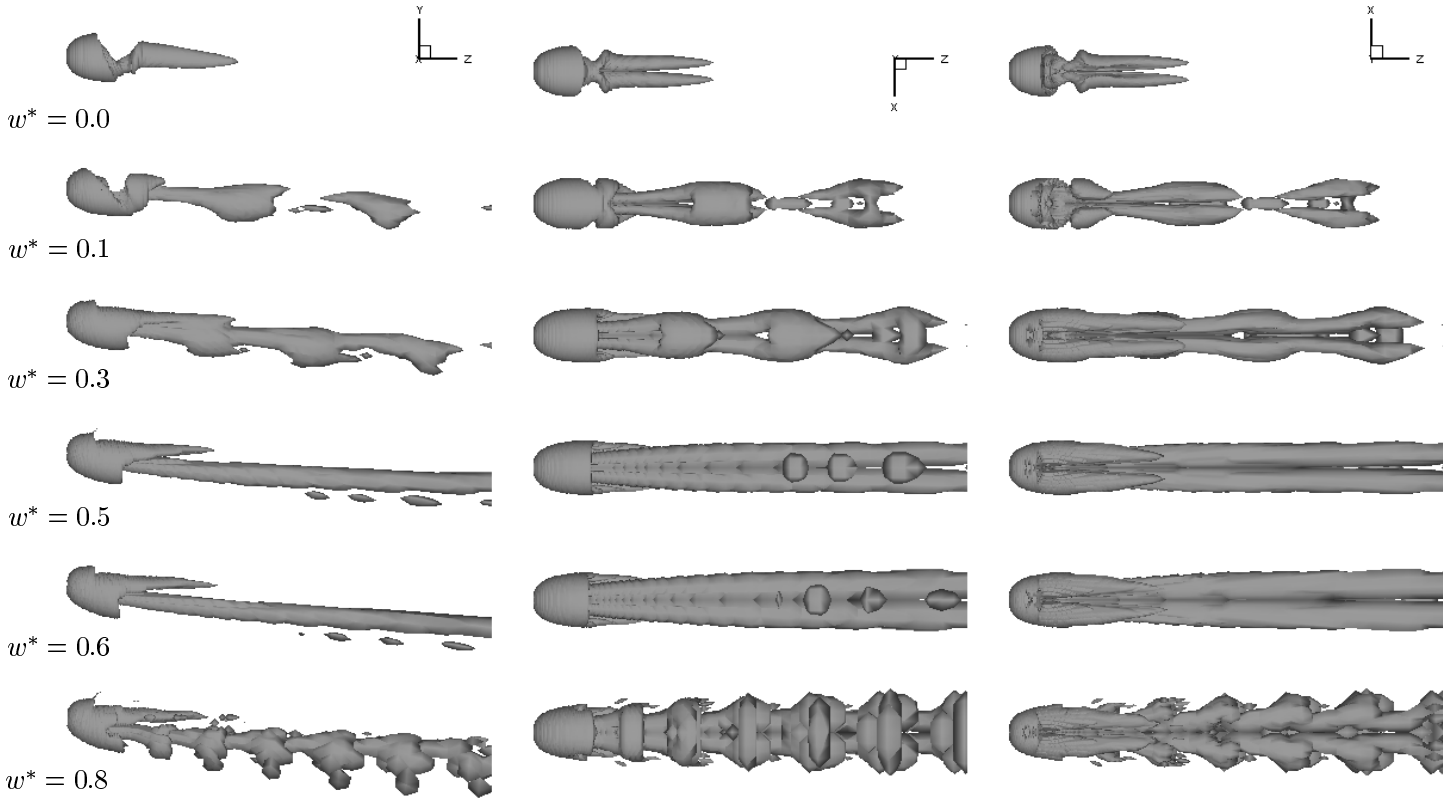

Figure 2: Wake structures at $Re = 250$. Stable focus/stretching structures are plotted for an isosurfaces of discriminant $D_A = 1e^{-7}$.

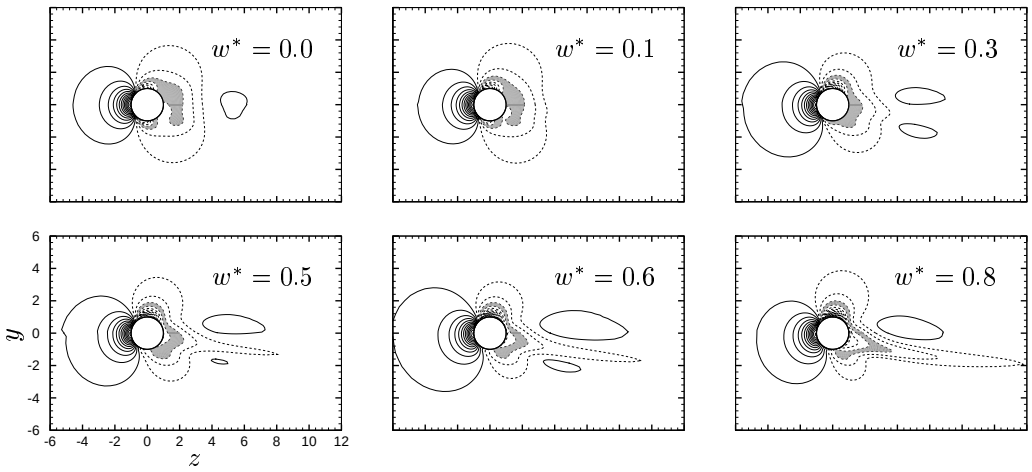

Figure 3: Pressure coefficient contours on the (y, z)–plane for $Re = 250$. Sphere rotation is about the positive x–axis. Contours range from -1.4 to 1.0 in increments of 0.08. Negative contours are indicated by dashed lines. Flooded regions are used to identify pressure coefficient in the range -0.28 to -0.2.

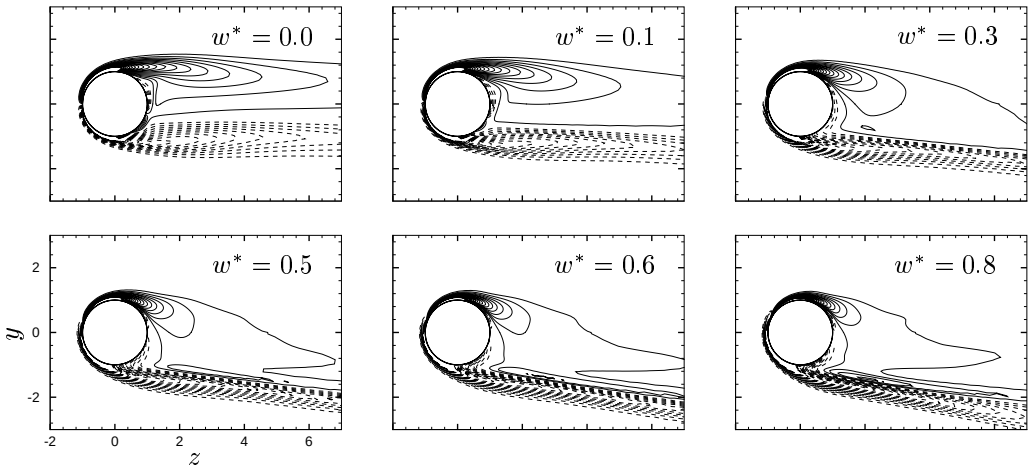

Figure 4: x–vorticity contours on the (y, z)–plane for $Re = 250$. Sphere rotation is about the positive x–axis. Contours range from -5.0 to 5.0 in increments of 0.25. Negative contours are indicated by dashed lines.

5 CONCLUSIONS

The flow past a sphere, rotating in the transverse direction has been studied using a direct numerical simulation for $Re = 250$ and $0.0 < w^* < 0.8$. For $w^* = 0.0$, the wake is steady and characterized by a double-thread wake structure. The introduction of sphere rotation results in a bifurcation to a vortex shedding regime, with the wake comprising a series of interconnected vortex loops. In the range $w^* = 0.3$ to 0.6 vortex shedding is suppressed and the wake comprises two steady stream–wise focal structures. The pressure field indicates that vortex suppression is accompanied by a smoothing of the pressure field over the leeside of the sphere. For $w^* > 0.6$ vortex shedding re–occurs. In this case the vortex loops appear in closer succession. The time averaged vorticity field suggests that a shear layer instability may be responsible for this transition. Simulations at higher spatial resolution are currently being undertaken in order to confirm the findings reported here.

ACKNOWLEDGMENTS

The authors would like to acknowledge the Australian Partnership for Advance Computing (APAC) and the Victorian Partnership for Advance Computing (VPAC) for providing the necessary computing resources. The authors would also like to acknowledge P. Bagchi for supplying the code used in this work.

REFERENCES

[1] Bagchi P and Balachandar S. "Steady planar straining flow past a rigid sphere at moderate reynolds number". *J. Fluid Mech.*, 2002. **466**, 365–407.

[2] Boyd JP. *Chebyshev and Fourier Spectral Methods*. Springer–Verlag, New–York, 1989.

[3] Chong MS, Perry AE and Cantwell BJ. "A general classification of three–dimensional flow fields". *Phys. Fluids A*, 1990. **2**(5), 765–777.

[4] Jeong J and Hussain F. "On the identification of a vortex". *J. Fluid Mech.*, 1995. **285**, 69–94.

[5] Johnson TA and Patel VC. "Flow past a sphere up to a reynolds number of 300". *J. Fluid Mech.*, 1999. **378**, 19–70.

[6] Kim D and Choi H. "Laminar flow past a sphere rotating in the streamwise direction". *J. Fluid Mech.*, 2002. **461**, 365–386.

[7] Mittal S and Kumar B. "Flow past a rotating cylinder". *J. Fluid Mech.*, 2003. **476**, 303–334.

[8] Zhou J, Adrian RJ, Balachandar S and Kendall TM. "Mechanisms for generating coherent packets of hairpin vortices in channel flow". *J. Fluid Mech.*, 1999. **387**, 353–396.

Proceedings of the Tenth Asian Congress of Fluid Mechanics
17-21 May 2004, Peradeniya, Sri Lanka

A STUDY OF SEPARATION CONTROL ON A THICK AIRFOIL BY VARYING MEMS PARAMETERS

Ajmal Baig and Salimuddin Zahir
Computer & IT Centre, National Engineering & Scientific Commission, Pakistan

Hossein Hamdani
Department of Aerospace, College of Aeronautical Engineering, NUST, Pakistan

ABSTRACT: In this research effort, boundary layer separation control over a thick airfoil, using Micro Electro Mechanical System (MEMS) actuator is studied. Separation imposes a considerable limitation on the operating characteristics of aircraft wings, leading to a significant degradation of their performance. A method of separation-control using alternating tangential blowing/suction with small speed at the slot-exit is studied by applying it to a NACA 0018 airfoil. Several MEMS parameters, such as frequency and velocity of actuator and position of slot, are varied to obtain the optimal solution. In the blowing phase, the boundary-layer velocity profiles downstream of the slot are made fuller and more separation-resistant. While in the suction phase, the boundary-layer velocity profiles upstream of the slot are made fuller and more separation resistant. This study is performed using a 2D grid generation code and a 2D Reynolds averaged Navier-Stokes equations (RANS) solver. Separation control over the thick airfoil (NACA 0018) is achieved in the post-stall region $(\alpha > 20)$ using single or multiple slots depending on the extent of separated flow and high L/D ratio is achieved. Applying flow control to attached flows yielded no significant gains.

1. INTRODUCTION

Boundary Layer separation entails great losses and limits the performance of many flow-related devices. Through separation control, flow pattern close to that given by inviscid flow theory can be obtained, leading to large lift and very small drag. The prevention of separation on airfoil and the generation of high lift are important aspects of boundary layer control. Much research has been done on this area[1~3]. It is known that if traditional methods of blowing or suction, such as using high-pressure air from the jet engine, were used for suppressing separation, very complex and large interior ducting would be needed. Due to the recent emergence of micro fabricated electro-mechanical systems (MEMS), the idea of alternating blowing/suction has originated. Among the various MEMS designs, zero-mass jet actuator [4] appears to be the most suitable for the above purpose. Zero-mass jet results from oscillating a diaphragm in an enclosed rigid cavity with a small orifice. The diaphragm is activated electro-statically, electro-magnetically or using piezoelectric material. The peak velocity and frequency are defining parameters of the zero-mass actuator. Recently, last author of this paper and Sun[5] reported their study on separation control on a thick airfoil with multiple slots with alternating tangential blowing/suction at small speeds. By alternating tangential blowing/suction meant that at each slot exit, the blowing/suction velocity was in the tangential direction of the airfoil surface and its magnitude varied periodically with a zero mean i.e.

$$V = V_a \sin(2\pi f t) \qquad (1)$$

Where V, V_a and f are the instantaneous velocity, peak velocity and frequency of blowing/suction respectively. It was seen that alternating tangential blowing/suction was very effective in controlling the separation and high values of time-averaged force coefficients were obtained however there were oscillations in the value of force coefficients due to alternating suction and blowing. The extent of variation of force coefficient during a cycle was found to be dependent on V_a and f. However it was found that when V_a is large enough to suppress separation (V_a 1) and frequency is large enough (f 1), then the global flow field did not vary much and the variation in force coefficients was also reduced.

2. COMPUTATIONAL METHOD

Governing equations are 2D-compressible, Reynolds-averaged Navier-Stokes equations. The equations are expressed in strong conservation form. They are well documented in literature [6] and will not be repeated here. The perfect gas law, Sutherland's viscosity formula, a constant Prandtl number and an algebraic eddy viscosity model for turbulence are used with the governing equation.

The governing equations are solved using the implicit, approximate factorization algorithm of Beam and Warming[7]. The scheme is formulated using three-point-backward implicit time differencing and second-order finite difference approximation for all spatial derivatives. Constant coefficient fourth-order explicit and second-order implicit spectral damping is added to damp high frequency oscillations and enhance stability behavior[7].

The Baldwin-Lomax two-layer eddy viscosity model[8] was chosen in the present flow simulations based on its previous successes in calculating flows on airfoils without separation[9]. At the inflow boundary, the velocity components and temperature are specified as free stream conditions while the pressure is extrapolated from the interior. At the outflow boundary, the pressure is set equal to the free-stream static pressure and the velocity and temperature are extrapolated from the interior. Along the grid cut-line, periodic boundary conditions were enforced. On the airfoil surface, adiabatic, impermeable wall and no-slip boundary conditions were applied, and the pressure on the boundary is obtained through the normal component of the momentum equation.

In the present calculations, the interaction between the flow of blowing/suction at a slot-exit and the surrounding fluid is simulated using a time-dependent boundary condition at the slot-exit. A special Poisson Solver based on the method developed by Thomas[10] with modifications incorporated by Liu *et al.*[11] is used for grid generation. The grid topology used in this work was an O-grid, with the grid cut line extending from the airfoil nose to the outer boundary. A portion of the grid for a NACA-0018 airfoil with a slot at 0.6c is shown in Fig. 1.

3. CODE VALIDATION AND SOLUTION ACCURACY EVALUATION

The code was validated with experimental data for a variety of cases, including flow around a NACA 0012 airfoil with angle of attack below stall angle of attack[12], unsteady flow around a NACA 0012 airfoil oscillating in pitch [13], unsteady flow around a circulation control airfoil with blowing jet [5].

4. GRID SELECTION

As with any numerical analysis, great care must be taken to insure the accuracy of the computed results. Grid sensitivity is considered and three grids were considered for grid test. Grid 1 is of 270x100 (270 points on the airfoil surface and 100 points in the direction normal to the surface). Grid 2 and grid 3 are of 400x150 and 600x225, respectively. It is seen that results of gird 2 and grid 3 are similar. On this basis, gird 2 is selected for further calculations.

5. RESULTS AND DISCUSSION

In the present research the blowing/suction velocity at slot exit is prescribed in a manner similar to that of reference [14] i. e.

$$V = V_a \sin(2\pi f t) \tag{2}$$

The angle of attack of airfoil is 25°, free stream Mach number is 0.1 and $Re/m = 10^6$. For comparison at these free stream conditions, a calculation was performed for the uncontrolled case (i.e. without slot and $V_a = 0$). From Fig 2, it is seen that the flow is separated and flow separation initiates from about 60% chord location. The defining parameters, which are important while applying alternating tangential blowing/suction for separation control, are Peak Velocity V_a, frequency f and slot location on upper surface of airfoil. The effect of slot height is already studied [14].
Above-mentioned parameters are separately discussed in the following discussion.

5.1 Effect of V_a

In this part, the effect of varying peak velocity (V_a) of blowing/suction at slot-exit is studied. Three values of V_a are considered, $V_a = 1.5$, 2.5and 3.0, which correspond to peak Mach number of 0.15, 0.25 and 0.3 respectively for a free stream Mach number of 0.1. The frequency is set at 2.5, the slot height is equal to $0.004c$ and slot is placed at 0.6 chord location (approximate location of separation for uncontrolled case; refer Fig. 2). The case of $V_a = 3.0$ is chosen for detailed discussion. Fig. 3 shows the variation of force coefficients vs. t for the case of $V_a = 3.0$. It is seen that C_L and C_D vary with time periodically with the same time period as velocity. Fig. 4 shows the global pictures of flow at three time

instants, i.e. the instant of zero velocity between suction and blowing phases, maximum blowing and maximum suction respectively. The three time instants correspond respectively to the A, C and G points on the V vs. t curve in Fig. 3. It is seen that the global flow field almost does not vary with time. The time variation of the aerodynamic forces is due to the variation of the flow inside the upper-surface boundary layer (see the discussion below). Comparing the global flow field in Fig. 4 with that for the uncontrolled case (Fig. 2), it is clearly seen that without flow control massive separation occurs and with the flow control, separation is completely suppressed. Table1 shows the time average force coefficients for the three cases i.e., Va = 1.5, 2.5 and 3.0.

5.2 Effect of Frequency

In this section, effect of varying frequency of blowing/suction is studied while keeping all other parameters constant. Three values of f are considered, f = 1.5, 2.5 and 5.0 which correspond to frequency values of 121 Hz, 303 Hz and 606 Hz, respectively, for the given free stream conditions. The slot height and slot location are $0.004\ c$ and $0.6\ c$ respectively (same values as used in previous section). The peak velocity V_a is equal to 3.0, since at this value of V_a separation is completely suppressed. Table 2 shows the time average force coefficients for f = 1.5, 2.5 and 5.0.

It is seen that $\overline{C_L}$ and $\overline{C_D}$ are similar for the three cases, and Fig. 5 shows the global flow field at an instant for f = 1.5, 2.5 and 5.0, respectively. The global flow field for these three cases is similar and the separation is completely suppressed. Due the lower value of $\overline{C_D}$ for f = 2.5 compared with that of f = 5.0, in subsequent cases frequency is fixed as 2.5.

5.3 Effect of Slot Location

In this section, four different locations of slots are considered and they are at $0.4\ c$, $0.55\ c$, $0.6\ c$ and 0.75 c. V_a is set as 3.0, f is equal to 2.5 and slot height is equal to $0.004c$. The placement (or location) of slot is done after giving due consideration to the point of separation of the uncontrolled case (Fig. 2). Table 3 shows the force coefficients for the four cases. It is seen that the best results are obtained for slot location of $0.55c$. While slightly lower values of $\overline{C_L}$ and slightly higher values of $\overline{C_D}$ are obtained for slot location of 0.4c and 0.6c. It is interesting to note that at $0.75c$ slot location $\overline{C_L}$ decreases considerably.

Figure 6 shows the global flow field for slot location of $0.4\ c$, $0.55\ c$, $0.6\ c$ and $0.75\ c$, respectively. For slot location of $0.4\ c$, $0.55\ c$ and $0.6\ c$, the control is effective and separation is suppressed. However for $0.75\ c$ slot location, separation is not suppressed and control is not effective since the flow separates before $0.75\ c$ location (see Fig. 2). This means that the slot is placed in the region of reverse flow and thus effectiveness of control is significantly reduced. From the above discussion, it is seen that slot location is a very important parameter during alternating tangential blowing/suction for separation control. The separation is suppressed, if the control is applied close to the point of separation for the uncontrolled case.

Table 1: Effect of velocity

V_a	f	$\overline{C_L}$	$\overline{C_D}$
1.5	2.5	1.35	0.14
2.5	2.5	2.36	0.085
3.0	2.5	2.46	0.085

Table 2: Effect of frequency

Va	f	$\overline{C_L}$	$\overline{C_D}$
3.0	1.5	2.37	0.084
3.0	2.5	2.465	0.085
3.0	5.0	2.485	0.095

Table 3: Effect of slot location

Slot location	$\overline{C_L}$	$\overline{C_D}$
0.4 c	2.385	0.095
0.55 c	2.5	0.0787
0.6 c	2.465	0.085
0.75 c	1.4	0.15

6. CONCLUS IONS

Based on the results of this study, the following conclusions are made.

1. Using alternating blowing/suction, in the blowing phase, the boundary layer velocity profiles downstream of the slot are made fuller and in the suction phase, the boundary layer velocity profiles upstream of the slot are made fuller.
2. For NACA 0018 at $a = 25°$, the flow separation is suppressed for $V_a = 2.5$.
3. For NACA 0018 at $a = 25°$, change in frequency of blowing/suction did not affect the value of force coefficients (when V_a is large enough to suppress separation).
4. Control is more effective if it is applied near the point of separation an uncontrolled case.
5. Control is ineffective for attached flow.

REFERENCES

[1] Abbot, I. H. and Doenhoff, A. E, "Theory of Wing Section", Dover, New York, pp. 188-246, Chap. 8, 1959.

[2] Gad-el-Hak, M. and Bushnell, D. M., " Separation Control: Review", Journal of Fluid Engineering, Vol. 113, pp. 5-29, March 1991.

[3] Gad-el-Hak, M., "Control of low speed Airfoil Aerodynamics", AIAA Journal, Vol. 28, pp. 1537-1552, 1990.

[4] Rathnasingham, R. and Breuer, K. S., "Characteristics of Resonant Actuators for Flow Control", AIAA paper 96-0311, 1996.

[5] Sun, M. and Hossein Hamdani," Separation Control by Alternating Tangential Blowing/Suction at Multiple Slots", AIAA-2001-0297.

[6] Steger, J. L., "Implicit finite-difference simulation of flow about arbitrary two-dimensional geometries", AIAA Journal, Vol. 16, pp. 679-696, 1978.

[7] Beam, R. M. and Warming, R. P., "An Implicit factored scheme for the compressible Navier-Stokes equations", AIAA Journal, Vol. 16, pp. 393-402, 1978.

[8] Baldwin, B. and Lomax, H., "Thin-layer Approximation and Algebraic model for separated Turbulent flows", AIAA paper 78-257, 1978.

[9] Rizzeta, D. D. and Visbal, M. R., "Comparative Study of two Turbulence models for Airfoil Static and Dynamic stall", AIAA Journal, Vol. 31, pp. 784-786, 1993.

[10] Thomas, P. D., "Composite three-dimensional grids generated by elliptic systems", *AIAA Journal*, Vol. 20, 1982, pp. 1195-1202.

[11] Liu, J. C., Sun, M. and Wu, L. Y., "Navier-Stokes analysis of circulation control airfoil", *Acta Mechanica Sinica*, Vol. 11, 1995, pp. 137-143.

[12] Wang, C. Y. and Sun, M., "Separation Control on a Thick Airfoil with Multiple slots blowing at small speeds", Acta Mechanica.

[13] Sun, M. and Sheikh, S., "Dynamic Stall Suppression on an Oscillating Airfoil by Steady and Unsteady Tangential Blowing", *Aerospace Science and Technology, vol. 3, No. 6, 1999.*

[14] Hamdani H., Baig, A. and Zahir, S., "A Systematic Study of Separation Control by Varying Various Parameters During Alternating Tangential Blowing/Suction", 41st AIAA Aerospace Sciences Meeting and Exhibit, Reno, AIAA-2003-0422.

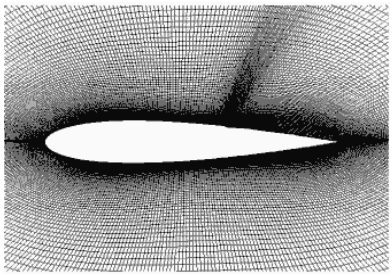

Fig. 1 Portion of grid for NACA 0018 airfoil with slot at 0.6c

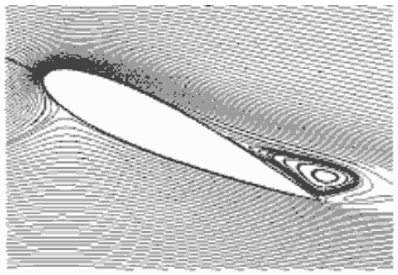

Fig. 2 Streamline plot for = 25° (Uncontrolled case and without slot)

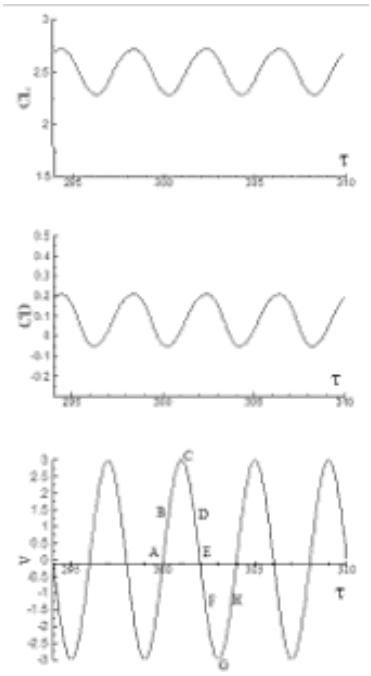

Fig. 3 Graph of C_L and C_D vs , V_a = 3.0, f = 2.5 and = 25°. Slot height = 0.004c and slot location = 0.6c

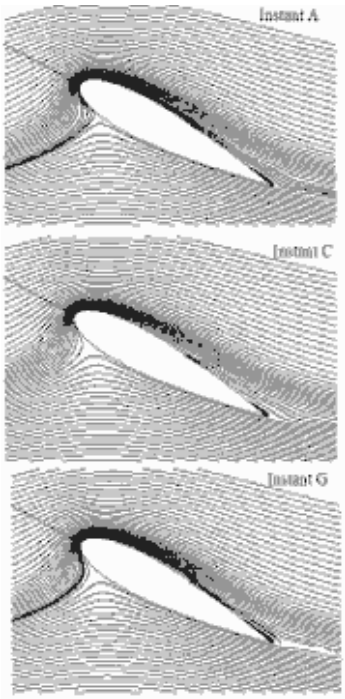

Fig. 4 Streamline plots at various instants. V_a = 3.0, f = 2.5, = 25°, Slot height = 0.004c and slot location = 0.6c.

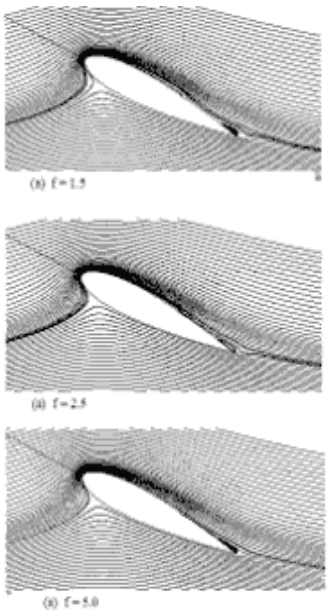

Fig. 5 Streamline plots for different f at particular instants. $V_a = 3.0$, $f = 2.5$, $= 25°$, Slot height = 0.004c and slot location = 0.6c.

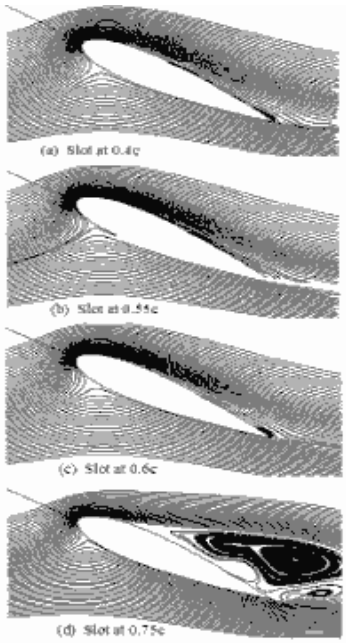

Fig. 6 Streamline plots comparison for different Slot locations. $V_a = 3.0$, $f = 2.5$, $= 25°$, Slot height = 0.004c and slot location = 0.6c.

Proceedings of the Tenth Asian Congress of Fluid Mechanics
17-21 May 2004, Peradeniya, Sri Lanka

Estimation of the Aerodynamic Forces for the Moveable Nozzles

S. Bilal H Bukhari , Ajmal Baig ,S. Zahir & M. A. Khan
CFD-Chapter, Computational, Modeling, Control & Simulation Society of Pakistan
www.ccsspak.org

ABSTRACT: A study has been made for the estimation of aerodynamic forces for the flexible convergent divergent, nozzle. The flow field parameters for a CD Nozzle were analyzed and validated earlier.[1] In this paper the thrust loss and lateral forces were estimated and compared with the experimental data available [2] at the different degrees of deflection of the flexible nozzle. The results obtained numerically were found to be in a good agreement with the experimental results. PAK-3D is used which is a Computational Fluid Dynamics (CFD) software based on Navier-Stokes Equations solver.

1. INTRODUCTION

Flexible nozzles are important to give an appropriate control force with the certain minimum thrust loss. The control force is due to the deflection of the divergent part from a typical location. The formation of the shock in the divergent part yields the difference in the pressure gradient between upper and the lower wall of the nozzle and thus providing the lateral force that is used as the control force. However the location of the pivot point remains the crucial issue for the optimum design point of view as the losses in the thrust may be significant as compared to the lateral force.

Control is very important for manoeuvre of flying bodies, for flying bodies, which propel in air or space without wing surfaces in general, move at the expense of thrust produced by the rate of change of momentum of the exhaust of the nozzle. In order to confine the moving body to the trajectory, control of some sort is used. The jet vanes are normally used in converging diverging nozzle to provide the manoeuvrability by redirecting the propulsive forces to alter the flight path of a vehicle flying at a certain speed. The jet vane placed in the downstream of the converging-diverging nozzle was analyzed and validated [3]. They deflect the exhaust flow, thus producing the required lateral forces that effectively pivot or roll the vehicle. The vane can be deflected to a certain degree so as to provide a required thrust vector angle.

2. GOVERNING EQUATIONS

A formulation of a set of partial differential equations obtained by the application of the general conservation laws (mass, momentum and energy) in an arbitrary control volume. The equations are given in conservative form with standard notations.

$$\frac{\partial U}{\partial t} + \nabla . F = 0 \qquad 1.1$$

$$U = \left[\rho \;\; \rho u \;\; \rho v \;\; \rho w \;\; e\right]^T$$

$$F = E\hat{e}_x + F\hat{e}_y + G\hat{e}_z$$

$$E=\begin{bmatrix}\rho u\\ \rho u^2+p+\tau_{xx}\\ \rho uv+\tau_{xy}\\ \rho uw+\tau_{xz}\\ (e+p+\tau_{xx})u+\tau_{xy}\upsilon+\tau_{xz}\omega+q_x\end{bmatrix}\qquad F=\begin{bmatrix}\rho\upsilon\\ \rho u\upsilon+\tau_{xy}\\ \rho\upsilon^2+p+\tau_{yy}\\ \rho\upsilon\omega+\tau_{yz}\\ \tau_{yx}\upsilon+(e+p+\tau_{yy})\upsilon+\tau_{yz}\omega+q_y\end{bmatrix}$$

$$G=\begin{bmatrix}\rho\omega\\ \rho u\omega+\tau_{zx}\\ \rho\upsilon\omega+\tau_{zy}\\ \rho\omega^2+p+\tau_{zz}\\ \tau_{zx}u+\tau_{zy}\upsilon+(e+p+\tau_{zz})\omega+q_z\end{bmatrix}$$

$$\tau_{xx}=-2\mu\frac{\partial u}{\partial x}-\lambda\nabla\cdot v\qquad \tau_{yy}=-2\mu\frac{\partial\upsilon}{\partial y}-\lambda\nabla\cdot v\qquad \tau_{zz}=-2\mu\frac{\partial\omega}{\partial z}-\lambda\nabla\cdot v$$

$$\tau_{xz}=\tau_{zx}=-\mu\left(\frac{\partial u}{\partial z}-\frac{\partial\omega}{\partial x}\right)\qquad \tau_{yx}=\tau_{xy}=-\mu\left(\frac{\partial u}{\partial y}-\frac{\partial\upsilon}{\partial x}\right)\qquad \tau_{yz}=\tau_{zy}=-\mu\left(\frac{\partial\upsilon}{\partial z}-\frac{\partial\omega}{\partial y}\right)$$

$$q=q_x\hat{e}_x+q_y\hat{e}_y+q_z\hat{e}_z=-k\nabla T$$

The following analytic relations provides partial derivatives in Cartesian coordinates with respect to the curvilinear coordinate system

$$\xi=\xi(x,y,z)\qquad \eta=\eta(x,y,z)\qquad \varsigma=\varsigma(x,y,z)$$

Thus equation 1.1 can be written in the following form,

$$\frac{\partial\overline{U}}{\partial t}+\frac{\partial\overline{E}}{\partial\xi}+\frac{\partial\overline{F}}{\partial\eta}+\frac{\partial\overline{G}}{\partial\varsigma}=0 \qquad 1.2$$

Where,

$$\overline{U}=U/J$$

$$\overline{E}j=E\xi_x+F\xi_y+G\xi_z$$

$$\overline{F}j=E\eta_x+F\eta_y+G\eta_z\qquad \overline{G}j=E\zeta_x+F\zeta_y+G\zeta_z$$

$$J=\frac{\partial(\xi,\eta,\zeta)}{\partial(x,y,z)}\begin{vmatrix}\xi_x & \xi_y & \xi_z\\ \eta_x & \eta_y & \eta_z\\ \zeta_x & \zeta_y & \zeta_z\end{vmatrix}$$

Where, J is the Jacobian of the transformation.

In PAK-3D [4], implicit Beam and Warming algorithm gives an inversion of scalar penta-diagonal matrices in each sweep, with time differencing by Euler backward differencing scheme and flux vector splitting for linearization.

3. GEOMETRY AND FLOW CONDITIONS

Geometry of the CD nozzle is shown in Fig. 1. The geometry and flow conditions are same as in [2] for validation purpose. The detail of the geometry is as follows

Length, L =0.02518m
Throat Diameter, Dt =0.011 m
Inlet Diameter, Di = 0.026m
Exit Diameter, De = 0.01919 m

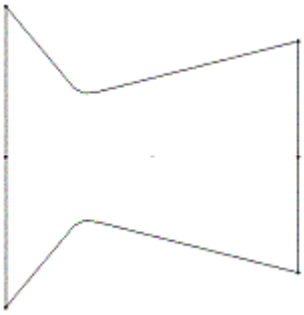

Fig. 1: 2D geometry of nozzle.

Flow conditions for the CD-Nozzle are reported as in [2], are as follows
Chamber pressure, P_c=9.0 MPa
Back pressure, P_b = 3.0 bar
Temperature, T=2200 K

4. GRID GENERATION AND BOUNDARY CONDITIONS

3-D simulation, single block was modelled with different grid sizes to access the grid independence study. 3-D Half Body was modelled to perform the calculations. Based on the grid independence study conducted in Ref. [1] the grid size 90 x 60 x 45 points, in the Block-1 containing the CD-Nozzle section The grids used for this study were generated by using PAKGRID [5].

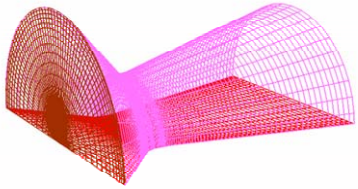

Fig.2: 3D Grid of CD-Nozzle.

In the present case, at the inlet, free stream conditions were fixed, while the condition of extrapolation was imposed at the exit of nozzle. For the nozzle wall, no-slip adiabatic condition was imposed. For 3-D symmetric plane symmetry plane condition was used and averaging was done about the nozzle's centre line.

5. RESULTS AND DISCUSSION

In the present study, effective lateral force was achieved by deflecting the divergent portion of the nozzle. Lateral force is due to the pressure difference on the wall of the nozzle. At zero degree deflection, the pressure distribution on the wall of the nozzle is uniform as shown in Fig. 3. As a result of uniform pressure distribution, there is no Lateral force. The Mach contours are also uniformly distributed for zero degree deflection as shown in Fig. 4. When the divergent portion of nozzle is deflected, the pressure distribution on the opposite planes of the wall is changed and, as a result, a lateral force is generated. The divergent portion of the nozzle is deflected at 2°, 4°, 6°, 8°and 10°, respectively. The pressure and Mach contours distribution for 8° deflections are shown in Fig. 5 and Fig. 6. For zero degree of deflection, the pressure curves overlap each other but as the deflection angle increases the curves overlap till throat section. After the throat section these pressure curves move away from each other as a result of increase of pressure difference on the opposite planes of wall. These pressure curves are drawn in Fig. 7. Normalized normal forces in the divergent section are calculated by integrating the pressure on the nozzle's wall. These normalized normal forces are drawn along the nozzle axis and is shown in the Fig. 8. With the increase in deflection the normal force increases as shown in the Fig. 8. The normal force integrated over the nozzle wall as a function of nozzle deflection angle is compared with experimental results and is found to be in a good agreement as shown in Fig. 9.

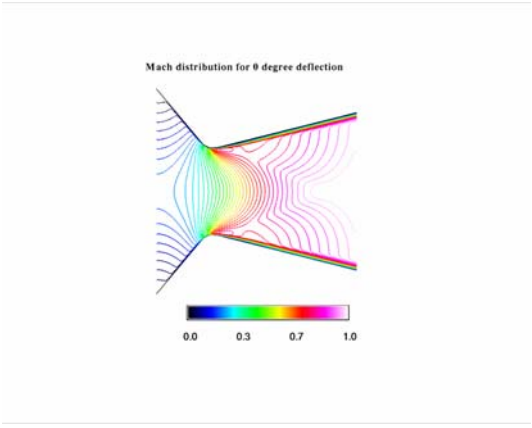

Fig. 3: Pressure Contour for 0° deflections along Nozzle's axis

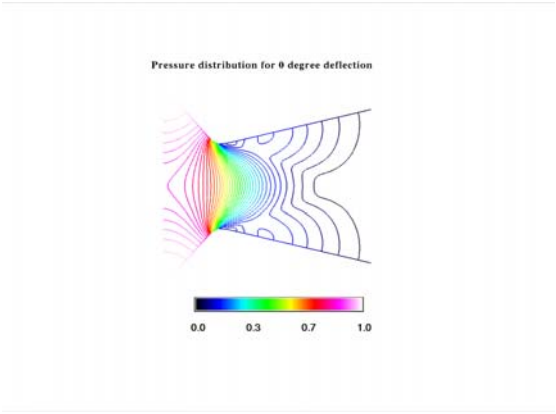

Fig. 4: ;Mach Contour for 0° deflections along Nozzle's axis

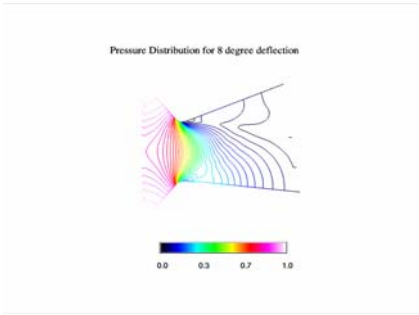

Fig. 5: Pressure Distribution for 8° deflections along Nozzle's axis

mkkkkkkkkkkkttttttt

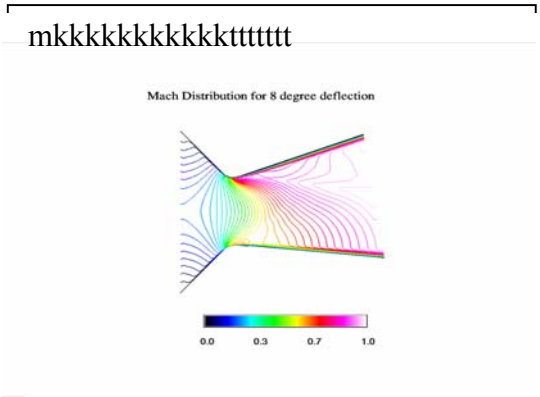

Fig. 6 Mach Distribution for 8° deflections along Nozzle's axis

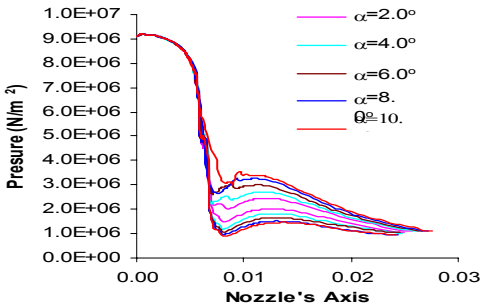

Fig. 7: Pressure Distribution along Nozzle's axis

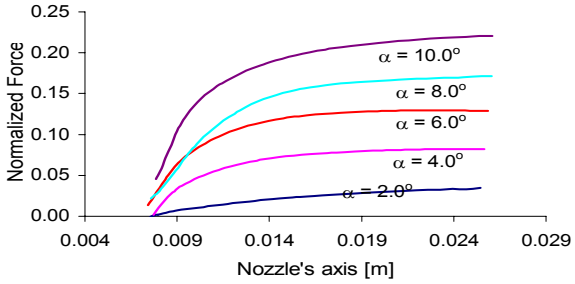

Fig. 8 : Normalized normal force vs nozzle's axis.

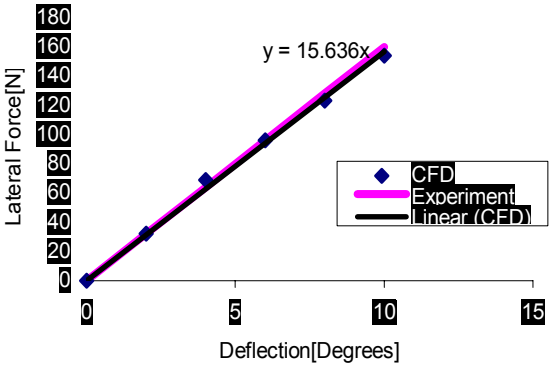

Fig. 9 Comparison of CFD and Experimental Results For Control Force

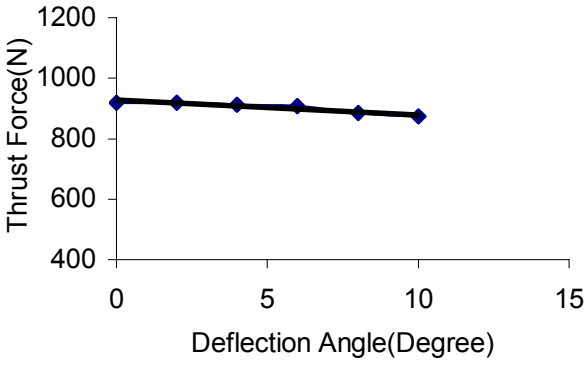

Fig. 10 Comparison of CFD and Experimental Results For Thrust Force

6. CONCLUSIONS

Lateral force would be achieved as a result of the pressure gradient on the nozzle wall.

Lateral force increases linearly with the deflection angle and is in a good agreement with the published experimental results [2].

The thrust losses as a function of deflection angle are in good agreement with the published experimental results [2].

REFERENCES

[1] S. Zahir, S. Bilal H.Bukhari & Mahmood A. Khan: A comparison of results of PAK-3D with the experimental results for an optimized Convergent Divergent Nozzle; CFD2002 Conference of the Computational Fluid Dynamic society of Canada.

[2] WANG Bao-shou, XU Sheng: Test Studies of Underwater Thrust Vector Control Performance. Journal of Ship Mechanics, Vol. 4 No.5 Oct. 2000.

[3] S. B. Bukhari, I. Jehan, S. Zahir: Solid Rocket Plume Analysis and its Applications, 9th Asian Congress on Fluid Mechanics Isfahan, Iran"

[4] User's Manual PAK-3D, Aerodynamics Division, ASAC, Pakistan, 1997.

[5] User's Guide PAKGRID, ASAC Pakistan, 1997.

Proceedings of the Tenth Asian Congress of Fluid Mechanics
17–21, May 2004, Peradeniya, Srilanka.

A MODEL FOR RELATING SPATIAL AND TEMPORAL CORRELATIONS OF TURBULENT FLOWS

Murali R. Cholemari & Jaywant H. Arakeri

Department of Mechanical Engineering, Indian Institute of Science,
Bangalore, India 560012

ABSTRACT: A model to relate the Eulerian spatial and temporal correlations of turbulent flows is presented. The model is for stationary and homogeneous flows. We implement the model for two point velocity correlations. We compare the model results with measurements of a quasi-steady turbulent flow with zero mean, which is homogeneous in one direction. The results are encouraging.

1. INTRODUCTION

The spatial and temporal correlations are important statistical parameters of a turbulent flow, allowing us to infer the spatial structure and energy distribution amongst various scales of turbulence. It has been difficult to measure spatial correlations experimentally, and spatial patterns are inferred from a single point temporal measurements by the 'frozen' turbulence hypothesis of Taylor.[9] This requires corrections, and these have been studied in detail (Fisher and Davies,[6] Lumley,[7] Clifford and Wyngaard[10]). All these analyses are in the spectral space. A series of experiments by Favre and co workers[3][4][5] give space time correlations. Recently the technique of PIV has enabled one to measure turbulent flows both spatially and temporally, making it possible to get both spatial and temporal correlations. It is interesting to ask whether we can infer one from the other and if so in what way. We give a model to simultaneously relate the Eulerian spatial and temporal correlations in stationary homogeneous turbulence. We implement the model for two point velocity correlations.

The related topic of the relation between the Lagrangian autocorrelation coefficient and the Eulerian velocity correlation is discussed in Saffman[8] and modeled in Baldwin and Mickelsen.[2]

2. MODEL

Consider homogeneous stationary turbulence with the velocity field in a plane (say (x, y)), given by $u(x, y, t)$ and $v(x, y, t)$. The mean velocity is zero; thus $\langle u \rangle = 0$ and $\langle v \rangle = 0$, where $\langle\ \rangle$ represents the mean. The spatial correlation, between two variables, with separation in the x direction, say, is given by,

$$\mathcal{C}^S_{\phi\psi}(r_x) = \frac{\langle \phi(x, y, t)\psi(x + r_x, y, t)\rangle}{\phi'\psi'} \tag{1}$$

where ϕ' and ψ' are the rms of ϕ and ψ, e.g.,

$$\phi' = \sqrt{\langle \phi^2 \rangle} \tag{2}$$

and r_x is the separation distance. Similarly the temporal correlation coefficient is,

$$\mathcal{C}^T_{\phi\psi}(\tau) = \frac{\langle \phi(x,y,t)\psi(x,y,t+\tau)\rangle}{\phi'\psi'} \tag{3}$$

where τ is the separation in time. For a flow that is homogeneous in all directions, and stationary the correlations will depend on the separation r_x or r_y or τ and are independent of the reference point (x, y, t). The correlation functions contain information on turbulence. At the simplest level, the correlation functions are used to obtain the integral scales and the Taylor microscale, but clearly, the correlations contain more information on turbulence.

To motivate the model, we briefly discuss the nature of correlations obtained in turbulence and why spatial and temporal correlations may be related.

Consider the longitudinal correlation $\mathcal{C}^S_{vv}(r_y)$ and the temporal correlation $\mathcal{C}^T_{vv}(\tau)$, schematically shown in figure 1. $\mathcal{C}^S_{vv}(0) = 1$ and the correlation reduces with increasing separation, finally becoming zero at large separation distances. Similarly $\mathcal{C}^T_{vv}(0) = 1$ and becomes zero at large separation times. One way to explain the reduction of correlation with increasing r_y or τ is as follows. The contribution of velocity at a certain spatial point (say, $y = 0$) and time (say $t = 0$) comes from *eddies* of various sizes. At a small distance δy away (at $\tau = 0$) the velocity will have the same contribution from the larger eddies, but not from the smaller ($\ell < \delta y$) eddies, and the correlation reduces to some extent. With increasing separation distance more and more eddies stop contributing to the correlation; at the larger separation distances, the correlation is only due to the larger eddies. Similarly, in case of temporal correlation, the first drop in correlation with time is due to the smallest eddies moving away from the reference point $y = 0$ and subsequent reductions in correlation occur as larger and larger eddies leave the reference point. Another way to look at the decorrelation with larger eddies is that they occur less frequently than the smaller eddies.

To look at this picture in a slightly different way, we note that the correlations, both spatial and temporal, are linked to the eddies in a similar way; and decorrelation occurs with increasing eddy size. In a stationary homogeneous turbulence, these eddies must occur with same probability at all points and over all times, and therefore it should be possible to relate the spatial and temporal correlations.

Our aim in this paper is to propose a model that relates the spatial and temporal two point velocity correlations, specifically using which it is possible to calculate one knowing the other. The model is in two parts, one part relating the temporal correlation to the spatial correlation, and the other for the reverse case. The essential idea is that one could define a sampled velocity field from the stationary homogeneous field using the correlations, which could be either stationary or homogeneous depending on whether the spatial or temporal correlation is used to define the sampling. Then, a spatial or temporal dependence respectively is brought about using the sampled velocity field, thus defining a new sampling and a spatial or temporal correlation, which would be the same as one would obtain directly with large data sets. The way one obtains the sample velocity field depends on the specific correlation considered.

2.1 Spatial from Temporal

Consider the two point spatial correlations of quantities ϕ and ψ in the direction x_i, $\mathcal{C}^S_{\phi\psi}(r_{x_i})$ and their temporal correlation $\mathcal{C}^T_{\phi\psi}(\tau)$. We would like to relate the two as,

$$\mathcal{C}^S_{\phi\psi}(\mathcal{S}(\tau)) = \mathcal{C}^T_{\phi\psi}(\tau) \tag{4}$$

where the *correlated displacement* $\mathcal{S}(\tau)$ is the displacement along the x_i of the spatial correlation function $\mathcal{C}^S_{\phi\psi}(r_{x_i})$, such that the correlation equals the temporal correlation at that time, $\mathcal{C}^T_{\phi\psi}(\tau)$. A *dispersion velocity* $u_d^{'T}$ effects the displacement $\mathcal{S}(\tau)$.

$$\mathcal{S}(\tau) = \int_0^\tau u_d^{'T}(t)dt \tag{5}$$

Further implementation requires the modeling of $u_d^{'T}$. We implement the model for the case of two point velocity correlations. Before we proceed further we note that in case of temporal velocity correlations, there are only one set of directions, those corresponding to the velocities. Thus one cannot get transverse spatial correlations from the temporal correlations, which require two sets of directions. One can obtain only the longitudinal spatial velocity correlations from temporal velocity correlations.

Consider $\mathcal{C}_{vv}^T(\tau)$ for example. We take,

$$(u_d^{'T}(\tau))^2 = u_s^{'2}\mathcal{C}_{\phi\psi}^T(\tau) = v'^2\mathcal{C}_{vv}^T(\tau); \tag{6}$$

where $u_s^{'2}$ is a scaling velocity that depends on the correlation considered. We take $u_s = v'$ for $\mathcal{C}_{vv}^T(\tau)$. The simplest model would have been to take $u_d^{'T} = v'$, but in that case the effect of the decorrelation of the smaller eddies with increasing τ is not modeled. This attennuation is modeled by $\mathcal{C}_{vv}^T(\tau)$. Thus the sampled rms field consists of the rms velocity (which is homogeneous and stationary) that is weighted by $\mathcal{C}_{vv}^T(\tau)$. The dispersion velocity is homogeneous, but depends on τ. The displacement $\mathcal{S}(\tau)$ brings the spatial dependence associated with timescale τ in the homogeneous temporal correlation. $\mathcal{S}(\tau)$ and the corresponding decorrelation give the spatial correlation $\mathcal{C}_{vv}^S(r_y)$ for large data sets. Thus equations (4), (5) and (6) together constitute the model.

2.2 Temporal from Spatial

Consider again a homogeneous, stationary turbulent flow and the temporal and spatial correlations of the quantities ϕ and ψ. We would like to relate the two as,

$$\mathcal{C}_{\phi\psi}^T(\tau(r_{x_i})) = \mathcal{C}_{\phi\psi}^S(r_{x_i}) \tag{7}$$

with $\tau(r_{x_i})$ being the *correlated time*.

$$\tau(r_{x_i}) = \int_0^x \frac{dr_x}{u_d'^S} \tag{8}$$

Further implementation requires the modeling of the dispersion velocity $u_d'^S$. We again consider two point velocity correlations. We note that we have two sets of directions available, corresponding to the co-ordinates and the velocities respectively and thus we have both transverse and longitudinal velocity correlations. The scaling velocity u_s' for the corelation of $u_i u_i$ is the rms u_i', irrespective of the direction, i.e., whether the transverse or longitudinal correlation is considered. Consider the transverse correlation $\mathcal{C}_{vv}^S(r_x)$. The dispersion velocity is a sampled velocity field in space, picking up only the part of the rms field which contributes to the spatial correlation from the stationary and homogeneous field. The dispersion velocity is given by,

$$(u_d^{'S}(r_x))^2 = v'^2\mathcal{C}_{vv}^S(r_x) \tag{9}$$

with the scaling velocity, $u_s' = v'$.

The time $\tau(r_x)$ brings in the temporal dependence associated with lengthscale r_x in the stationary spatial correlation. $\tau(r_x)$ and the associated decorrelation give the temporal correlation $\mathcal{C}_{vv}^T(\tau)$ for large data sets. Equations (7), (8) and (9) constitute the model.

3. DESCRIPTION OF THE FLOW

The data are from a buoyancy driven turbulent flow in a vertical pipe of 50mm diameter and a length of 0.6m. The flow is created and maintained by the density difference across the ends of the pipe. We use fresh water in the bottom tank and brine (typical initial density of 1%) in the top tank at the two ends of the pipe to create the initial density difference. The unstable configuration causes the flow to develop. There is no net flow as the fluids are incompresible. The fluids mix bringing down the density difference across the ends of the pipe and therefore the intensity of turbulence. However, this process is slow (about 2 hours) compared to the turbulent time scales and the flow can be considered quasi-steady for small intervals of a few minutes. Except near the ends of the pipe, the flow is homogeneous in the axial (y) direction, with a linear density gradient. The rms of velocity fluctuations are of the order of cm/s. The Rayleigh number based on the diameter is about 10^9. The integral scales of turbulence are of the order of the pipe diameter. The Taylor microscale Reynolds number is about 100. In the absence of the mean flow there are no mean shear stresses and therefore the turbulence is sustained by buoyancy alone, the shear production being absent. Also the walls of the pipe do not participate in production of turbulence, just containing the flow with kinematic wall blocking effects. The turbulence is found to be scaled by a mixing length represented by the pipe diameter. This has been supported by the integral length scales being comparable to the pipe diameter.

We use Planar Particle Image Velocimetry to obtain the turbulent velocity fields in the axial plane at the pipe mid-section. The velocity frames are one second apart. The data is for a total of twenty five minutes. Each velocity frame is of 29 by 31 velocity vectors, sampling an area of 50mm by 50mm of the flow. The axis of the pipe is vertical in the images. The details of the experiments are given in.[1]

The data consists of 5 sets each with duration of $54s$ of a stationary flow with a direction along which the flow is homogeneous. The two spatial directions are x and y. $\langle \quad \rangle_x$, $\langle \quad \rangle_y$ indicate spatial averages. $\langle \quad \rangle_N$, refers to the ensemble averaging over all of the 5 sets, for example,

$$\langle u(x,y,t) \rangle_N = \frac{1}{N} \sum_N u(x,y,t) \tag{10}$$

with t being the time within each of the N sets. For the data sets considered, $N = 5$, and further since the flow is stationary and homogeneous in y, we average over time or y. The results shown are for data along the axis of the pipe.

4. RESULTS

We give below typical results of the comparison. In all cases, the results of the model are shown by symbols. Figure 2 gives the spatial correlation calculated from the temporal correlation. As described in 2.1, equations (4)-(6), only longitudinal spatial components can be handled. The figure shows the longitudinal spatial correlation in the axial direction from axial velocity correlation in time. The matching is fairly good. Figure 3 gives the temporal correlation of the axial velocity evaluated from the longitudinal spatial correlation in the axial direction evaluated as described in equations (7)-(8). As described in 2.2, equation (9) we can also evaluate the temporal correlation from transverse spatial correlation. The temporal correlation of lateral velocity as obtained from the transverse spatial correlation in the axial direction is given in figure 4. The transverse direction is inhomogeneous, and it would be incorrect to apply the model in this direction. In all the cases the matching is fairly good, and are typical of the results.

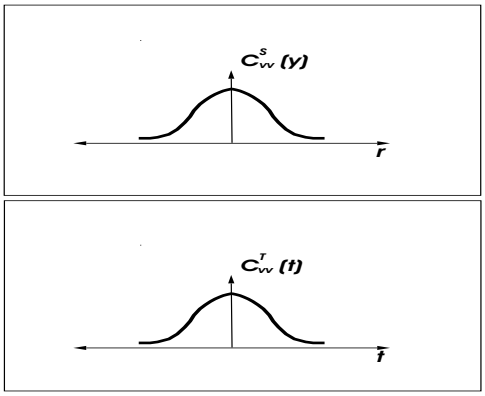

Figure 1: Schematic of the correlations

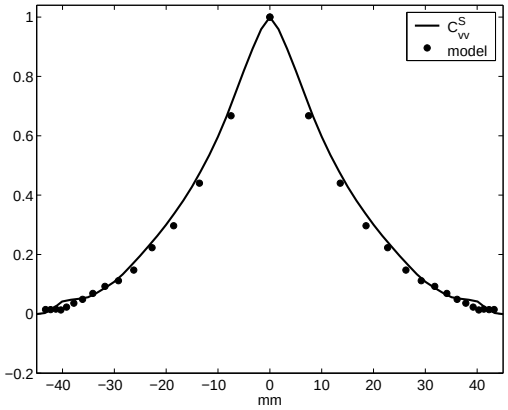

Figure 2: Longitudinal spatial correlation from temporal correlation of the axial velocity

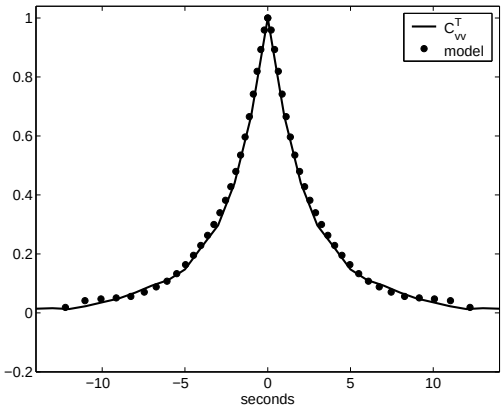

Figure 3: Temporal correlation from longitudinal spatial correlation of the axial velocity

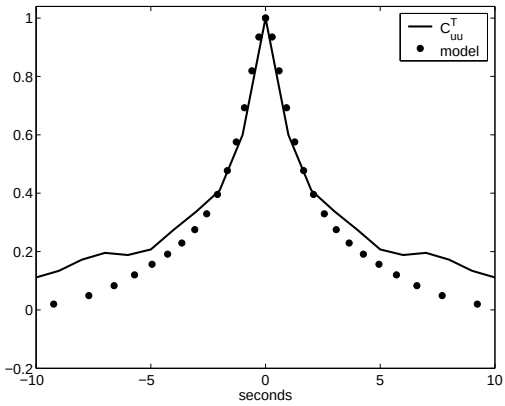

Figure 4: Temporal correlation from transverse spatial correlation of the lateral velocity

5. APPLICATIONS AND CONCLUSION

The model would be quite useful in case of evaluation of turbulent statistics, especially in the cases where one or the other of the correlations cannot be measured. While relating to the inference of the spatial statistics from the temporal measurements of the advected field, using Taylor's frozen turbulence hypothesis, we can see that the dispersion velocity is augmented by the advection velocity, and the error is proportional to the ratio of the relevent rms velocity and the mean velocity of advection.

To conclude the model appears to be useful for getting additional information from turbulent statistics.

REFERENCES

[1] Arakeri, J.H. and Cholemari, M.R.: Fully developed buoyancy driven turbulence in a tube *Proceedings of the 9th ACFM* 2002

[2] Baldwin, L.V. and Mickelsen, W.R.: Turbulent diffusion and anemometer measurements *Trans Am Soc Civil E Part I* 1963 **128**, 1595–1627

[3] Favre, A.J.: Review on space-time correlations in turbulent fluids *Trans ASME J App Mech* 1965 **32E**, 241–257

[4] Favre, A.J., Gaviglio, J.J. and Dumas, R.: Space-time correlations and turbulent spectra in a turbulent boundary layer *J Fluid Mech* 1957 **2**, 313–342

[5] Favre, A.J., Gaviglio, J.J. and Dumas, R.: Further on space-time correlations and turbulent spectra in a turbulent boundary layer *J Fluid Mech* 1958 **3**, 344–356

[6] Fisher, M.J. and Davies, P.O.A.L.: Correlation measurements in a non-frozen pattern of turbulence *J Fluid Mech* 1964 **18**, 97–116

[7] Lumley, J.L.: Interpretation of time spectra measured in high intensity shear flows *Phys Fluids* 1965 **8**(6), 1056–1062

[8] Saffman, P.G.: An approximate calculation of the lagrangian autocorrelation coefficient for stationary homogeneous turbulence *App Sc Res A* 1963 **11**, 245–255

[9] Taylor, G.I.: The spectrum of turbulence *Proc Roy Soc London* 1938 **A132**, 476–490

[10] Wyngaard, J.C. and Clifford, S.F.: Taylor's hypothesis and high frequency turbulence spectra *Jour Atmos Sc* 1977 **34**, 922–929

The 10th Asian Congress of Fluid Mechanics
17-21 May, 2004
The University of Peradenia, Sri Lanka

Drag Reduction in Swirling Turbulent Flows through a Curved Pipe

Toshihiro Takami *

* Department of Mechanical Engineering, Okayama University of Science,
1-1 Ridaicho, Okayama-city 700-0005, JAPAN
E-mail: takami@mech.ous.ac.jp

Key Word: Three Dimensional Flow, Turbulent Flow, Swirling Flow, Curved Pipe, Drag Reduction

ABSTRACT

The effect of the injection of swirling motion into turbulent flows in a curved pipe is studied experimentally. Friction of the swirling flow in a straight pipe is known to increase as the introduced swirl intensifies. That in a curved pipe, on the other hand, is found to reduce compared with that of the non-swirling case as long as the intensity of the injected swirl is relatively small. In order to investigate this novel drag reduction, velocity distributions of the flows are also measured at some cross sections in the curved pipe by using a rotating probe technique with an inclined hot-wire. Detailed measurements of the velocity distribution reveal that, in case of weaker swirls, an interesting swingback effect appears in the vortical flow structure as it develops, and that the velocity of the primary flow in the fastest region is slightly slower than that of the non-swirling case.

1. INTRODUCTION

Turbulent flows in curved pipes are significant for many engineering applications such as piping systems in the industrial plant of heat exchangers, turbo-machinery and etc. Many researches have made it clear that the secondary flow, which consists of a pair of symmetric vortices, is induced in the pipe cross-section by the centrifugal effect due to the curvature of the pipe. It causes not only an promotion of the heat transfer and fluids mixing but an increase of the flow friction. In the present study, the effects of the introduction of swirling flow into the turbulent flow in the curved pipe are investigated experimentally as an attempt of the drag reduction of the curved pipe flow.

Nomenclature (see Fig.1)

C_P : Pressure Coefficient
d : Pipe Diameter (=104mm)
k : Turbulence Energy $[=(\overline{u'^2}+\overline{v'^2}+\overline{w'^2})/2]$
P : Static Pressure at Pipe Wall
Rc : Curvature Radius (=780mm)
Re : Reynolds Number ($=Wad/\nu$)
Wa : Cross-Sectional Average Velocity
r, θ, φ (z): Coordinate System
U,V,W : Velocity in r, θ, φ (z) Direction
α : Guide Vane Angle of Swirl Generator
λ : Pipe Friction Coefficient

Suffix
', o : Mean, Fluctuation, and Non-Swirl

2. EXPERIMENTAL APPARATUS

Schematic views of a tested piping system and a swirl generator are shown in Fig.1. The piping system is composed from the swirl generator, the 180° curved pipe of d=104mm and Rc=780mm (a radius ratio Rc/d

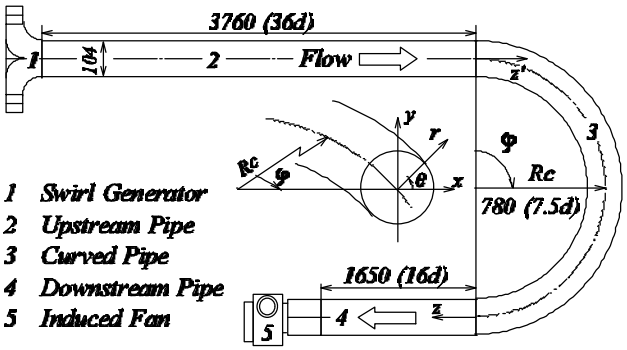

(a) Tested Piping System

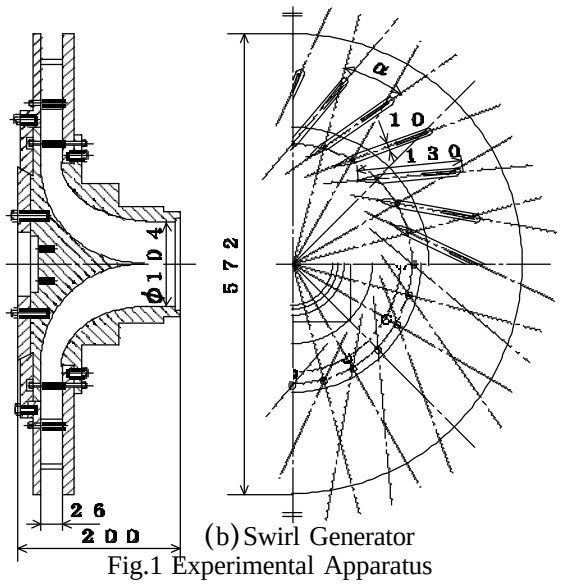

(b) Swirl Generator

Fig.1 Experimental Apparatus

=7.5), an upstream tangent of 3.76m (36d) long, a downstream one of 1.65m (16d) long and an induced fan. Axissymmetric swirling flows are produced by the swirl generator with 24 guide vanes installed circularly between two parallel circular plates. An intensity of the swirling motion can be regulated by a variable angle α of the guide vanes.

In order to investigate the drag reduction in the curved pipe due to an instability of injected swirling flows, distributions of wall static pressure in the curved section are measured from φ=0° (the entry) to φ = 180° (the exit) with an increment of 30° along the pipe axis. As the reference value of the wall static pressure, the pressure at z'=-20d, which lies in the upstream tangent, is selected. Velocity distributions are also measured at some cross-sections by using a rotating probe technique with an inclined hot-wire, to study vortical flow structures in case of a weakly swirling flow when the drag reduction has been excited.

The Reynolds numbers examined are varied from Re 2×10^4 to 6×10^4.

3. EXPERIMENTAL RESULTS

3.1 Wall Static Pressure

Distributions of the wall pressure for Re=4×10^4 are shown in Fig.2. In the figure, the pressure coefficients

$$C_P=\frac{2(P-Pref)}{\rho Wa^2} \quad \cdots(1)$$

are plotted where Pref is the reference pressure measured at z'=-10d. Also, the dash-dotted line and the hypotenuse of the right-angled triangle depicts the pressure gradient in the straight pipe from z'=-20d to -10d and that in the curved pipe from φ=90° to 150°, respectively. Those friction coefficients λ are shown in Fig.3 with solid and dash-dotted lines which respectively indicate the Reynolds number dependence of the non-swirling turbulent flow in the curved pipe (by Ito) and in the straight pipe (by Blasius);

$$\lambda_o=0.3164(2Rc/d)^{-0.1}\,Re^{-0.2} \quad \text{(Ito)}$$
$$\lambda_o=0.3164Re^{-0.25} \quad \text{(Blasius)} \quad \cdots(2)$$

The friction coefficient of the swirling flow in the curved pipe is found to reduce compared with that of the non-swirling flow as long as the injected swirl is relatively weak.

Figure 4 indicates the rate of the drag reduction, which is defined by

$$DR=\frac{\lambda-\lambda_o}{\lambda_o} \quad \cdots(3)$$

where λ_o is given by Eqs(2). The flow friction of the swirling flow in the straight pipe is known to increase as the introduced swirl intensifies. On the other hand, it decreases in the curved pipe if the injected swirl is generated by the guide vane with angles α 0° to 20°, in which cases the injected swirl is relatively weak. Thus, the drag reduction occurs by the weak swirl injection.

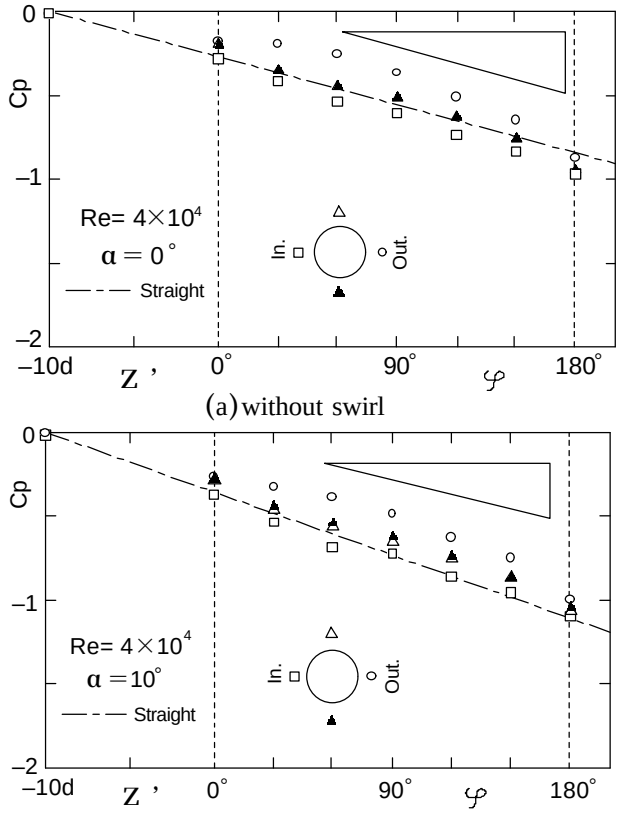

Fig.2 Axial Distribution of Wall Pressure

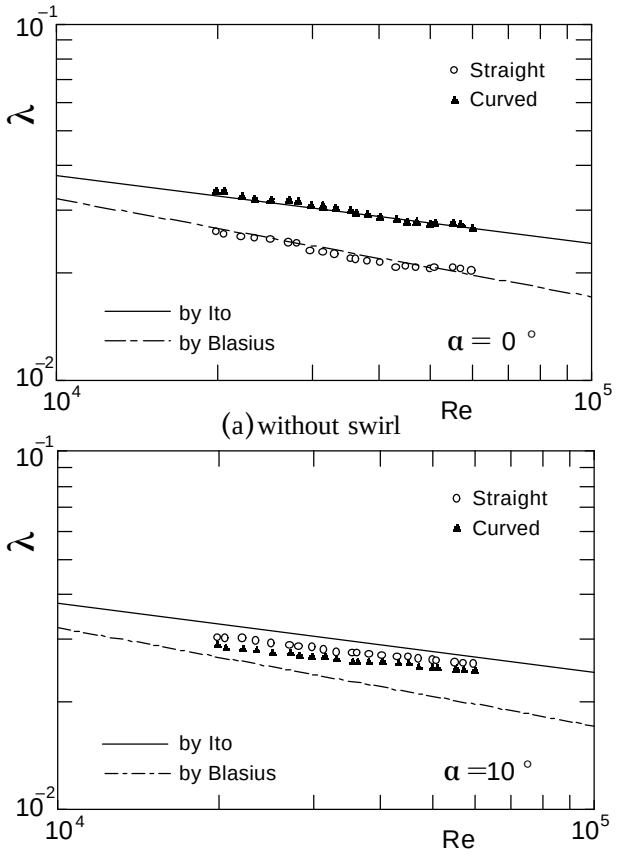

Fig.3 Friction Coefficient

3.2 Vortical Flow Structure

In Fig.5, three-components of the mean velocities and the turbulence energy at the sections φ =0°, 30°, 90° and 150° are depicted for Re=4×10⁴ (Wa 5.6m/s) and the weak swirl case of α =10°, where the drag reduction rate takes its minimum (see Fig.4).

The weakly swirling turbulent flow is injected into the curved section of the pipe. At the entry φ =0° of the curved section, the secondary flow $(\overline{U},\overline{V})$ created by the injection of clockwise swirl and the turbulence energy *k* are almost axisymmetric. The axial velocity $\overline{W}$, on the other hand, takes its maximum at slightly inner side of the cross-section. This position shift of the fast velocity region is also seen in the curved pipe without the swirl injection.

At φ =30°, a small secondary vortex which rotates in the counter direction to the injected swirl is onset near the upper wall of the pipe by the centrifugal effect. The core of injected swirl shifts to the lower side from the pipe center and starts to whirl around the pipe axis in the clockwise direction as that of injected swirl. The slow region of the axial flow and the slight high region of the turbulence energy are observed at the upper-left side of the cross-section, where the principal swirl and the counter rotating vortex collide each other. The flow pattern is asymmetric about the central horizontal plane of the cross-section.

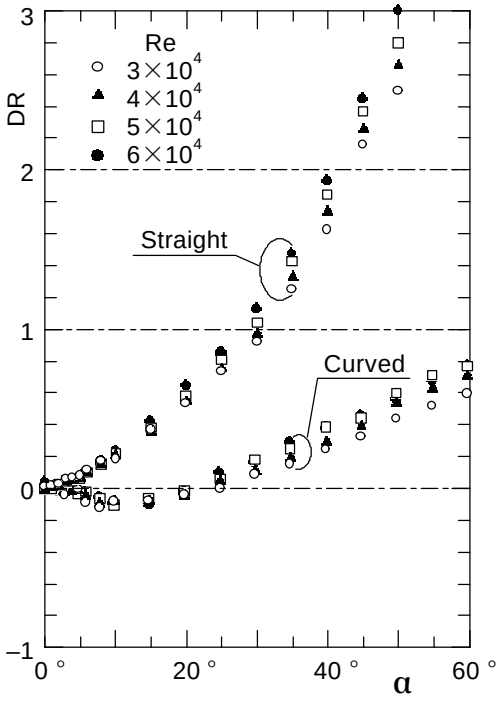

Fig.4 Rate of Drag Reduction

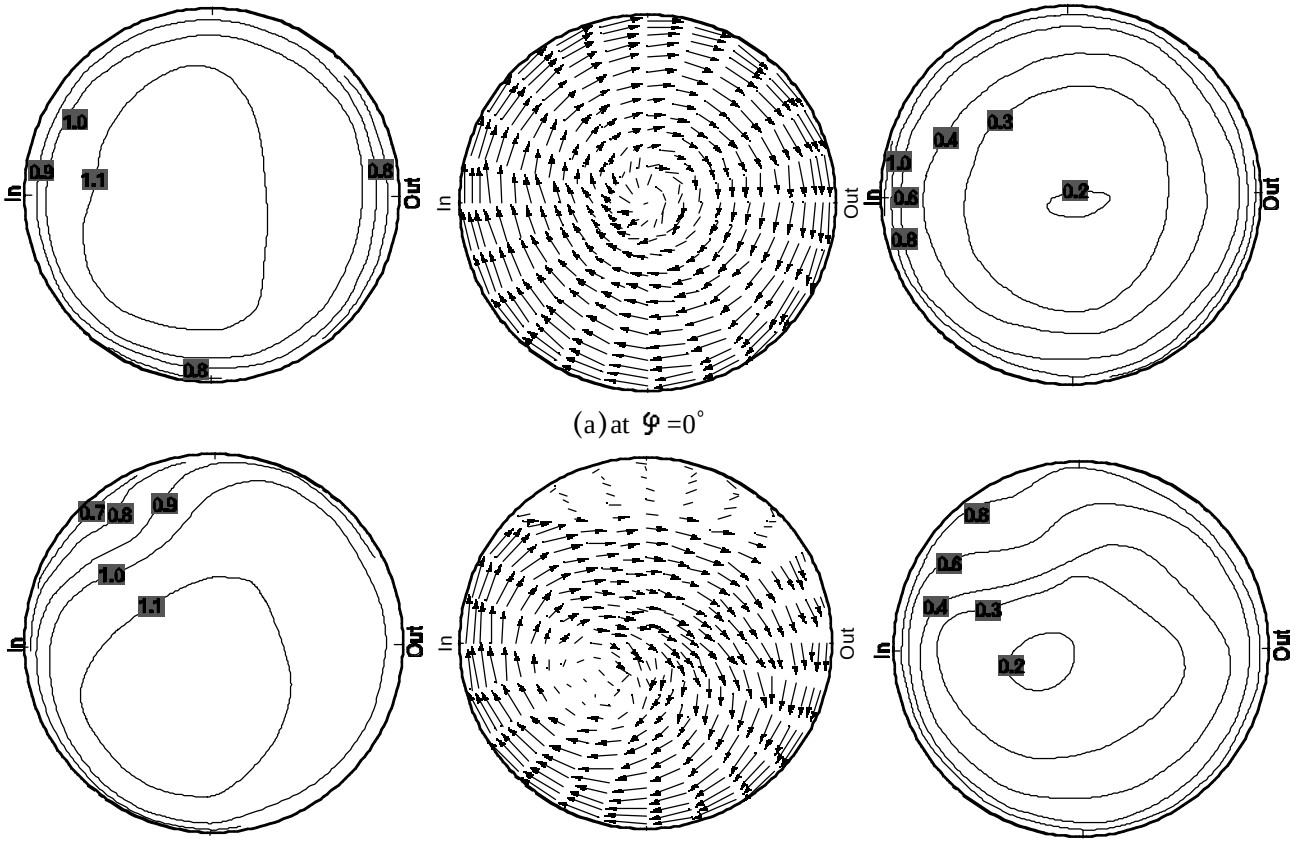

(a) at φ =0°

(b) at φ =30°

Fig.5 Graphic Illustration of Flow Pattern [The left figures show the contours of the normalized axial flow $\overline{W}$/Wa, the middle ones the velocity vectors of the secondary flow $(\overline{U},\overline{V})$, the right ones the contours of the normalized turbulence energy $k/Wa^2\times10^2$. The length of velocity vectors is also normalized by the cross-sectional average velocity Wa which corresponds to one-third of the pipe diameter.]

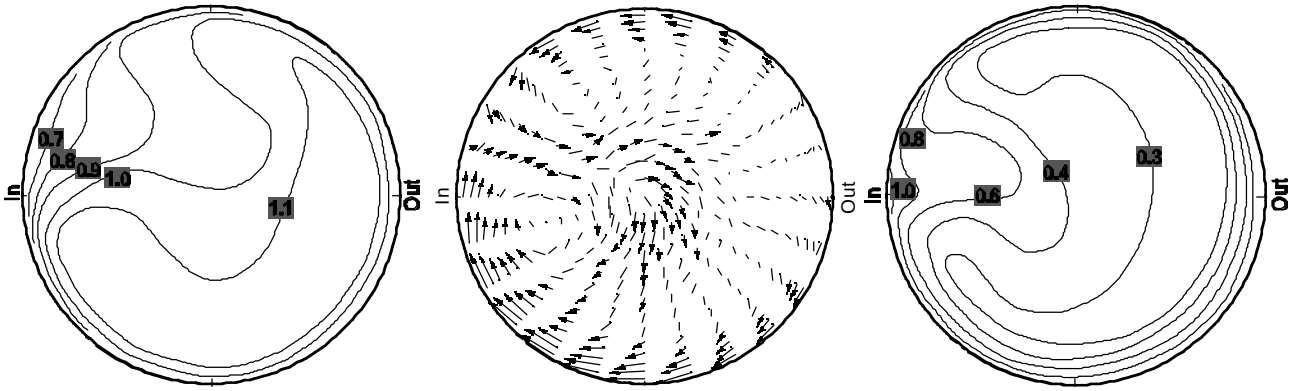

(c) at φ=90°

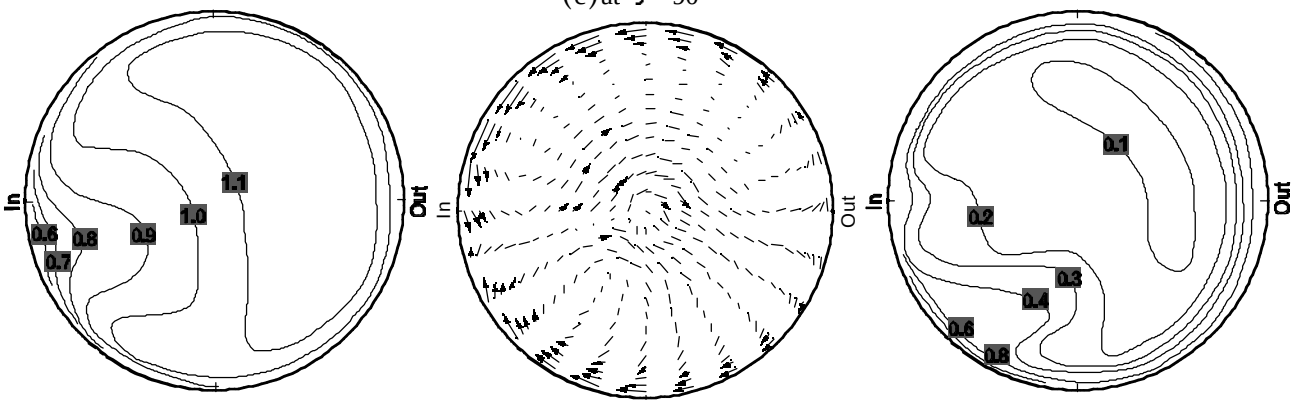

(d) at φ=150°

Fig.5 [continued] Graphic Illustration of Flow Pattern

At φ=60°, not shown here, the new counter-rotating vortex grows in the upper side of the cross-section and the eccentric core of the principal vortex is located near the inside wall. The axial flow is distorted because the slow fluid near the pipe wall is convected to the pipe center from the upper-left by the strong secondary flow.

At φ=90°, the counter-rotating vortex grows up to occupy the almost upper half of the cross-section and the injected swirl declines in the lower half. The overall structure of flow rotates counter-clockwisely.

Consequently, at φ=150°, the counter rotating vortex expands over the upper half of the cross-section. The slow region of the axial flow and the strong region of the turbulence energy move down to the lower part of the cross-section along the inside wall. In this way, those regions rotate counter-clockwisely as the curved angle φ increases and do not approach symmetric states but over-rotate. Such a state of over-rotation make a trigger to induce the reversely vortical motion of flow structure in the curved pipe, which may be called as the swingback phenomenon.

At the exit φ=180°, not shown here, the flow structure recovers the symmetry with respect to the central horizontal plane. It looks quite similar to that of the non-swirling flow in the ordinary curved pipe.

4. CONCLUSION

The effect of the injection of swirling motion into turbulent flows in a curved pipe is studied experimentally. Main results obtained are as follows;

(1) The friction factor of the swirling flow in the curved pipe is found to reduce compared with that of the non-swirling case as long as the intensity of the injected swirl is relatively weak.

(2) Detailed measurements of the velocity distribution reveal that the interesting swingback phenomenon appears in the vortical structure of the developing flow when the drag reduction occurs in case of the weakly swirling motion injected into the curved pipe. However, the elucidation of these phenomena needs further study.

REFERENCES

Ito,H. (1959) Friction Factors for Turbulent Flow in Curved Pipes. Trans. ASME (ser.D) 81, 123-134.

Sudou,K., Takami,T., & Hibara,H. (1995) Turbulent Flows in Rough Curved Pipes. J. Turbomachinery 23-8, 455-460 (in Japanese).

Sudou,K., & Takami,T. (1994) Swirling Flows in a Circular-Sectioned 90° Bend. Trans. JSME (ser.B) 60-570, 464-472 (in Japanese).

Sudou,K., Takami,T., & Hibara,H. (1997) Weakly Swirling Flows through a 90° Bend. Trans. JSME (ser.B) 63-606, 505-512 (in Japanese).

Takami,T. (1998) Three-Component Velocity Measurements in Turbulent Flows using a Technique of Rotating Probe with an Inclined Hot-Wire. JSME Int. J. (ser.B) 41-1, 145-150.

Proceedings of the Tenth Asian Congress of Fluid Mechanics
17-21 May 2004, Peradeniya, Sri Lanka

THE NONEQUILIBRIUM CASCADE BEHAVIORS OF FORCED ISOTROPIC TURBULENCE

A.-K. Xiong, S. Izawa, and Y. Fukunishi
Department of Mechanical Engineering, Tohoku University, Sendai 980-8579, Japan

ABSTRACT: The dynamic behaviors of a forced isotropic turbulence are analyzed from several new viewpoints. The correlation function between the rotation and the deformation of a fluid particle, the amount of the averaged nonlinear interaction between the rotation and the deformation in the physical space, and the Kolmogorov entropy in the rotation-deformation space are used to examine the behaviors of complex flows. The results show that the first two undergo nearly the opposite paths in the nonequilibrium cascade process and have steady asymptotic states. The entropy is found to increase within the nonequilibrium cascade process, which is consistent with the disordered nature of turbulence. To reveal the characteristics of the vector $W_i = \omega_j S_{ji}$, which appears in the vorticity transport equation and whose role is to stretch and distort the vorticity, a two-dimensional phase space showing the relative orientation of the vector **W** against the vorticity vector is examined. It is shown that in the nonequilibrium developing stage, the vorticity stretching exceeds the compression. There also exist a strong tendency for the vector **W** and the vorticity vector to become aligned with each other. It is also shown that the alignment and the deformation in the cross-sectional plane tend to be stronger when the vorticity is high.

1. INTRODUCTION

Due to its complexity, it is still a challenge to reveal the fundamental characteristics of turbulence. However, thanks to the advancement of the computer power, it is now feasible to obtain a database of three-dimensional complex flows in detail by direct numerical simulations. The field of velocity gradients, consisting of deformation tensors and rotation tensors may disclose more mechanisms and features of the fluid flows, compared to the velocity field. Mathematically, frame-independent scalars of a tensor are preferred to depict the properties of the tensor. The two well-known and physically meaningful invariants are the enstrophy $\omega^2 = \omega_i\omega_i$ and the deformation modulus or strain strength $S^2 = S_{ij}S_{ij}$. Here, ω_i is the vorticity vector and S_{ij} is the deformation tensor. The spatial characteristics of these two invariants have been extensively documented in the past. In the last decade, the investigations of other invariants besides the two were increasingly carried out. Especially, the statistical behavior of orientations of the vorticity vectors in the frame of the principal axes of the deformation tensors has attracted more attentions (e.g. Andreotti, 1997 and references therein). Studies for the cases of homogeneous isotropic turbulence (Nomura and Post, 1998, Tsinober, 1998), homogeneous sheared turbulence (Nomura and Diamessis, 2000), and atmospheric surface layer (Kholmyansky et al., 2001) have been carried out. It was shown that there exists a tendency between the vorticity vector and the intermediate eigenvector of the deformation tensor to become aligned with each other. The similar tendency between the vorticity and the vector $W_i = \omega_j S_{ji}$, which appears in the transport equation of vorticity and whose role is to stretch and distort vorticity tubes, was also shown by Tsinober et al. (1992). It should be pointed out here that there is a strong relation between the two alignments, because the alignment of vorticity vector with **W** means that the vorticity vector is one of the eigenvectors of the deformation tensor. Tsinober et al. (1999) also discussed the behaviors of the key nonlinearities related to the velocity gradients in the regions of flow dominated by enstrophy and strain. Chong et al. (2002) overviewed a method of using the invariants of the velocity gradient tensors to study eddy motions and turbulences. Very recently, Xiong et al. (2003) introduced a correlation function between the rotation and the deformation of a fluid particle, which represents the strength of the

nonlinear interaction between the rotation and the deformation, and the Kolmogorov entropy of the rotation-deformation space, in order to investigate the complicated behaviors of four vortex ring interaction, and proposed using a two-dimensional normalized phase space to depict the relative orientation of the vector $W_i = \omega_j S_{ji}$ with respect to the vorticity. In this phase space the vector is limited in the upper half of an area bounded by a ellipse with the half of the long and the short axes being $\sqrt{2/3}$ and $\sqrt{1/2}$, respectively.

In this paper, DNS of a forced three-dimensional isotropic turbulence is performed using Lattice Boltzmann Method with the resolution of 128^3. The turbulence is forced by continually injecting random velocity fields which are consist of the modes with the wavenumber of one to four. By looking into the behaviors of the variables with these new viewpoints, some new fundamental features of the nonequilibrium cascade behaviors of forced isotropic turbulence are revealed.

2. DYNAMICS OF THE INVARIANTS OF VELOCITY GRADIENT TENSOR

It has been known that the number of the *independent* invariants of *any* asymmetrical tensor is not more than six, in the sense that each extra-invariant has an algebraic constraint (linear or nonlinear) equation relating it to the six independent invariants. By decomposing the asymmetrical velocity gradient tensor $u_{i,j}$ into the symmetric part $S_{ij} = (u_{i,j} + u_{i,j})/2$ and the antisymmetric part $R_{ij} = (u_{i,j} - u_{i,j})/2 = -\epsilon_{ijk}\omega_k/2$, besides the trivial invariant $S_{ii} \equiv 0$ for incompressible flows, the other five concise independent invariants may be chosen as:

$$J_1 = S_{ij}S_{ij} \tag{1}$$

$$J_2 = S_{ij}S_{jk}S_{ki} \tag{2}$$

$$I_1 = \omega_i\omega_i \tag{3}$$

$$I_2 = \omega_i S_{ij}\omega_j \tag{4}$$

$$I_3 = \omega_i S_{ij}S_{jk}\omega_k \tag{5}$$

Therefore, all that are need to know in this context are the properties of the three physically meaningful variables themselves, i.e. strain, vorticity, and **W** vector, and the relative orientation of the **W** vector with vorticity vector. Although these five quantities are free from each other in the tensor theory viewpoint, they are closely coupled by a dynamic system which can be derived from the incompressible Navier-Stokes equations:

$$\begin{aligned}\frac{DJ_1}{Dt} = &-2J_2 - \frac{1}{2}I_2 - 2S_{ij}\frac{\partial^2 p}{\partial x_j \partial x_i} \\ &-2\nu\frac{\partial S_{ij}}{\partial x_l}\frac{\partial S_{ji}}{\partial x_l} + \nu\frac{\partial^2 J_1}{\partial x_l \partial x_l}\end{aligned} \tag{6}$$

$$\begin{aligned}\frac{DJ_2}{Dt} = &-\frac{3}{2}J_1 J_1 + \frac{3}{4}J_1 I_1 - 3S_{ij}S_{jk}\frac{\partial^2 p}{\partial x_k \partial x_i} \\ &-6\nu S_{ij}\frac{\partial S_{jk}}{\partial x_l}\frac{\partial S_{ki}}{\partial x_l} + \nu\frac{\partial^2 J_2}{\partial x_l \partial x_l}\end{aligned} \tag{7}$$

$$\frac{DI_1}{Dt} = I_2 - 2\nu\frac{\partial \omega_i}{\partial x_j}\frac{\partial \omega_i}{\partial x_j} + \nu\frac{\partial^2 I_1}{\partial x_l \partial x_l} \tag{8}$$

$$\begin{aligned}\frac{DI_2}{Dt} = &I_3 - \omega_i\frac{\partial^2 p}{\partial x_i \partial x_j}\omega_j + \nu\frac{\partial^2 I_2}{\partial x_l \partial x_l} \\ &-2\nu\left(\frac{\partial \omega_i}{\partial x_l}\frac{\partial S_{ij}}{\partial x_l}\omega_j + \frac{\partial \omega_i S_{ij}}{\partial x_l}\frac{\partial \omega_i}{\partial x_l}\right)\end{aligned} \tag{9}$$

$$\frac{DI_3}{Dt} = -2\omega_i \frac{\partial^2 p}{\partial x_i \partial x_j} S_{jk}\omega_k + \nu \frac{\partial^2 I_3}{\partial x_l \partial x_l}$$
$$-2\nu(2\frac{\partial \omega_i}{\partial x_l}\frac{\partial S_{ij}}{\partial x_l}S_{jk}\omega_k + \frac{\partial \omega_i S_{ij}}{\partial x_l}\frac{\partial S_{jk}\omega_k}{\partial x_l}) \tag{10}$$

Here, $D(*)/Dt$ stands for the material derivatives. Note that for two-dimensional flows, $J_2 = I_2 = I_3 = 0$, indicating only global effects exist. It should also be noted that I_3 serves as production term of I_2 and the latter plays the same role on I_1. Because of the non-negative characteristics of I_3, the predominance of the vortex stretching over compressing can be expected.

As shown in Eqns.(6), (7), (9), and (10), the pressure Hessian plays an important role in the development of the system. While the effects of the anisotropic part of the Hessian are difficult to analyze due to its global feature, the influence of the isotropic part of the Hessian:

$$\frac{\partial^2 p}{\partial x_l \partial x_l} = Q = \frac{1}{2}I_1 - J_1 \tag{11}$$

is local and is explicit in the governing equations of the system. Eqn.(11) is a Poisson equation from which the pressure can be educed and then the pressure Hessian can be derived. Here, the invariant Q serves as the 'source of pressure'.

Another meaningful and dimensionless invariant is

$$S_d = \frac{(\frac{I_2}{I_1\sqrt{J_1}})^2}{\sqrt{\frac{2}{3}}} + \frac{(\sqrt{\frac{I_3}{I_1 J_1} - \frac{I_2^2}{I_1^2 J_1}})^2}{\sqrt{\frac{1}{2}}} \tag{12}$$

For incompressible flows the range of value of the invariant is [0,1] and physically it represents the proportion of the deformation taking place in the meridian planes of vorticities in the total deformation. For example, S_d becomes zero in two-dimensional flows, which means that there is no deformation along the vertical direction of the flow plane. If S_d is equal to unity, it means there is not deformation in the cross-sectional plane of the vorticity.

3. RESULT AND DISCUSSION

Fig.1 shows the time development of the energy spectrum. It can be found that the smaller scales are continuously excited from timestep 1 through timestep 9. After that the smaller scales' motions reach an equilibrium state. The evolutions of the total energy and enstrophy are compared in Fig.2. Both of them share the same tendency. Small fluctuations in the curves are caused by the unsteady energy-injecting. It should be pointed out here that in our case, the slope of equilibrium spectra does not reach -5/3, which suggests the resolution of simulation is not sufficient with respect to the rate of energy-injecting. However, the focus of this paper is on the behaviors of the nonequilibrium dynamics.

From the kinematical viewpoint, the deformation and the rotation of fluid particles are two independent characteristics of fluid media. A potential flow and a flow in solid-body rotation are the two extreme cases. But in the most cases they are dynamically coupled. In Fig.3 it can be observed that the correlation between enstrophy and deformation is enhanced in the nonequilibrium development and then, after a period of decreasing, reaches a steady asymptotic state. These behaviors are in a good agreement with the features of four vortex rings' interaction (Xiong et al., 2003), and therefore seem to be independent of the details of flows, such as whether the flows are forced or decaying. The Kolmogorov entropy of rotation-deformation space also rapidly increases during the nonequilibrium cascade process, as the result of increasing of the degree of freedom for disorder, but unlike the vortex rings' case without following decay. The time-development of the

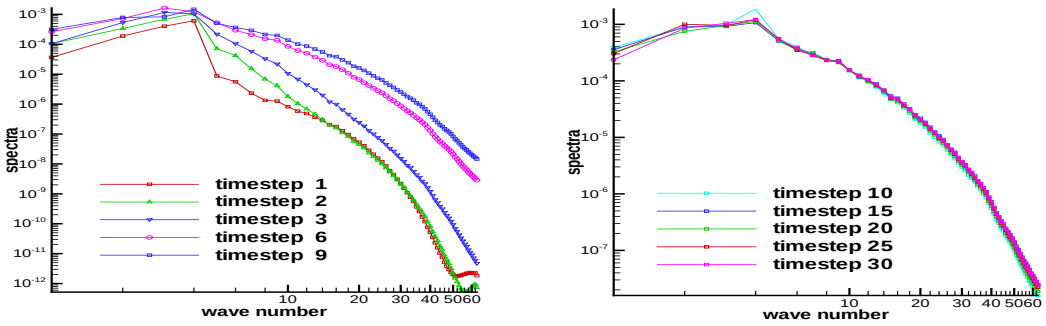

Fig. 1: Development of energy spectrum

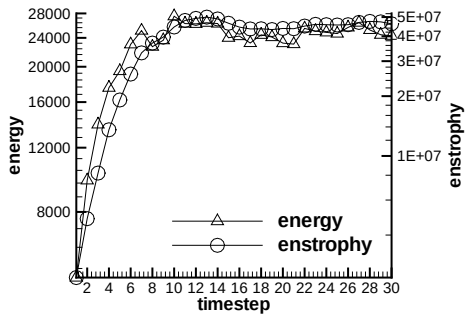

Fig. 2: Development of energy and enstrophy

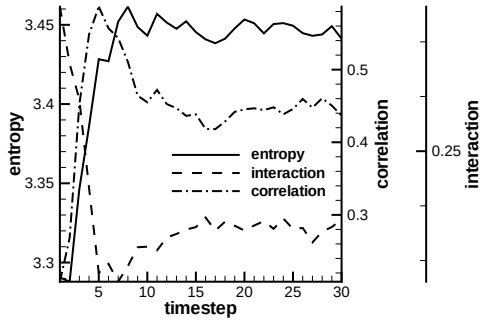

Fig. 3: Development of the variables

normalized production term $< I_3/I_1J_1 >$ is also plotted in the same figure (i.e. the interaction in the figure). Here $< * >$ denotes the spatial average. It is worthy to point out that $< I_3/I_1J_1 >$ may also be regarded as the non-linear interaction between the rotation and the deformation. The behaviors of this variable in the figure are also in good agreement with the four vortex rings' case and suggest that the cascade in nonequilibrium state can be regarded as a relaxation process of non-linear interaction between deformation and rotation, even though their correlation increases.

All the agreement with the results of the four vortex rings' interaction substantiate the importance of vortex-vortex interaction in turbulence. The results of this paper also support the discussion in Xiong et al. (2003) that the entropy exciting is a basical property of the cascade process and then can serve as an indicator of cascade for the flows without periodic boundary condition.

From the vorticity transport equation, it can be assumed that development of the vorticity is affected by the **W** vector. This vector represents one of two non-linear terms in the vorticity transport equation, and plays a vital role in energy cascade of the three-dimensional turbulences. To reveal its characteristics and to understand its dynamic behaviors, a two-dimensional phase space, proposed in Xiong et al. (2003), is shown in Fig.4. The abscissa in Fig.4 is $I_2/(I_1\sqrt{J_1})$ and its direction is parallel to the direction of the local vorticity in the flow field. The ordinate is $\sqrt{I_3/(I_1J_1) - I_2^2/(I_1^2J_1)}$. Therefore, from Eqn.(12) we can know $S_d = constant$ is a cluster of ellipses and the largest ellipse is $S_d = 1$. Any point in this space, which is determined by a set of

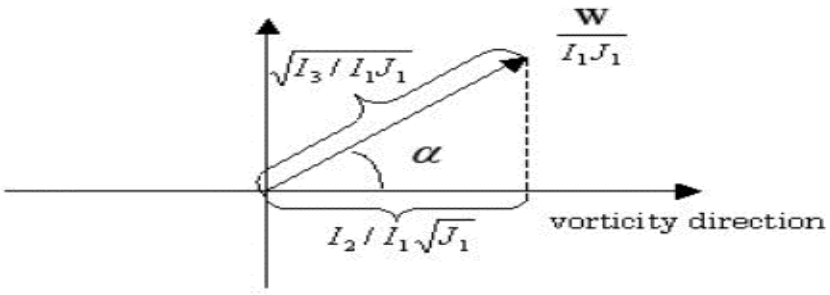

Fig. 4: Diagram of the relative orientation of $\mathbf{W}$ vector with respect to vorticity vector

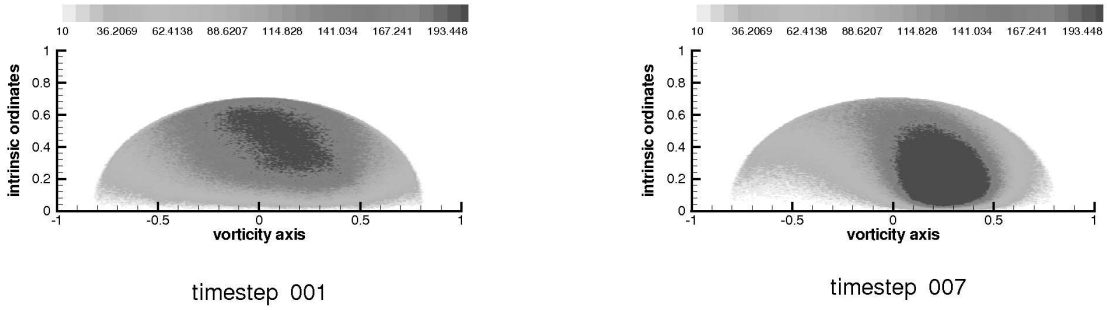

Fig. 5: PDFs of the normalized vorticity stretching and distorting vector $\mathbf{W}/I_1 J_1$

invariants, represents the normalized $\mathbf{W}$ vector in the direction relative to the local vorticity: the distance from the origin of the coordinates system represents the magnitude of the vector and the angle α indicates the angle between the vector and the local vorticity.

The two figures in Fig.5 show the PDFs of the same $\mathbf{W}$ vector end distributions in the earlier state and in the later state of cascade. It can be observed in the figures that not all of events but the most are undergoing elongation and the majority of events move to locations with smaller α and smaller S_d. Therefore strong tendency of alignment between the $\mathbf{W}$ vector and the vorticity vector can be found. The decrease of S_d suggests that the major deformation shifts to the cross-sectional planes of vorticities from their meridian planes. At the same time, the cases where the angle α are close to zero are rare.

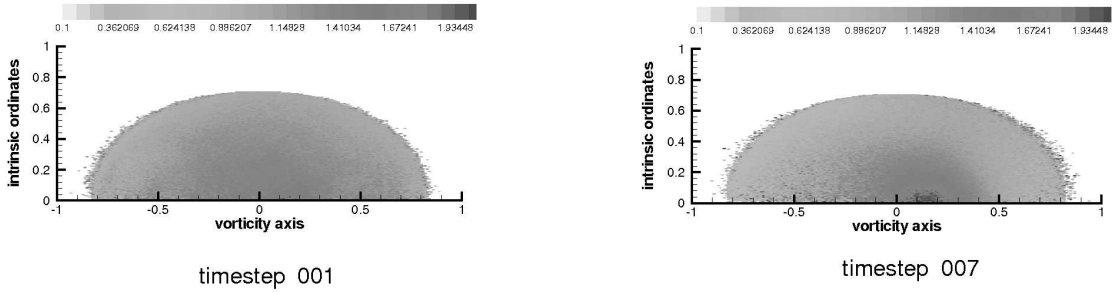

Fig. 6: Flood contours of the averaged enstrophy

In Fig.6, the distribution of the averaged values of enstrophies of the events that share same point in the two-dimensional phase space is shown. The enstrophy has its peak near the abscissa, and this peak is located in the quite smaller elliptical area (i.e. quite smaller values of S_d) with lower PDF in Fig.5. These results indicate that the high vorticity events are rarer but pose higher aligning tendency and have stronger deformation in cross-sectional planes than that in the meridian planes. It is also clear that intensive vorticities are undergoing elongation process because they are located on the positive side.

4. CONCLUSIONS

The analyses of DNS data of forced isotropic turbulence revealed that the characteristics of the flow is quite similar to that of four vortex rings' interaction. The result indicates the importance of interaction between vortices in turbulence.

It is clearly shown in the phase space analysis that the stretching is more dominant than the compressing in a turbulent flow, especially for the region of concentrated vorticity. The reason is due to the non-negative source term in its governing equation. The tendency of the alignment between the **W** vector and the vorticity vector becomes stronger during the non-equilibrium cascade process when the turbulence is developing. The concentrated vorticities have higher alignment tendency and are with stronger deformation in cross-sectional planes in comparison with the deformation in meridian planes.

REFERENCES

[1] Andreotti, B., 1997, Phys. Fluids, Vol. 9(3), pp. 735-742.

[2] Chong, M. S., Higgins, K., and Ooi, A., 2002, Proc. of the 9th Asian Congress of Fluid Mech., Ed. E. Shirani and A. Pishevar. (CD-ROM).

[3] Galanti, B. and Tsinober, A., 2000, Phys. Fluids, Vol. 12(12), pp. 3097-3100.

[4] Kholmyansky, M., Tsinoberf, A., and Yorish, S., 2001, Phys. Fluids, Vol. 13(1), pp. 311-314.

[5] Nomura, K. K. and Diamessis, P. J., 2000, Phys. Fluids, Vol. 12(4), pp. 846-864.

[6] Nomura, K. K. and Post, G. K., 1998, J. Fluid Mech., Vol. 377, pp. 65-97.

[7] Tanaka, M. and Kida, S., 1993, Phys. Fluids A, Vol. 5(9), pp. 2079-2082.

[8] Tsinober, A., 1998, Eur. J. Mech. B/Fluids, Vol. 17(4), pp. 421-449.

[9] Tsinober, A., Kit, E., and Dracos, T., 1992, J. Fluid Mech., Vol. 242, pp. 169-192.

[10] Tsinober, A., Ortenberg, M., and Shtilman, L., 1999, Phys. Fluids, Vol. 11(8), pp. 2291-2297.

[11] Tsinober, A., Shtilman, L., and Vaisburd, H., 1997, Fluid Dynamics Research, Vol. 21, pp. 477-494.

[12] Xiong, A., Izawa, S., and Fukunishi, Y., 2003, 3rd Int. Symp. on Turb. and Shear Flow Phen., Vol. 1, pp. 27-32.

Proceedings of the Tenth Asian Congress of Fluid Mechanics
17-21 May 2004, Peradeniya, Sri Lanka

DETAILED WIND TUNNEL MEASUREMENTS OF TURBULENCE PARAMETERS WITHIN A REGULAR ARRAY OF CUBE ROUGHNESS

M. Roth
Department of Geography, National University of Singapore, Singapore

H. Ueda
DPRI, University of Kyoto, Kyoto, Japan

ABSTRACT: This study investigates the mean and turbulence characteristics of a neutral flow developed over an experimental surface with different roughness characteristics. Preliminary results from 2 staggered roughness arrays are presented. Vertical and transverse profiles show the strong modification normalized turbulence statistic experienced within and just above the canopy. The present results are compared to other laboratory and a limited number of full scale urban observations.

1. INTRODUCTION

The urban surface consists of irregular arrays of mainly bluff body roughness which strongly affect the airflow. Mean flow and turbulence properties are modified within the canopy and above to a height of about 2-3 times the height of the obstacles [1,2]. Traditional theories for the description of the flow are not valid in this region or need to be modified.

Because of the strong 3-dimensionality of the wind field within and above the roughness it is very difficult to obtain a complete representation based on field observations. Most real world studies are restricted to single-point measurements or profiles at one location within a canyon [3-7]. Fluid modelling studies are useful to overcome some of these difficulties encountered in full-scale research. The nature of the surface can be controlled and the flow can be sampled at sufficiently high spatial resolution.

Previous work on laboratory flow over rigid roughness includes studies by using plastic coffee cups [8], gravel [9,10], wood cylinders [11], scale model [12,13] and 2-D bars [14] as roughness elements. More recently the focus has shifted to investigations of flow in relation to the dispersion of pollutants in urban canyons. These studies inform of dispersion and flow patterns in urban street canyons based on wind tunnel experiments measuring vertical and lateral profiles of turbulence intensity and other dispersion parameters and confirming the existence of rooftop re-circulation zones and canyon vortices [15-19].

The objective of the present laboratory study is to investigate the detailed spatial characteristics of the mean and turbulence flow fields within and just above the canopy of a rough surface consisting of regularly arrayed, rigid roughness elements of varying density. In contrast to most studies reviewed, a laser Doppler anemometer (LDA) is used which offers some advantages over more conventional sensors within the canopy layer.

2. METHODOLOGY

The measurements used in the following analysis were performed in the open-circuit blower wind tunnel of the Research Institute for Applied Mechanics, Kyushu University, Fukuoka, Japan [20]. The working section of the wind tunnel is 13.5 m long, 1.5 m wide and 1.2 m high. Flow speed can be varied between 0.1 – 2.2 m s^{-1} (maximum speed was used for the present study) and the turbulence intensity of the longitudinal wind component u at the inlet is generally less than 1 %. Although capable of producing stable and unstable stratification the wind tunnel was only used in its neutral mode for the present research.

The mock urban surface consisted of cubes (dimension of each side = 30 mm) organized in 4 regular arrays with linearly increasing roughness concentration, λ:

$$\lambda = l^2 / D^2 \tag{1}$$

where l and D are the horizontal dimension of and distance to nearest cubes, respectively (Table 1, Figure 1).

Table 1: Physical characteristics of experimental surfaces

	B	C	D	E
Array-type	square	staggered	square	staggered
D (mm)	200	141.4	100	70.7
λ	0.0225	0.045	0.09	0.18

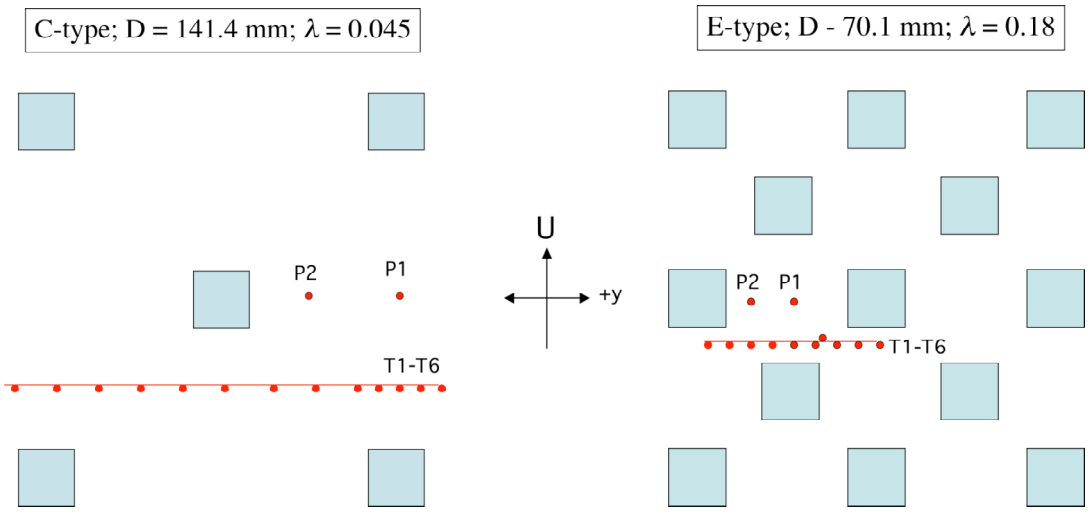

Fig. 1: Roughness layout for experimental surfaces, C-type and E-type, respectively. Dots indicate measurement locations for traverses (T1-T6) and profiles (P1 and P2). U – direction of mean flow; y – direction perpendicular (in the horizontal) to the flow.

Measurements of the alongwind (u) and vertical (w) components were done with a Dantec 2-channel Laser Doppler Anemometer (LDA) in forward scattering mode (Fig. 2). A lens with focal length of 600 mm was used to focus the beams near the centerline of the wind tunnel. The range of the frequency tracker was set to 33.3 - 333 and 100 - 1000 kHz, respectively depending on the flow speed. If used properly the LDA has many advantages compared to unmodified conventional X-wires. It is non-intrusive and capable of resolving the flow direction which is necessary in conditions of high turbulence intensity and in regions with reverse (negative) flow direction which is often the case for canopy flow.

The measurements were taken at about x = 5 m downwind from the beginning of the test section. Transverse to the flow direction traverses (y-direction) consisted of 10-13 equally spaced points and were taken at 6 heights (3 within the canopy). Vertical profiles consisted of 19 points (7 within the canopy) and were measured at 2 points behind and between canopy elements, respectively (Fig. 1). The data were sampled at 1000 Hz and averaged over 180 s. Glycol particles with mean diameter of 1.1 μm (Safex fog fluid) produced by a fog generator placed at the wind tunnel intake were used to seed the flow.

Fig. 2: LDA measuring u and w components within the canopy of type E roughness at x = 5 m.

3. PRELIMINARY RESULTS

The flow was tripped at the beginning of the test section with a 5 mm trip wire and allowed to develop over the different experimental arrangements. The resulting boundary layer was relatively shallow (0.2 – 0.3 m) compared to the height of the roughness, $h = z_H$ = 30 mm. As a consequence no substantial constant flux or inertial sublayer can develop and the range of eddy sizes is limited compared to a fully developed boundary layer. The following analysis therefore concentrates on the flow and turbulence within and just above the canopy. The preliminary results shown are for the 2 staggered roughness arrays C and E. Profiles of observations are plotted against normalized height z_s/z_H where $z_s = z$ is height of measurement.

3.1 Mean Flow

Profiles of mean velocity (U) normalized by the value at the height of the roughness ($U(z_H)$) are shown in Fig. 3. The variation of this ratio with height for the less dense array (C) measured "between" cubes (see Fig. 1) is similar to a logarithmic wind profile. The other profiles show the expected point of inflexion near the top of the canopy, which is region associated with strong shear and hence large momentum absorption. The effect is more pronounced for the high density array (E) and position directly behind a roughness element. The current observations show overall agreement with data from a variety of canopies (wind tunnel: strips, rods; field data: corn, forests [1]) and roughness densities for which high-quality turbulence data exist).

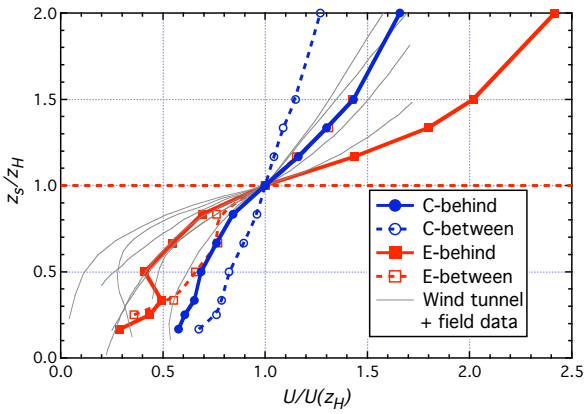

Fig. 3: Vertical profiles of normalized wind speed measured at two positions relative to the roughness elements as a function of non-dimensional height. Grey lines are results from wind tunnel and field studies [1].

U and mean vertical velocity component, *W*, are also strongly affected in the transverse (y-direction) within the canopy depending on the relative location to the roughness elements. The flow is reduced behind the obstacles but accelerates between the cubes (Fig. 4). The effect is stronger in the case of the lower density array C which probably represents an isolated roughness flow régime. In type E, on the other hand, the flow within the roughness seems to be de-coupling from the above-canopy flow which is indicative of a skimming flow régime. The spatial inhomogeneities propagate above the top of the canopy and the flow becomes uniform at about $z > 3h/2$ in both cases.

The behaviour of mean vertical velocity is more complex and in particular *W* at $z = h$ shows a large difference between the 2 surfaces (Fig. 4). The observations show that the flow is directed downward behind the cube at canopy height and above but upward within the canopy which is suggestive of a re-circulation zone behind the obstacle as found in isolated roughness flow. For type E, where the measurement point is very close to the obstacle (see Fig. 1), the upward motion is much more pronounced and probably part of a self-contained vortex developing in the cavity which is largely disconnected from the generally horizontal flow above the canopy. Unlike *U*, *W* is still affected at heights $z > 3h/2$.

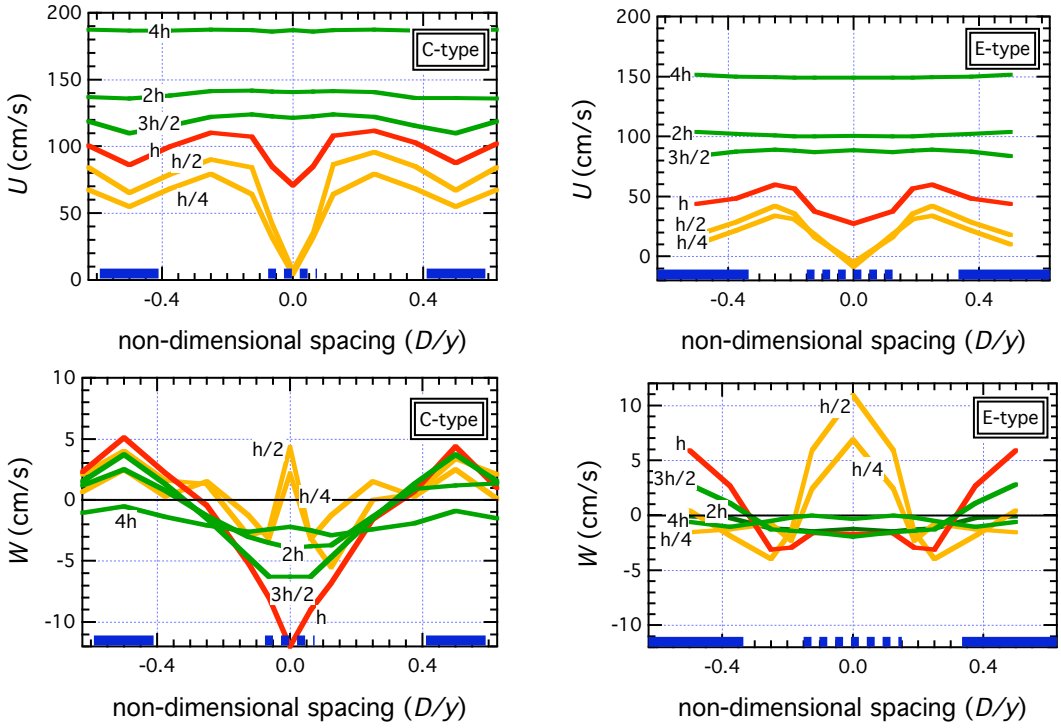

Fig. 4: Lateral *U* (top row) and *W* (bottom row) traverses at several heights (indicated as multiples of cube height *h*) plotted against non-dimensional distance between cubes for staggered arrays C and E. $D/y = 0$ and $D/y = |0.5|$ are positions directly downwind (heavy dotted line) and upwind (heavy solid line) of cubes, respectively (Fig. 1). *D* – distance between cubes; *y* – direction perpendicular (in the horizontal) to the flow.

3.2 Profiles of Turbulence

A sample of turbulence data is given in Figure 5. Profiles of normalized standard deviations of *u* (σ_u) and *w* (σ_w) measured at 2 positions are plotted as a function of non-dimensional height. Two different normalization procedures are applied. It is customary to use the constant flux layer value of the friction velocity u_* for normalizing turbulence statistics. As mentioned above only a very limited constant flux

layer was established in the present experiment and hence the largest value, usually measured just above the canopy, was used as $u_{*(c)}$. Within the canopy the values of the normalized statistics decrease with decreasing height, more so for the profiles measured behind cubes. Above z_H the values are constant but associated with some scatter (Figs. 5a, b). This is in overall agreement with other laboratory data and the few results available from urban studies. The scatter probably reflects the various geometries of the experimental surfaces. The above-canyon value of the normalized standard deviations are somewhat smaller for u and similar for w compared to urban results obtained under neutral conditions [2].

Previous research conducted in urban roughness sublayers has shown that in the absence of a well-established constant flux layer, normalization with the locally (*i.e.* measured at the same height as the variable of interest) measured $u_{*(l)}$ value leads to good results [2,4,5]. If the present observations are normalized by their local values the statistics show good agreement and little scatter between locations and roughness types above the canopy (Figs. 5c, d).

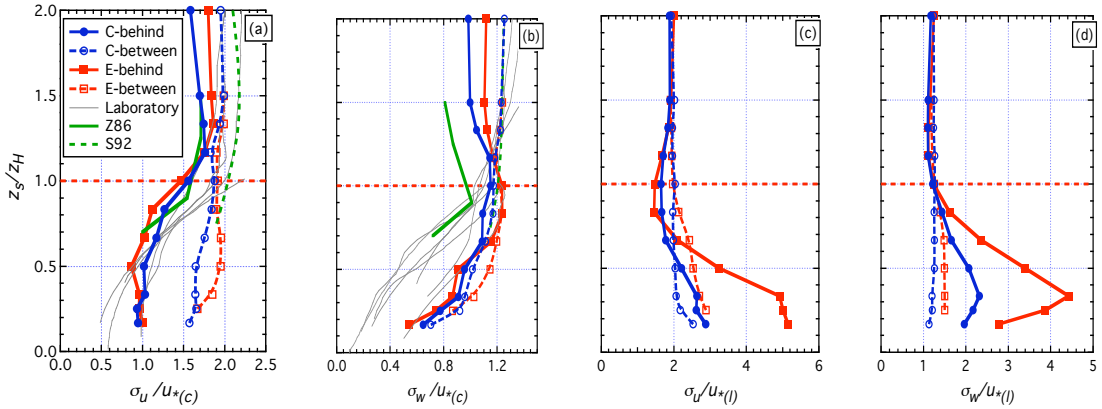

Fig. 5: Vertical profiles of σ_u (a)and σ_w (b) normalized by the constant flux layer value of $u_{*(c)}$ and normalized by the local value of $u_{*(l)}$ ((c) and (d)) measured at two positions relative to the roughness elements as a function of non-dimensional height. Thin grey lines are wind tunnel and field results (see 3.1) [1]. Green solid (Z86) and dashed (S92) lines are full-scale urban field observations [4,6].

ACKNOWLEDGMENTS

We would like to thank Dr. Karasudani as well as Mr. Ishii and Mr. Takahira (all from RIAM, Kyushu University) for help during the experiments. One of the authors (MR) would also like to acknowledge support received from the Swiss National Science Foundation (#8220-042853).

REFERENCES

[1] Raupach, M. R., Antonia, R. A. and Rajagopalan, S., 1991: Rough-wall turbulent boundary layers. *Appl. Mech. Reviews,* **44**, 1-25

[2] Roth, M. 2000: Review of atmospheric turbulence over cities. *Q. J. R. Meteorol. Soc*., **126**, 941-990.

[3] Clarke, J. F., Ching, J. K. S. and Godowitch, J. M., 1982: An experimental study of turbulence in an urban environment. *Tech. Rep. U.S. E.P.A.,* Research Triangle Park, N.C. NMS PB 226085.

[4] Rotach, M., 1995: Profiles of turbulence statistics in and above an urban street canyon. *Atmos. Env.*, **29**, 1473-1486.

[5] Roth, M. and Oke, T. R. 1993: Turbulent transfer relationships over an urban surface. I: Spectral characteristics. *Q. J. R. Meteorol. Soc*., 119, 1071-1104.

[6] Oikawa, S. and Meng, Y., 1995: Turbulence characteristics and organized motion in a suburban roughness layer. *Bound. Layer Meteorol*., **74**, 289-312.

[7] Feigenwinter, Ch., Vogt, R. and Parlow, E., 1999: Vertical structure of selected turbulence characteristics above an urban canyon. *Theoretical and Applied Climatology,* **62**, 51-63.
[8] Cook, N.J., 1973: On simulating the lower third of the urban adiabatic boundary layer in a wind tunnel. *Atmos. Env*., **7**, 691-705.
[9] Mulhearn, P. J. and Finnigan, J. J., 1978: Turbulent flow over a very rough, random surface. *Boundary-Layer Meteorol.,* **15**, 109-132.
[10] Raupach, M.R. and Legg, B.J., 1983: Turbulent dispersion from an elevated line source: measurements of wind-concentration moments and budgets. *J. Fluid Mechanics*, **136**, 111-137.
[11] Raupach, M. R., Legg, B. J. and Edwards, I., 1980: A wind tunnel study of turbulent flow close to regularly arrayed rough surfaces. *Boundary-Layer Meteorol*., **18**, 373-397
[12] Maruyama, T. and Ishizaki, H., 1988: A wind tunnel test on the boundary layer characteristics above an urban area. *J. Wind Eng. & Ind. Aerodynamics*, **28**, 139-148.
[13] Theurer, W. 1993: Diffusion of near-surface emissions in complex urban terrain. PhD Thesis, *Institute for Hydrology and Water Resources*, University of Karlsruhe, **45**,187 pp. (in German).
[14] Rafailidis, S. and Schatzmann, M, 1995: Concentration measurements with different roof patterns in street canyons with aspect ratios B/H=1/2 and B/H=1. *Institute of Meteorology*, University of Hamburg.
[15] Davidson, M, Snyder, W., Lawson, R. and Hunt, J., 1996: Wind tunnel simulations of of plume dispersion through groups of obstacles. *Atmos. Env.*, **30**, 3715-3731.
[16] Kastner-Klein, P., Plate, E. and Fedorovich, E., 1997: Gaseous pollutant dispersion around urban-canopy elements: wind tunnel case studies. *Int. J. Env. & Poll.*, **8**, 727-737.
[17] Kastner-Klein, P., Fedorovich, E. and Rotach, M. 2001: A wind tunnel study of organized and turbulent motions in urban street canyons. *J. Wind Eng. & Ind. Aerodyn*., **89**, 849-861.
[18] Brown, M., Lawson, R., DeCroix, D. and Lee, R., 2001: Measurements obtained around 2D and 3D building arrays in a wind tunnel. *Int. Soc. Environ. Hydraulics*, Tempe, AZ, 6 pp.
[19] MacDonald, R., Carter, S. and Slawson, P, 2002: Physical modelling of urban roughness using arrays of regular roughness elements. *Water, Air & Soil Poll*., **2**, 541-554.
[20] Ohya, Y., Tatuno, M., Nakamura, Y. and Ueda, H., 1996: A Thermally Stratified Wind Tunnel for Environmental Flow Studies', *Atmos. Environ*. **30**, 2881–2887.